

---

Doctoral Dissertations

Student Theses and Dissertations


---

Fall 2019

## Microstructural evolution of zirconium carbide (ZrC<sub>x</sub>) ceramics under irradiation conditions

Raul Florez

Follow this and additional works at: [https://scholarsmine.mst.edu/doctoral\\_dissertations](https://scholarsmine.mst.edu/doctoral_dissertations)

 Part of the [Materials Science and Engineering Commons](#), and the [Nuclear Engineering Commons](#)  
Department: Mining and Nuclear Engineering

---

### Recommended Citation

Florez, Raul, "Microstructural evolution of zirconium carbide (ZrC<sub>x</sub>) ceramics under irradiation conditions" (2019). *Doctoral Dissertations*. 2821.  
[https://scholarsmine.mst.edu/doctoral\\_dissertations/2821](https://scholarsmine.mst.edu/doctoral_dissertations/2821)

This thesis is brought to you by Scholars' Mine, a service of the Missouri S&T Library and Learning Resources. This work is protected by U. S. Copyright Law. Unauthorized use including reproduction for redistribution requires the permission of the copyright holder. For more information, please contact [scholarsmine@mst.edu](mailto:scholarsmine@mst.edu).

MICROSTRUCTURAL EVOLUTION OF ZIRCONIUM CARBIDE ( $\text{ZrC}_x$ )  
CERAMICS UNDER IRRADIATION CONDITIONS

by

RAUL FERNANDO FLOREZ MEZA

A DISSERTATION

Presented to the faculty of the Graduate School of the  
MISSOURI UNIVERSITY OF SCIENCE AND TECHNOLOGY

In Partial Fulfilment of the Requirements for the Degree

DOCTOR OF PHILOSOPHY

In

NUCLEAR ENGINEERING

2019

Approved by:

Joseph T. Graham, Advisor

William G. Fahrenholtz

Gregory E. Hilmas

Miguel L. Crespillo

Carlos H. Castano

## PUBLICATION DISSERTATION OPTION

This dissertation consists of four manuscripts that were prepared for publication as follows.

The paper entitled, “The irradiation response of ZrC ceramics at 800° C” (Paper I, Pages 28–59), was submitted to the *Journal of the European Ceramic Society* and is currently under revision.

The manuscript entitled “Early stage oxidation of  $\text{ZrC}_x$  under ion-irradiation at elevated temperatures” (Paper II: Pages 60–101) was submitted to the *Journal of Corrosion Science*.

The manuscript entitled “Sequential Ion-Electron Irradiation of Zirconium Carbide Ceramics: Microstructural Analysis” (Paper III: Pages 102–137) was prepared for submission to the *Journal of Nuclear Materials*.

The manuscript entitled “Fabrication and Microstructural Analysis of Hot-Pressed  $\text{ZrC}_x$  with low Hf-content” (Paper IV: Pages 144–172) is intended for submission for publication in the *Journal of Nuclear Materials* following revision based on the recommendations of the dissertation committee and review by the authors.

## ABSTRACT

A comprehensive understanding of the microstructural evolution of Zirconium Carbide ( $\text{ZrC}_x$ ) ceramics under irradiation conditions is required for their successful implementation in advanced Gen-IV gas-cooled nuclear reactors. The research presented in this dissertation focusses on elucidating the ion and electron irradiation response of  $\text{ZrC}_x$  ceramics. In the first part of the research, the microstructural evolution was characterized for  $\text{ZrC}_x$  ceramics irradiated with 10 MeV  $\text{Au}^{3+}$  ions up to doses of 30 displacement per atom (dpa) at 800 °C. Coarsening of the defective microstructure, as a function of dose, was revealed by transmission electron microscopy analysis. The lack of change in the irradiated microstructure, at doses above 5 dpa, indicated that a balance between irradiation damage accumulation and dynamic annealing of defects was reached. It was also found that concurrent oxidation occurred during the ion irradiation. The effects of irradiation on the morphology and microstructure of the initial oxide formed on the surface of  $\text{ZrC}_x$  were investigated. The concomitant reduction in size and surface coverage of the oxide nodules at high doses, indicated that oxide dissolution was the predominant mechanism under irradiation conditions.

In the second part of the research, Zirconium Carbide ( $\text{ZrC}_x$ ) was irradiated with 10 MeV  $\text{Au}^{3+}$  ions to a dose of 10 dpa and subsequently with 300 keV electrons in a transmission electron microscope (TEM). It was found that high-energy electron irradiation of pre-damaged  $\text{ZrC}_x$  foils induce atomic mixing via radiation enhanced diffusion (RED), producing surface oxidation of the TEM foil.

## ACKNOWLEDGEMENTS

I would like to start by expressing my sincere gratitude to my advisor Dr. Joseph Graham for his continuous support through my doctoral studies and related research. Certainly, this work would not been possible without his motivation, guidance, and patience. I would also like to thank Dr. William Fahrenholtz and Dr. Gregory Hilmas for providing their unending advice and expertise to my work, in addition to their modelling of several qualities I hope to emulate in all facets of my life. Thanks to Dr. Miguel Crespillo for conducting the ion irradiation experiments and for showing me that the biggest factor limiting my research was myself. I am also grateful for everything Dr. Carlos Castano did for me over the last four years.

I would be remiss if I did not thank Dr. Xiaoqing He at the Electron Microscopy Core (EMC) at the University of Missouri, Columbia. In addition to teaching me how to effectively utilize the electron microscopes, he has been a mentor and brainstorming partner for the last two years. His encouragement for my attending conferences and applying to fellowships has tremendously expanded my understanding on electron microscopy techniques. I would like to thank my friends and fellow students for all their help and support. Many people have helped me with this research, and I will not list the names for fear of omitting someone.

Finally, my deepest gratitude goes to my parents, Raul and Ingrid, my siblings, Paula and Andres, and my little niece Juliana. Without your unconditional support, I would not been able to be where I am today. I love you all very much.

## TABLE OF CONTENTS

	Page
PUBLICATION DISSERTATION OPTION .....	iii
ABSTRACT.....	iv
ACKNOWLEDGMENTS .....	v
LIST OF FIGURES .....	xii
LIST OF TABLES .....	xvi
 SECTION	
1. INTRODUCTION.....	1
1.1. RESEARCH SCOPE AND CONTRIBUTIONS .....	4
1.2. DISSERTATION OUTLINE .....	5
2. STATE OF KNOWLEDGE.....	7
2.1. CRYSTAL STRUCTURE AND PHASE DIAGRAM .....	7
2.2. PROCESSING OF ZIRCONIUM CARBIDE CERAMICS .....	10
2.2.1. Solid Phase Reaction.....	10
2.2.2. Solution Based Fabrication.....	11
2.2.3. Vapor Phase Fabrication.....	12
2.3. THERMOMECHANICAL PROPERTIES .....	13
2.4. MAJOR DEGRADATION MODES.....	15
2.4.1. Radiation Damage.....	15
2.4.2. Chemical Compatibility with Coolant.....	22
2.4.3. Air Ingress Accident.....	23

2.4.4. Other Degradation Mechanisms .....	27
---	----

## PAPER

I. THE ION IRRADIATION RESPONSE OF ZrC CERAMICS AT 800 °C .....	28
ABSTRACT .....	28
1. INTRODUCTION .....	29
2. EXPERIMENTAL PROCEDURE AND METHODS .....	33
2.1. SAMPLE PREPARATION .....	33
2.2. ION IRRADIATION .....	34
2.3. MATERIAL CHARACTERIZATION .....	36
2.3.1. Grazing Incidence X-Ray Diffraction (GIXRD).....	36
2.3.2. Line Profile Analysis.....	37
2.4. ELECTRON MICROSCOPY .....	37
2.5. RAMAN SPECTROSCOPY .....	38
3. RESULTS AND DISCUSSION .....	39
3.1. CONTROL SPECIMEN.....	39
3.2. IRRADIATED SPECIMENS .....	41
3.2.1. GIXRD and TEM Analysis.....	41
3.2.2. Raman Spectroscopy.....	46
4. CONCLUSIONS .....	47
ACKNOWLEDGEMENTS .....	48
REFERENCES .....	54
II. EARLY STAGE OXIDATION OF ZrC <sub>x</sub> UNDER ION IRRADIATION AT ELEVATED TEMPERATURES .....	60

ABSTRACT .....	60
1. INTRODUCTION .....	61
2. EXPERIMENTAL PROCEDURE .....	66
2.1. SAMPLE PREPARATION .....	66
2.2. ION IRRADIATIONS .....	66
2.3. MATERIAL CHARACTERIZATION .....	69
2.3.1. Density and Chemical Analysis. ....	69
2.3.2. Grazing Incidence X-Ray Diffraction (GIXRD). ....	69
2.3.3. Electron Microscopy. ....	69
3. RESULTS .....	71
3.1. AS-SINTERED SAMPLE .....	71
3.2. ANNEALED UNIRRADIATED SAMPLE .....	71
3.3. IRRADIATED SAMPLES .....	76
4. DISCUSSION .....	78
4.1. EARLY STAGE OXIDATION .....	78
4.2. OXIDATION UNDER IRRADIATION CONDITIONS .....	82
5. CONCLUSIONS .....	86
ACKNOWLEDGEMENTS .....	87
REFERENCES .....	95
III. SEQUENTIAL ION IRRADIATION ZIRCONIUM CARBIDE CERAMICS: MICROSTRUCTURAL ANALYSIS .....	102
ABSTRACT .....	102
1. INTRODUCTION .....	103
2. MATERIALS AND METHODS .....	107



2.1. SAMPLE PREPARATION .....	107
2.1.1. Synthesis of ZrO <sub>2</sub> Precursor. ....	107
2.1.2. Synthesis of ZrC Powder.....	108
2.1.3. Densification. ....	108
2.2. ION IMPLANTATION .....	109
2.3. MATERIAL CHARACTERIZATION .....	110
2.3.1. Density and Chemical Analysis. ....	111
2.3.2. Grazing Incidence X-Ray Diffraction (GIXRD).....	111
2.3.3. Raman Spectroscopy. ....	111
2.3.4. Electron Microscopy. ....	112
3. RESULTS.....	113
3.1. DENSITY AND CHEMICAL ANALYSIS .....	113
3.2. GRAZING INCIDENCE X-RAY DIFFRACTION.....	113
3.3. RAMAN SPECTROSCOPY .....	114
3.4. TEM ANALYSIS .....	114
3.4.1. Electron Beam Irradiation. ....	115
3.4.1.1. Ion irradiated ZrC grain . ....	115
3.4.1.2. Unirradiated ZrC grain .....	117
3.4.2. EELS Analysis. ....	118
4. DISCUSSION .....	119
4.1. ION IRRADIATED .....	119
4.2. ELECTRON IRRADIATED .....	120
5. CONCLUSIONS .....	126

ACKNOWLEDGEMENTS .....	127
REFERENCES .....	133
SECTION	
3. SUMMARY AND CONCLUSIONS .....	138
4. FUTURE WORK .....	142
APPENDIX .....	144
REFERENCES .....	173
VITA .....	179

## LIST OF FIGURES

SECTION	Page
Figure 1.1. Temperature and dose for in-core structural materials for the operation of six proposed Gen- IV advanced reactor concepts.....	2
Figure 2.1. 3D representation of ZrC crystal structure .....	8
Figure 2.2. Calculated phase diagram of Zr-C system.....	9
Figure 2.3. Thermal conductivity of ZrC as a function of temperature.....	14
Figure 2.4. Historic irradiation data on $ZrC_x$ compare to operating fuel temperature. DPA range data represented by bars, where appropriate, n: neutrons, Kr: Krypton ions, Au: gold ions, P: proton ions.....	16
Figure 2.5. Stages of the oxidation of hot-pressed (H.P.) specimens of ZrC: at 800 and 900 °C in atmospheric air.....	26
 PAPER I	
Figure 1. Depth profile of damage level using SRIM Kinchin and Pease calculations, and Au concentration as a function of depth for a fluence of $3.59 \times 10^{15} \text{ cm}^{-2}$ .....	49
Figure 2. The scattering depth, $\Lambda$ , from which diffraction data was collected as a function of the x-ray incident angle for two diffraction peaks, (111) and (400).....	49
Figure 3. (a) GIXRD obtained from ZrC after thermal annealing in the ion irradiation chamber at 800 °C, collected at various x-ray incident angles. (b) An enlarged view of the most intense (111) ZrC diffraction maxima.....	50
Figure 4. (a) Heterogeneous microstrain of control sample determined using Williamson–Hall plots as a function of the X-ray incident angle. (b) Unit cell parameter of ZrC for the control specimen as a function X-ray incident angle.....	50
Figure 5. A secondary electron SEM image of the surface topography showing $ZrO_2$ nanometric nodules.....	51

Figure 6.	GIXRD patterns of ZrC after irradiation with 10 MeV Au <sup>3+</sup> ions to different doses showing (a) the entire pattern and (b) an enlarged view of the (111) diffraction peak.....	51
Figure 7.	(a) Williamson-Hall plots of the representative XRD data from irradiated ZrC. (b) Williamson-Hall plot of the specimen irradiated to 2.5 dpa.....	52
Figure 8.	(a) Heterogeneous microstrain determined using Williamson–Hall plots as a function of dose, (b) Changes in the unit cell parameter of ZrC as a function of dose .....	52
Figure 9.	(a) On-Zone STEM Bright Field Image of the specimen irradiated to 0.5 dpa, (b) Brighth Field Image of the specimen irradiated to 5 dpa, (c) Bright Field Image of the specimen irradiated to 30 dpa .....	53
Figure 10.	Raman spectra for ZrC irradiated at various doses.....	54
PAPER II		
Figure 1.	Pressure and temperature evolution of the ion chamber before to the onset of ion irradiation.....	89
Figure 2.	(a) GIXRD patterns obtained from ZrC control sample before and after thermal annealing in the ion irradiation chamber at 800 °C, (b) GIXRD obtained from annealed ZrC sample at various x-ray incident angles.....	89
Figure 3.	(a) Secondary electron SEM image of the surface topography of the control sample, (b) EDX compositional maps for C, Zr and O acquired in the box area in (a), (c) EDX spectra and strandardless compositional quantification for the mapping area.....	90
Figure 4.	(a) HRTEM image of the near surface area of the control specimen after annealing in the irradiation chamber (b) STEM-HAADF image with the EELS line profile. Two EELS spectrum are extracted from the spot A and spot B from the line profile, shown in the (c) and (d) respectively. Elemental line profile of Zr (e) and O (f).....	90
Figure 5.	(a) HRTEM image of a precipitate embedded in the ZrC matrix. (b) FFT pattern from the red squared region in (a), (c) The simulated electron diffraction pattern based on the tetragonal structure, (d) EELS spectrum from the precipitate, confirming it is ZrO <sub>2</sub> . (e) FFT pattern from both ZrC and precipitate ZrO <sub>2</sub> .....	91

Figure 6.	Morphology of the nanostructured ZrO <sub>2</sub> nanoparticles obtained by SEM as a function of irradiation dose (a) Control sample, (b) 2.5 dpa, (c) 10 dpa, (d) 15 dpa. Statistical histograms of the oxide islands for each sample are reported below the SEM micrographs.....	91
Figure 7.	HRTEM images of oxide island formed (a) control sample, and samples irradiated to (b) 0.5 dpa, (c) and (d) 2.5 dpa, (e) 5 dpa, and (f) 15 dpa.....	92
Figure 8.	Cavity morphology in the ZrO <sub>2</sub> island after irradiation to 5 dpa (a) in-focus, (b) underfocused, and (c) overfocused BF-TEM images .....	92
Figure 9.	Schematic model of the early oxide growth a) without ion irradiation, and b) under ion-irradiation conditions.....	93
PAPER III		
Figure 1.	Depth profile of damage level, and Au concentration as a function of depth for a fluence of $3.59 \times 10^{15} \text{ cm}^{-2}$ .....	128
Figure 2.	GIXRD diffraction patterns obtained from ZrC a) before, and b) after ion irradiation at room temperature.....	128
Figure 3.	Raman spectra for the pristine and ion irradiated specimens.....	129
Figure 4.	(a) Bright field overview of the ion irradiated ZrC along [110] zone axis, and (b) magnified bright field image.....	129
Figure 5.	SAD pattern from ion irradiated ZrC (a) initially, (b) after 30 min, and (c) after 60 min of electron irradiation; (d) dark field image after 60 min of electron beam exposure.....	130
Figure 6.	(a) HR-TEM image and (b) FFT pattern of the ion irradiated area after 60 min of electron beam exposure; (c) Experimental FFT of precipitate (red box) and simulated electron diffraction.....	130
Figure 7.	(a) SAD pattern from the ion irradiated ZrC area after 100 min of electron beam exposure, (b) overview dark field image after electron irradiation; (c) SAD pattern acquired in the ion irradiated area adjacent to the e-beam irradiated region.....	131
Figure 8.	Figure 8. (a) Bright field micrograph of the pristine ZrC grain; (b) EELS spectra of pristine ZrC grain after e-beam exposure; SAD pattern from pristine (c) initially, (d) after 30 min, and (e) after 60 min of electron irradiation.....	131

Figure 9.	EELS spectrum from ZrC grains obtained (a) from the pristine area, (b) ion-irradiated area, and (c) ion-implanted area after 100 min of electron beam exposure.....	132
Figure 10.	(a) Maximum energy transfer to atoms by electrons, (b) maximum energy transfer to Zr atoms by primary carbon and oxygen recoils.....	132

**LIST OF TABLES**

PAPER II		Page
Table 1.	Statistical data related to the morphology and distribution of the oxide nanoislands as a function of irradiation dose.....	88
Table 2.	Pre-annealing, irradiation and post-annealing times for each specimen.....	88

## **SECTION**

### **1. INTRODUCTION**

Energy is an essential commodity for many economic activities in modern society. According to the 2019 International Energy Outlook report [1], it was estimated that more than 600 quadrillion British thermal units (qBTU) of energy were consumed worldwide in 2018, and the global energy demand is expected to double by 2050. Traditionally, most of the energetic needs in the modern world have been satisfied through the combustion of non-renewable fossil fuels such as gas, coal, and oil. However, the rapid consumption of fossil fuels has caused not only a global depletion of natural resources, but also serious environmental and public health problems. As the global energy demand continues to increase, and as the climate impacts of fossil fuel-based energy sources become untenable, increasing emphasis is being placed on alternative sources of energy. In this context, nuclear energy has emerged over the past five decades to become a reliable baseload source of clean and economical energy.

Due to the renascent interest in nuclear energy, several initiatives have been launched around the world aimed to design and implement new nuclear energy systems that will significantly improve safety and reliability, sustainability, useful reactor life, proliferation-resistance and profitability with respect to current nuclear power reactors. Among these programs, the Generation-IV initiative [2] has identified six advanced nuclear energy systems with the greatest potential to fulfill the above requirements. The six systems chosen include the gas-cooled fast reactor (GFR), the lead-cooled fast reactor (LFR), the molten-salt cooled reactor (MSR), the sodium-cooled fast reactor (SFR), the



supercritical water-cooled reactor (SCWR), and the very high temperature reactor (VHTR) [3]. Despite the promising attributes of Gen-IV nuclear reactors, there are significant challenges on materials and component developments that need to be addressed for successful implementation of these new reactors systems. The core of Gen-IV nuclear reactors presents an exceptionally harsh environment for materials because of the combination of high temperature, high stresses, a chemically aggressive coolant and intense radiation fluxes. Figure. 1.1 shows the temperature and dose requirements for in-core structural material for the operation of Gen-IV reactors.

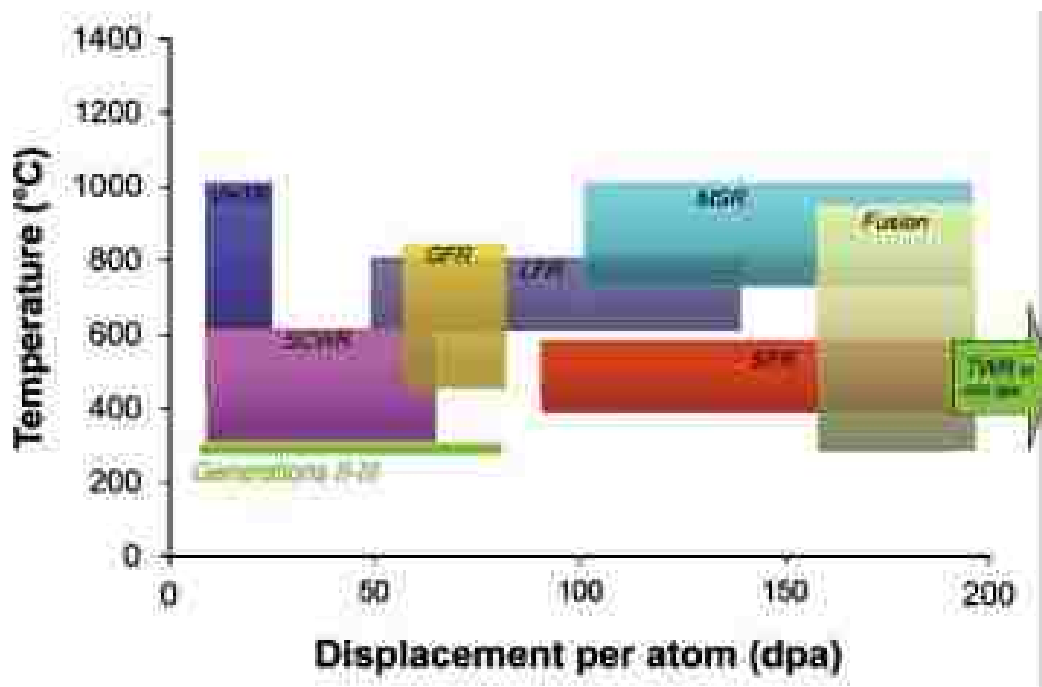


Figure 1.1. Temperature and dose for in-core structural materials for the operation of six proposed Generation IV advanced reactor concepts. Taken from [4]

It is noted that all the new reactor designs will operate at higher temperatures and doses compared to current light water reactor systems (LWRs-Gen II Reactors). These extreme conditions are beyond the capabilities of the existing structural material used in current nuclear reactors. Therefore, it is necessary to look at new material options to meet the operational requirements of Gen-IV reactors.

A range of different materials are currently under investigation for structural and fuel applications in Gen-IV nuclear reactors including refractory metals, oxide dispersion-strengthened (ODS) alloys [5], [6], ferritic-martensitic steels [7], nickel superalloys [8], and non-oxide ceramics [9]. Particularly, the family of transition metal carbides and nitrides exhibit properties that make them attractive for advanced nuclear reactors operating at temperatures above 800 °C (VHTR, GFR and MSR). Foremost of these properties are good thermal conductivity, high refractoriness, phase stability, and radiation resistance [10]. Among the family of transition metal carbides, zirconium carbide ( $\text{ZrC}_x$ ) has received considerable attention as a major contender for future applications in advanced nuclear energy systems.  $\text{ZrC}_x$  could be potentially used as an inert fuel matrix material for GFRs [11], as an oxygen getter for microencapsulated fuels [12], as an alternative cladding for advanced non-light water reactors [13], and as a fission product barrier in Tri-structural Isotropic (TRISO) fuel particles [14].

The successful deployment of  $\text{ZrC}_x$  in advanced Gen IV fission reactors requires a thorough understanding of the changes in performance and structure associated with the simultaneous exposure to ionizing and energetic radiation, high temperature, and chemically challenging environments. Although there exists some historical data on the performance of  $\text{ZrC}_x$  ceramics in high temperature nuclear reactors, the radiation

response of  $\text{ZrC}_x$  is still poorly understood. Therefore, any attempt to contribute to the understanding of the fundamentals of radiation damage in  $\text{ZrC}_x$  is helpful for the scientific community studying radiation effects in ceramics and for the nuclear industry

## 1.1. RESEARCH SCOPE AND CONTRIBUTIONS

Studying radiation damage in  $\text{ZrC}_x$  is a broad research topic. In order to make the objectives of this work more focused, and achievable, this research is particularly concerned with investigating the microstructural evolution of  $\text{ZrC}_x$  ceramics under ion and electron irradiation conditions. In the first part of the thesis, efforts were made to characterize the microstructure of  $\text{ZrC}_x$  irradiated with 10 MeV  $\text{Au}^{3+}$  ions up to doses of 30 displacements per atom (dpa) at 800 °C. To date, most of the studies on irradiated  $\text{ZrC}_x$  have only focused on the low dose (< 5 dpa), low temperature (25 °C) irradiation regime. Thus, the results of the first part of the dissertation extends the current state of knowledge of the irradiation response of  $\text{ZrC}_x$  at conditions that are relevant to the operation of advanced Gen-IV gas-cooled nuclear reactors. In the second part of the dissertation, the microstructural evolution of  $\text{ZrC}_x$  under sequential ion-electron irradiation conditions was investigated. To the best of our knowledge, no previous studies have investigated the sequential irradiation of  $\text{ZrC}$ . Thus, the second part of the dissertation provides new knowledge of the microstructural response of  $\text{ZrC}_x$  to different types of radiation. It also gives new insights into the inadvertent effects of the electron beam irradiation during TEM analysis of *in-situ* and *ex-situ* ion irradiated  $\text{ZrC}_x$ .

## 1.2. DISSERTATION OUTLINE

This dissertation is structured based on the manuscripts that have been prepared for submission to peer-review journals. The dissertation is partitioned into the following sections:

**Section 2:** A literature review that provides a detailed background on the degradation mode of ZrC in nuclear systems is presented. The aim of this section is to identify the current existing knowledge gaps.

**Papers:** The papers section contains the three manuscripts about the experiments that were conducted in this research. The first paper presents a detailed multiscale microstructural characterization of  $\text{ZrC}_x$  irradiated with 10 MeV  $\text{Au}^{3+}$  ions at 800 °C. This paper identified specific relationships between irradiation dose and final microstructure, showing how the microstructure of  $\text{ZrC}_x$  ceramics evolves at different length scales under irradiation conditions relevant to the operation of high temperature nuclear reactors. The results presented expands the current state of knowledge on the irradiation behavior of  $\text{ZrC}_x$  at doses above 5 dpa and high temperatures (800 °C), where only a limited number of studies have been conducted.

The second paper focuses on the early stage oxidation behavior of  $\text{ZrC}_x$  under irradiation conditions. Here, a detailed microstructural and morphological analysis of the  $\text{ZrO}_2$  nodules formed during ion-irradiation of  $\text{ZrC}_x$  at 800 °C is presented. To the best of our knowledge, no previous studies have focused on in-pile oxidation of  $\text{ZrC}_x$ . Therefore, the results presented in this paper are the first ones to shed light on the complex in-service oxidation of  $\text{ZrC}_x$  in high temperature nuclear reactors. This information will enable better design and safe operation of the next generation of nuclear power systems.

The third paper deals with the sequential ion-electron irradiation of  $\text{ZrC}_x$  at room temperature. This article provides new knowledge of the microstructural response of  $\text{ZrC}_x$  to different types of radiation and new insights into the inadvertent effects of electron beam during TEM analysis of *in-situ* and *ex-situ* ion irradiated  $\text{ZrC}_x$ .

**Section 3 and 4:** Conclusions and Future work presents a summary of the work and discusses the main findings of the thesis. This section also outlines key directions for future experimental work.

**Appendix:** This appendix contains the fourth paper, which investigated the microstructural characterization of a ZrC billet with low Hf-content. This article discusses the significance of employing a multiprobe approach to characterize the microstructural inhomogeneities in  $\text{ZrC}_x$  ceramics, Furthermore, the results of this work provide new insights into role of the main impurities on the microstructural evolution of  $\text{ZrC}_x$  ceramics during densification.

## 2. STATE OF KNOWLEDGE

Due to its high melting temperature of  $T_m=3420\text{ }^{\circ}\text{C}$  [15], zirconium carbide ( $\text{ZrC}_x$ ) belongs to a group of materials classified as ultra-high temperature ceramics (UHTCs), a family of binary borides, nitrides, and carbides compounds that have melting points above  $3000\text{ }^{\circ}\text{C}$  [16].  $\text{ZrC}_x$  ceramics also exhibits higher electrical and thermal conductivities [17], outstanding mechanical properties [18], good resistance to fission product attack [19], and a low neutron absorption cross section [20]. This unique combination of properties allows  $\text{ZrC}_x$  to survive extreme temperatures, heat fluxes, radiation levels, mechanical loads, chemical reactivities, and other extreme conditions that are expected to occur in the core of advanced gas cooled nuclear reactors. Therefore,  $\text{ZrC}_x$  is a strong contender for future applications in advanced nuclear energy systems.

The purpose of this section is to review the published research pertaining to the papers presented in section 3. First, an overview of the crystal structure, bonding and phase equilibria of  $\text{ZrC}_x$  is presented. Next, the fabrication methods of  $\text{ZrC}_x$  ceramics are briefly reviewed and the major gaps existing in the evaluation of the thermophysical properties of  $\text{ZrC}_x$  are listed. Finally, the major degradation modes of  $\text{ZrC}_x$  ceramics in advanced gas-cooled nuclear reactors are discussed.

### 2.1. CRYSTAL STRUCTURE AND PHASE DIAGRAM

Zirconium Carbide ( $\text{ZrC}_x$ ) is a group IVb transition metal compound that crystallizes in the rocksalt  $Fm3m$  structure (space group 225) [20]. A schematic representation of the crystalline structure of  $\text{ZrC}_x$  is depicted in Figure 2.1. The crystal

structure can be described as a face-centered cubic (FCC) Bravais lattice with a basis consisting of a Zr atom at (0,0,0) and a C atom at the position  $a/2(1,0,0)$ . In this structure, the Zr atoms form a metallic FCC sublattice whose octahedral interstitial sites host C atoms. The crystal structure leads to a combination of covalent, ionic, and metallic bonding. The ionic character of the bonding arises because of the difference in electronegativity between C and Zr atoms, the covalent character is due to the interactions between the 2p state of carbon and 4d state of Zr, and the metallic bonding arises when atoms are ionized, producing positive Zr atoms and delocalized electrons [21]. This combination of bonding types gives  $\text{ZrC}_x$  an unique mixture of properties including high hardness ( $\sim 25$  GPa), very high melting point ( $>3000$  K), and high thermal and electrical conductivities ( $>10 \text{ W m}^{-1} \text{ K}^{-1}$  and  $\sim 200 \times 10^4 \Omega^{-1} \text{ m}^{-1}$  respectively).

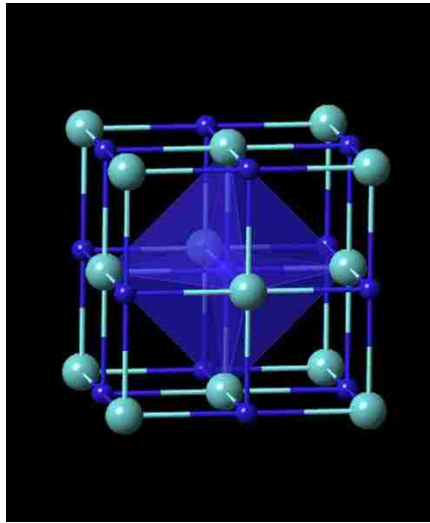


Figure 2.1. 3D representation of ZrC crystal structure [22].

Zirconium carbide can deviate significantly from its stoichiometric composition with the formation of structural vacancies in the carbon sublattice. The phase diagram of the Zr-C system is shown in Figure 2.2. The phase diagram shows the existence of the  $\text{ZrC}_x$  phase between  $\sim 37.5$  and  $49.5$  at.% C, where  $x$  is between  $0.6$  and  $0.98$ , with the congruent melting of the  $\text{ZrC}_x$  phase at  $3723$  K. Below  $\sim 37.5$  at.% C, a hexagonal close packed Zr and  $\text{ZrC}_x$  coexist field exists until  $\sim 1200$  K, where the Zr metal becomes body centered cubic. This phase begins melting at  $\sim 2030$  K resulting in liquid Zr and solid  $\text{ZrC}_x$ . For carbon contents higher than  $49.5$  at.%, a mixture of  $\text{ZrC}_x + \text{C}$  phases forms.

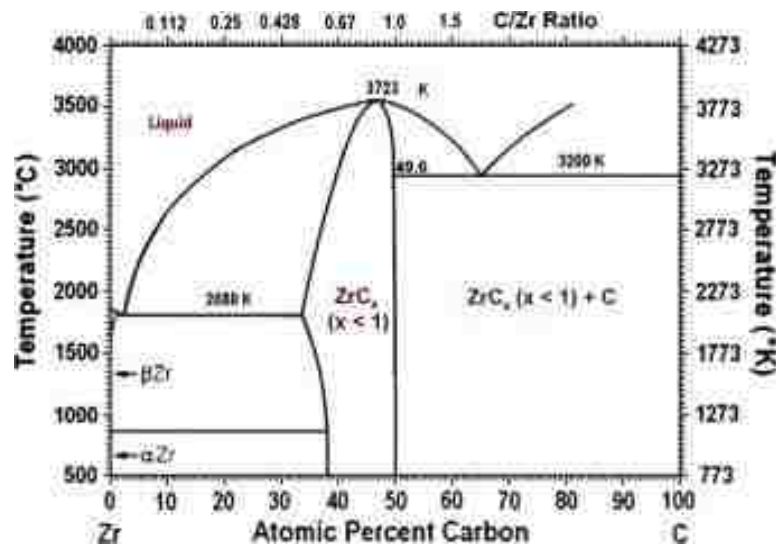


Figure 2.2. Calculated phase diagram of Zr-C system. Taken from [20].

As a characteristic non-stoichiometric compound,  $\text{ZrC}_x$  exhibits both short-range ordering (SRO) and long-range ordering (LRO) for the carbon vacancy distribution [23].



Ordered  $\text{ZrC}_x$  phases are usually obtained by long-duration post annealing treatments [24]. However, vacancy-ordered structures with new symmetry can be also obtained by direct routes such as high temperature chain–reaction synthesis at  $\text{ZrC}_{0.6-0.74}$  [25] or spark plasma sintering (SPS) of  $\text{ZrC}_{0.61}$  nano-powders [26]. The mechanisms driving vacancy ordering are still largely unstudied. Likewise, accurate phase identification of the vacancy-ordered variants of  $\text{ZrC}_x$  is difficult in experiments due to the lack of high quality  $\text{ZrC}_x$  samples and proper characterization techniques [27]. Despite that, the existence of ordered vacancy configurations is exciting from an engineering standpoint because it provides the opportunity to fabricate new materials through engineering of chemical composition and vacancy configurations.

## 2.2. PROCESSING OF ZIRCONIUM CARBIDE CERAMICS

$\text{ZrC}_x$  can be produced by solid phase reactions [28], [29], from solution based precursors [30], and through vapor phase reaction methods such as chemical vapor deposition [31], [32]. Various fabrication techniques can provide samples with varying characteristics including microstructure, chemical composition, and impurity species.

**2.2.1. Solid Phase Reaction.** Carbothermal reduction of  $\text{ZrO}_2$  powders with elemental carbon (Reaction 1) has historically been the most common route to synthesize zirconium carbide [33], [34]. This method usually requires high temperatures ( $>1800^\circ\text{C}$ ) and long-duration heat treatments ( $>12$  hours) to obtain high purity  $\text{ZrC}_x$  powders. Furthermore, the reaction requires a strictly controlled environment (vacuum or inert gas) to ensure purity of the final product. Due to the tendency for carbon deficiencies, combined with the solubility of oxygen, the carbothermal reduction method often results

in the formation of oxycarbide  $\text{ZrC}_x\text{O}_y$  [28]. The presence of oxygen impurities in the carbon sub-lattice is known to influence both the densification mechanisms and thermomechanical properties of the ceramic [35].



Alternatively, direct reaction of carbon with Zr [11],[36] (Reaction 2) or  $\text{ZrH}_2$  [37] (Reaction 3) is used in cases where higher purity or controlled carbon stoichiometry is desired.

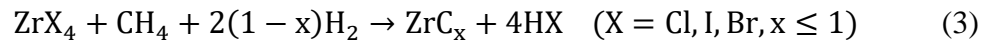


These reactions are classified as combustion synthesis reactions [38]. To produce the  $\text{ZrC}_x$  powders, the reactant mixture is pressed to form a green body and heated to a temperature known as the ignition temperature after which the heat released by the reaction is enough to sustain and drive it to completion. It is essential to maintain the contact between the reactant particles without which the reaction fails to sustain itself. Unlike carbothermal reduction route, combustion synthesis methods pose serious handling issues for bulk production of  $\text{ZrC}_x$ . The limitations are mainly due to the exothermic nature of the combustion reaction and the size of the zirconium reactant, which are highly pyrophoric and susceptible to oxidation at room temperatures.

**2.2.2. Solution Based Fabrication.**  $\text{ZrC}_x$  can also be synthesized by using precursors via solution-based processing methods [39], [40]. The advantage of using a solution-based fabrication route is the high intimacy, at a molecular or colloidal scale, that is achieved between the precursors. This intimate mixing helps to shorten the diffusion distance, decreasing the heat treatment (dwell temperature and duration)

necessary to complete the reaction. The shorter dwell times result in smaller particles sizes compared with traditional solid-state routes. Sol–gel processing is one of the most common solution-based routes used for the fabrication of  $\text{ZrC}_x$  powders. Typically, a polymer containing Zr-O-Zr links is formed from Zr n-propoxide or zirconium oxychloride and a carbon source such as alcohols or sugar. Pyrolysis then results in intimate mixing of  $\text{ZrO}_2$  and C. The production of  $\text{ZrC}_x$  with varying stoichiometry can be achieved by varying the proportion of the reactant precursors. However, the solution based mixing process suffers from the disadvantage of residual oxygen impurities.

**2.2.3. Vapor Phase Fabrication.** Vapor phase reactions are the most common route to produce  $\text{ZrC}_x$  coatings for microencapsulated nuclear fuel concepts such as the TRI-structural ISotropic (TRISO) fuel particles. Given the high melting point of  $\text{ZrC}_x$  ( $T_m > 3000^\circ\text{C}$ ), the coatings are normally deposited by low pressure chemical vapor deposition (LPCVD) [31], evaporation [41], or sputtering [42]. Among these methods, LPCVD is the preferred one to produce high purity, uniform, and defect-free ZrC coatings onto TRISO particles [20]. In this process, a Zr precursor is reacted with  $\text{CH}_4$  in a fluidized bed reactor at temperatures between 1300 and 1500  $^\circ\text{C}$ . Several zirconium halides precursors have been used in this process including chloride, iodide, and bromide. The process can be represented as follows:



The reaction is conducted in an inert environment to prevent the uptake of oxygen and other impurities. Also, the C/Zr compositional ratio and the morphology of the coating can be controlled by varying the flow of methane and hydrogen. Further heat

treatments can also be used to adjust the porosity of the coating. Compared to the solid-state and liquid routes, LPCVD is known to produce high quality  $\text{ZrC}_x$  coatings.

### 2.3. THERMOMECHANICAL PROPERTIES

Thermal and mechanical properties of  $\text{ZrC}_x$  ceramics at room temperature have been extensively studied in the last four decades [17],[20], [43],[44], [45], with the most important properties being strength, hardness, elastic constants, heat capacity, thermal conductivity, and fracture toughness. Despite these assessments, many fundamental properties of  $\text{ZrC}_x$  ceramics remain poorly characterized and discrepancies exist among different studies even in basic properties such as thermal conductivity and strength (Figure. 2.3). The inconsistencies observed in the thermomechanical database for  $\text{ZrC}_x$  ceramics is largely attributed to factors such as impurities, vacancies, porosity, and other microstructural features (grain size, grain boundaries, etc.) that are rarely reported in the literature. Up to now, most of the studies have reported properties for a single ceramic without identifying fundamental factors related to composition, microstructure, porosity, impurities, etc. that can control the observed behavior. Presentation of properties without an understanding of structure-property relations hinders the reporting of accurate thermophysical data. Consequently, more systematic studies are necessary to elucidate microstructure property relationships, isolate fundamental factors that control thermal and mechanical behavior, and report intrinsic properties of  $\text{ZrC}_x$  ceramics.

The literature survey also indicates that most of the thermomechanical testing of  $\text{ZrC}_x$  has been conducted under ambient conditions. While insightful, this information is insufficient to qualify  $\text{ZrC}_x$  as a safe nuclear material for advanced gas-cooled reactors

that will operate at temperatures above 600 °C. Therefore, further experimental work is required to establish a comprehensive database of the thermal and mechanical properties of  $\text{ZrC}_x$  at elevated temperatures.

It is necessary to evaluate the thermal and mechanical properties experimentally because a simple extrapolation of the properties from room temperature to high temperatures might not take into account potential non-linear behavioral trends, which could be caused by phenomena such as phase changes, creep, softening of grain boundary/impurity phases, sub-critical crack growth, or stress-induced microcracking at high temperature.

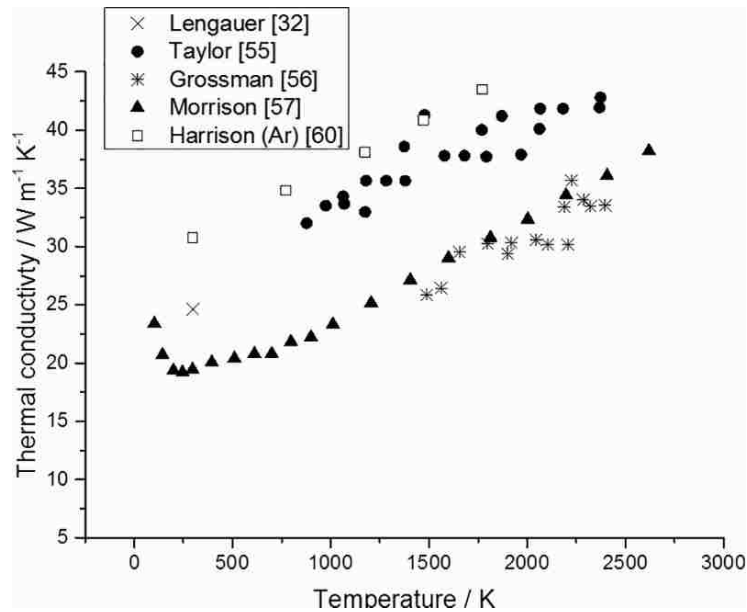


Figure 2.3. Thermal conductivity of  $\text{ZrC}$  as a function of temperature. Taken from [21].

Additionally, systematic research on the effects of C/Zr ratio on the elevated temperature thermophysical properties of  $\text{ZrC}_x$  is needed. A substantial influence of stoichiometry of  $\text{ZrC}_x$  on elevated temperature properties is anticipated; however, very limited data is available in this regard.

## **2.4. MAJOR DEGRADATION MODES**

Several environmental degradation mechanisms are encountered in the core of advanced gas-cooled nuclear reactors including radiation damage and oxidation. A literature review on the main degradation mechanisms is here presented.

**2.4.1. Radiation Damage.** Despite having practical knowledge of the performance of  $\text{ZrC}_x$  ceramics under irradiation conditions, the radiation response mechanisms of  $\text{ZrC}_x$  are still largely unexplored, with systematic studies only emerging in the literature within the last two decades. Understanding these mechanisms will allow for the development of phenomenological and mechanistic models, which can reduce the number of validation irradiations required in real reactor conditions and provide more reliable predictions outside of the validation domain. A summary of the historic irradiation data on  $\text{ZrC}_x$  ceramics is presented in Figure 2.4 [46]. From this figure, it is clear that most of the studies to date have only focused on the low dose, low temperature irradiation regime. Although these data has furthered the state of the knowledge about the radiation response of  $\text{ZrC}_x$ , more research is needed on the effects of neutron and ion irradiation at high temperatures ( $>800\text{ }^\circ\text{C}$ ) and higher doses ( $>5\text{ dpa}$ ) as these are the general requirements for materials in advanced nuclear fission reactors.

Early studies on the neutron-irradiation behavior of  $\text{ZrC}_x$ , at temperatures ranging from 300 to 700°C, were reported by Keilholtz *et al.* [47]. This work investigated the irradiation response of three types of powder processed  $\text{ZrC}_x$  materials in a strongly carbon-rich condition (C/Zr ranging from 1.08 to 1.27) and low density (ranging from 70% to 95% theoretical). Although the fabrication routes for each specimen were described in the paper, the details of the quality of the materials and pre-irradiation microstructures were not reported. Keilholtz found gross volume swelling (dimensional changes) in the range of 2–2.7% for three samples.

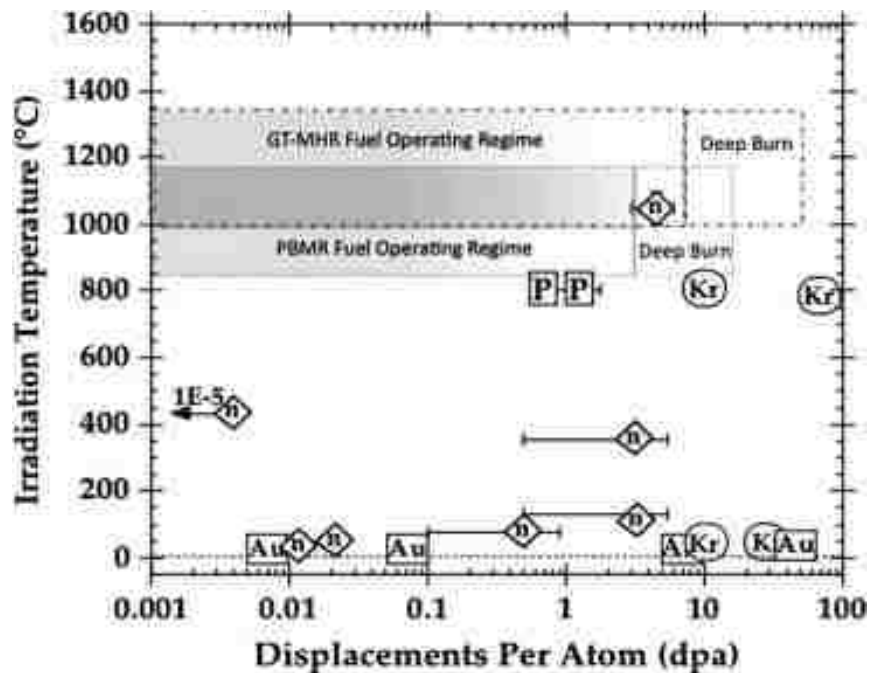


Figure 2.4. Historic irradiation data on  $\text{ZrC}_x$  compared to operating fuel temperature. DPA range data is represented by bars, where appropriate, n: neutrons, Kr: krypton ions, Au: gold ions, P: proton ions. Taken from [46]

Reynolds *et al.* [48] irradiated four experimental fuel particle types based on zirconium carbide with fast neutrons ( $E > 0.18$  MeV) at 1200 °C up to  $5 \times 10^{21} \text{ cm}^{-2}$ . Post-irradiation examination by stereoscopic, metallographic and electron-beam microprobe analysis of the irradiated particles indicated that ZrC possesses exceptional resistance to chemical attack by fission products and good mechanical stability under irradiation.

Recently, Snead *et al.* [46] reported the effects of fast neutron irradiation on the properties of high purity zone-refined  $\text{ZrC}_{0.87}$ . The samples were irradiated in the High Flux Isotope Reactor (HFR) at Oak Ridge National Laboratory (ORNL) to fluences ranging from 1 to  $10 \times 10^{25} \text{ m}^{-2}$  ( $E > 0.1$  MeV) in the irradiation temperature range of  $\sim 910$ – $1750$  K. Small unidentified dislocation loops aligned in a raft-like structure were observed by TEM analysis in samples irradiated at  $\sim 910$  K and a fast fluence  $\sim 4 \times 10^{25} \text{ cm}^{-2}$ . As the temperature increased to  $\sim 1295$  K, formation of larger Frank faulted loops was reported. The microstructure of the samples irradiated at  $\sim 1530$  K contained both distinct Frank loops and other unidentifiable dislocation loops. As the irradiation temperature increased, a transition from Frank loops to prismatic loops was reported. The changes in lattice parameter determined by X-ray diffraction were within the measurement error and the corresponding macroscopic swelling due to lattice expansion were reportedly less than 0.1%. Though the substantial variation in lattice parameter in non-irradiated samples prohibited accurate determination of lattice swelling, the linear lattice expansion appeared to be less than  $\sim 0.03\%$  at all temperatures.

Several studies have conducted proton irradiation of  $\text{ZrC}_x$  at high temperatures. Yang *et al.* [49] reported the effect of proton irradiation (2.6 MeV) on the microstructure



of  $\text{ZrC}_{1.01}$  irradiated to a dose of 0.7 and 1.5 dpa at  $\sim 800^\circ\text{C}$ . Post-irradiation characterization with TEM indicated the formation of high-density nano-sized dislocation loops with densities increasing with irradiation dose. Yang also reported a change in the lattice parameter with irradiation dose of 0.09 and 0.11% for 0.7 and 1.5 dpa respectively. Similar results were obtained by Gan *et al.*[50] on post-irradiation examination of hot-pressed  $\text{ZrC}_{1.01}$  ( $\sim 100\%$  theoretical density) irradiated by 2.6 MeV protons up to 0.71–1.8 dpa at  $800^\circ\text{C}$ . Huang *et al.* [51] investigated the effect of stoichiometry on the damage evolution in proton-irradiated  $\text{ZrC}_x$  ( $0.9 < x < 1.2$ ) up to 3 dpa at  $800^\circ\text{C}$ . It was found that the loop size and density were both dependent on dose and stoichiometry. For substoichiometric compositions, little variation in the diameter of the dislocation loops was observed for different C/Zr ratios. However, for superstoichiometric compositions, the defect size and density increased in the vicinity of the graphite precipitates as a function of carbon content. This suggests that other mechanisms for defect nucleation or growth may occur in superstoichiometric  $\text{ZrC}_x$ . More research is needed to investigate the irradiation response of  $\text{ZrC}_x$  in carbon rich regions.

Heavy ion irradiations have been also used to investigate the effects of irradiation on  $\text{ZrC}_x$ . The seminal work by Gosset *et al.*[122] reported the microstructural evolution in hot pressed ZrC subject to 4 MeV Au ion irradiation at room temperature. The ion fluence was between  $10^{11}$  and  $5 \times 10^{15} \text{cm}^{-2}$ . Three damage stages were identified using a combination of TEM and XRD analysis. At low fluences ( $< 10^{11} \text{cm}^{-2}$ ), no significant damage to the microstructure and minimal swelling were observed. However, in the intermediate fluence range ( $< 10^{14} \text{cm}^{-2}$ ), formation of high-density dislocation loops and appearance of microstrain was reported. Swelling saturation (0.6%) was observed at a

fluence close to  $\sim 10^{14} \text{ cm}^{-2}$ . With fluences  $> 10^{15} \text{ cm}^{-2}$ , the growth of these loops led to the formation of a high-density dislocation network via loop interactions. Further interactions of this dislocation network with defects were cited as the reason for swelling saturation beyond  $10^{14} \text{ cm}^{-2}$ .

Gan *et al.* [52] irradiated  $\text{ZrC}_x$  with 1 MeV Kr ions to doses of 10 and 30 dpa at 27 °C, and 10 to 70 dpa at 800 °C in the Intermediate Voltage Electron Microscope (IVEM) at Argonne National Laboratory (ANL). Faulted dislocations loops were observed in all irradiated samples. Irradiations of ZrC to doses of 10 dpa and 30 dpa at 27 °C caused a 0.7 and 0.9 % lattice expansion respectively. Irradiation at 800 °C produced lattice expansion of approximately 0.6% at 10 dpa and 7% at 70 dpa. The large lattice expansion observed in the sample irradiated to 70 dpa at 800 °C was attributed to the formation of precipitate type defect features, which were believed to be face centered cubic (FCC) ZrC with a lattice constant 8% greater than that of irradiated ZrC. The formation mechanisms of the nanoprecipitates was not investigated by the authors.

Recently, Ulmer *et al.* [53] investigated the microstructural evolution of  $\text{ZrC}_x$  under in-situ ion irradiation conditions using the IVEM at Argonne National Laboratory. The irradiation response of  $\text{ZrC}_x$  was separated into two different regimes depending on the irradiation temperature: low temperature (25 °C and below) and high temperature (600 °C and higher). During low temperature irradiation, damage was observed in the form of black-dot damage. The damage appeared after a threshold dose and increased gradually with dose until saturation. In the high temperature regime (600 °C and higher), ion irradiation resulted in the formation of dislocation loops at doses above 1 dpa. Gradual coarsening of the microstructure through defect coalescence was observed as

dose increased, which led to the formation of entangled dislocation networks at doses above 5 dpa. Ulmer also observed the formation of nanoprecipitates as a result of Kr irradiation. The ring pattern of the nanoprecipitates was indexed and was consistent with a FCC crystal structure with a lattice parameter 8% larger than that of ZrC. No explanation was provided in this work concerning the formation mechanism of the nanoprecipitates.

Pellegrino *et al.* [54], [55] also examined the microstructure of single crystal  $\text{ZrC}_x$  irradiated with 1.2 MeV Au ions at room temperature. The evolution of the microstructure as a function of dose was investigated using RBS/C, XRD and TEM techniques. The results were interpreted in the framework of a two-step damage process with an increase of the elastic strain in the first step followed by a sharp release of strain in the second step, accompanied with the appearance of TEM visible damage and large RSB-C dechannelling. The critical dose level for the transition was identified to be 2.2 dpa for Au ions in ZrC. Similar irradiation response has been observed in other non-amorphizable ceramics such as  $\text{ZrO}_2$  and  $\text{UO}_2$ .

Computational methods have been also applied to investigate radiation damage in  $\text{ZrC}_x$  ceramics. Zheng *et al.* [56] predicted the threshold displacement energy ( $E_d$ ) of C and Zr atoms in ZrC using *ab initio* molecular dynamics simulation. Averaged values of 16 eV and 37 eV were obtained for the C and Zr sublattices respectively. The effect of the presence of C vacancies on the displacement energies was also investigated. It was found that a neighboring vacancy can increase the values of  $E_d$ , although the increment is minimal (~4 eV) and only along one crystallographic direction. Jiang *et al.* [57] used *ab initio* molecular dynamics simulations to compare the response of SiC and ZrC to low

energy irradiation. It was proposed that the discrepancy in the resistance to antisite formation between SiC and ZrC contributes to the difference in the irradiation response of the two ceramics. Zheng *et al.*[58] used density functional theory methods to investigate the migration of point defects, recombination of Frenkel pairs (FPs), and resistance to amorphization in ZrC. They found that interstitials have lower migration energy than vacancies, and C defects have higher diffusivity than Zr defects. Additionally, the recombination barrier of C FPs is significantly reduced in the presence of carbon vacancies and the Zr FP recombination has a low barrier. The amorphization process of SiC and ZrC was studied by Jiang *et al.*[59] by adding C Frenkel pairs into both systems. They found that SiC readily amorphized with the addition of defects in the carbon lattice but ZrC did not amorphize. This difference was explained in terms of the intrinsic mechanical instability of the Si sublattice compared with the intrinsic stability of the Zr lattice. Jiang also reported that regardless of the number of C Frenkel pairs added, the point defects did not accumulate to enough energy to destabilize the crystalline ZrC. This behavior suggests that athermal annealing processes are accessible in ZrC with high concentrations of point defects. Classical molecular dynamics (MD) simulations were also used by Brutzel *et al.* [50] to study the primary damage created by collisional cascade in ZrC. No amorphization was observed in the cascades, and the point defects created included C and Zr interstitials, a few Zr antisites, and clusters of two kinds of interstitials.

In summary, the literature review on irradiated  $\text{ZrC}_x$  ceramics shows that  $\text{ZrC}_x$  is not amorphized by ion and neutron irradiations at temperatures between -253 and 900 °C. These experimental observations confirm the superior radiation resistance of  $\text{ZrC}_x$

compared with conventional ceramics such as SiC. The high radiation amorphization resistance of  $\text{ZrC}_x$  ceramics has been also confirmed by ab-initio computational studies. Additionally, no evidence of void formation has been reported in neutron and ion irradiated  $\text{ZrC}_x$  up to doses of 70 dpa and 800 °C, suggesting that vacancies are sessile below 800 °C. TEM analysis of  $\text{ZrC}_x$  irradiated with light and heavy ions at different temperatures shows that the density of radiation-induced defects decreases with temperature, indicating that some degree of radiation defect annealing and/or recovery occurs at higher temperatures. Collectively, these observations indicate that temperatures between 25 and 800 °C in  $\text{ZrC}_x$  correspond to temperatures above stage I (onset for interstitial motion) and below recovery stage III (on-set temperature for vacancy motion). This temperature regime is also known as the “point defect swelling” regime and is characterized by the accumulation of radiation damage until saturation is reached at doses between 0.1 and 1 dpa. The damage saturation is due to the high concentration of immobile vacancies that serve as recombination centers for the migrating interstitials [12].

**2.4.2. Chemical Compatibility with Coolant.** In advanced high temperature gas-cooled reactors, helium gas will be used as a primary coolant. Under normal operation conditions, the helium gas will inevitably contains part per million (ppm) levels of impurities such as CO, CO<sub>2</sub>, H<sub>2</sub>, H<sub>2</sub>O, O<sub>2</sub>, and CH<sub>4</sub>, which arise mainly from in-leakage of O<sub>2</sub>, N<sub>2</sub> and water vapor from seals and welds, and degassing from reactor materials. Depending on the level of impurity concentration, temperature, and material composition, the impurities can react with in-core structural components resulting in a variety of corrosion reactions. Given the high chemical affinity of  $\text{ZrC}_x$  towards oxygen

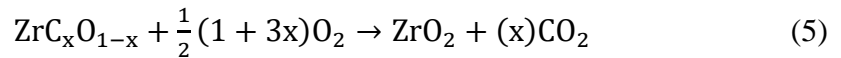
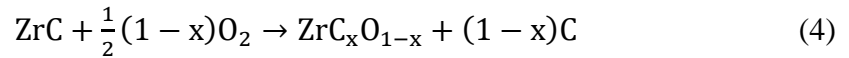
and water vapor impurities, it is possible that in-service oxidation of  $\text{ZrC}_x$  components occurs under normal operation in advanced high temperature gas-cooled reactors. While the oxidation of  $\text{ZrC}_x$  has been extensively studied in non-nuclear contexts, issues that are unique to the reactor environment are the effects of radiation on the oxidation of  $\text{ZrC}_x$ . To the best of our knowledge, no previous studies have investigated the oxidation of  $\text{ZrC}_x$  under prototypical operation conditions of high temperature gas-cooled reactors. Consequently, new experiments need to be conducted to achieve a comprehensive understanding of the in-service oxidation mechanisms of  $\text{ZrC}_x$  and its impact on the material performance. A detailed knowledge of the oxidation mechanism and rates of microstructure degradation is also important to estimate the lifetime of the components and define mitigation strategies.

**2.4.3. Air Ingress Accident.** An air ingress-accident is one of the design basis accidents (DBA) of high temperature gas-cooled reactors [60]. This accident is initiated by a break in the hot duct of the reactor core vessel and can lead to an initial loss of the primary helium coolant by depressurization. Following the depressurization process, the air-helium mixture in the reactor cavity could enter the reactor core producing oxidation of the core components. The air ingress event can last for hours or days, depending on the severity of the accident, and cause the reactor core to become immersed in air atmosphere at temperatures around 1600 °C [61].

A literature survey on the oxidation behavior of  $\text{ZrC}_x$  indicates that it is vulnerable to oxidation and the rate of this process depending on temperature, porosity, partial pressure of oxidative and reductive gas species, carbon content, and impurities [95], [96], [97], [98]. Although it is well established that oxidation does not

affect  $\text{ZrC}_x$  at room temperature, complete spalling can occur due to oxidation at elevated temperatures ( $T > \sim 870$  K), especially in high oxygen partial pressure environments ( $\sim 130$  kPa) [94], [97], [98]. However, at temperatures exceeding  $\sim 1500$  K with sufficient oxygen partial pressures, ZrC is known to passivate and the produced zirconia undergoes limited yet considerable sintering contributing to improved structural integrity in certain conditions [96]. The mechanisms of oxidation of ZrC at temperatures above  $470^\circ\text{C}$  is explained with the following steps:

- The formation of  $\text{ZrO}_x\text{C}_y$ , which proceeds to form amorphous  $\text{ZrO}_2$  and C upon oxygen saturation. The formation of oxycarbide is well expected as oxygen is known to dissolve in  $\text{ZrC}_x$  [62]. The rate of oxycarbide formation is controlled by the phase boundary reaction, especially with oxygen partial pressure  $\sim 100$  kPa [63], [64]. At temperatures below  $600^\circ\text{C}$ , with low oxygen partial pressures ( $< 50$  kPa), the literature supplies evidence of the presence of zirconia and free carbon in the scales [65], [66]. The overall reaction is summarized by [65].



- As the temperature increases ( $> 600^\circ\text{C}$ ), cubic zirconia begins to nucleate from the amorphous zirconia and the crystals start to grow. The stabilization of the c- $\text{ZrO}_2$  polymorph occurs via substitution of  $\text{O}^{2-}$  with  $\text{C}^{3-}$  ions creating oxygen vacancies.
- Oxygen then diffuses through this oxide layer to the free carbon producing

CO<sub>2</sub> with diffuses out via existing pores or cracks, leaving behind pores in the zirconia layer, which with very little carbon left to stabilize transform to monoclinic zirconia (m-ZrO<sub>2</sub>), along with small amounts of tetragonal polymorph (t-ZrO<sub>2</sub>).

- With further increase in the temperature beyond 800 °C, the stress exerted by the growth of m-zirconia at the grain boundaries and the pressure exerted by the increased CO<sub>2</sub> gas initiates inter-crystalline fracture in an already porous layer [67]. In the range of temperature between 800 and 1100 °C, the oxidation behavior of ZrC is quite complex as summarized schematically in Fig 2.5. The oxide formed by oxidation at below 900 °C strongly adhere to the carbide core and is comprised of m- and t/c-ZrO<sub>2</sub> [68]. On the contrary, the oxide scale formed at temperature above 1100 °C shows a gap between ZrC and ZrO<sub>2-x</sub> and the oxide was voluminous and made of m-ZrO<sub>2</sub>. The voluminous and heavily cracked structure of the oxide at 1100 °C demonstrates its nonpassivating nature at this temperature range.

- With temperatures above 1200 °C, the porous zirconia scale (mostly m-ZrO<sub>2</sub>) starts to sinter and densify, acting as a barrier for the diffusing oxygen atoms [67]. Then the CO<sub>2</sub> partial pressure assumes control of oxidation rate as the gas starts to effuse out of the shrinking pores. With most of the paths for oxygen to reach the ZrC substrate blocked by CO<sub>2</sub> and densification of the scale, oxidation turns passive as long as the zirconia scale remains intact. The sintering process also ensures structural stability of the ZrC coating and prevents it from spalling, with considerable reduction in inter-crystalline stresses [67], [69].

Despite the numerous studies on the oxidation behavior of ZrC<sub>x</sub> [70],[71], [72], a clear understanding of this process has not been achieved yet. due to the large numbers



of variables that affect it, such as chemical composition of the initial material (C/Zr stoichiometry), porosity, or grain size [20], [73]. Additionally, most of studies published until now have only investigated the out-of-pile oxidation of ZrC at temperatures relevant to reactor operation. Thus, these studies suffer from major limitations as they do not consider the radiation effects that occur in nuclear reactors. Radiation can affect the oxidation behavior of  $\text{ZrC}_x$  in a number of ways. For example, the interaction between ionizing radiation and coolant impurities can produce a variety oxidizing species that could accelerate the oxidation through an increase in oxidation potential. Likewise, the oxidation rate can be affected by the properties of the oxide layer formed during exposure, including oxide morphology, oxide phase, stress, etc. In the oxide, the displacement of ions from their lattice sites by radiation could lead to enhanced point defect concentrations, enhanced diffusion, which would lead to accelerated oxidation. These mechanisms need to be understood in order to predict the oxidation performance of ZrC in nuclear environments.

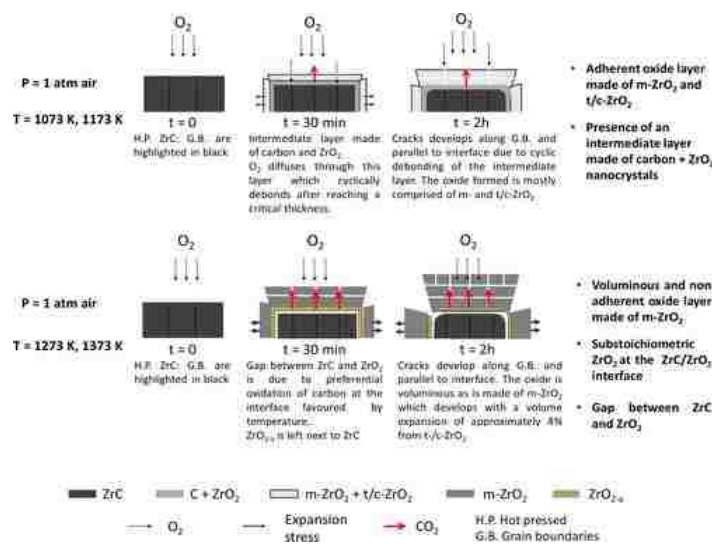


Figure 2.5. Stages of the oxidation of hot-pressed (H.P.) specimens of ZrC at 800 and 900 °C in atmospheric air. Taken from [68].

**2.4.4. Other Degradation Mechanisms.** There are other degradation mechanisms that are important for the implementation of  $\text{ZrC}_x$  in nuclear reactors such as the chemical interaction with fission products. This topic is beyond the scope of this thesis and will not be further elaborated. An extensive review on retention of fission products in ZrC-based fuels have been recently published by Katoh *et al.* [20].

## PAPER

### I. THE ION- IRRADIATION RESPONSE OF ZrC CERAMICS AT 800 °C

Raul Florez<sup>a</sup>, Miguel L. Crespillo<sup>b</sup>, Xiaoqing He<sup>c,d</sup>, Tommi A. White<sup>c,e</sup>, Gregory Hilmas<sup>f</sup>,  
William Fahrenholtz<sup>f</sup>, Joseph Graham<sup>a,f\*</sup>

- a. Nuclear Engineering Program, Missouri University of Science and Technology,  
65409 Rolla, MO, United States
- b. Department of Material Science and Engineering, University of Tennessee, 37996  
Knoxville, TN, United States
- c. Electron Microscopy Core, University of Missouri, 65211 Columbia, MO, United  
States
- d. Department of Mechanical and Aerospace Engineering, University of Missouri,  
65211 Columbia, MO, United States
- e. Department of Biochemistry, University of Missouri, Columbia, MO, 65211,  
United States
- f. Department of Materials Science and Engineering, Missouri University of Science  
and Technology, 65409 Rolla, MO, United States

## ABSTRACT

The microstructural evolution was characterized for ZrC ceramics irradiated with 10 MeV Au<sup>3+</sup> ions at 800 °C. Post-irradiation examination showed that ZrC did not amorphize at doses up to 30 displacement per atoms (dpa). Concurrent oxidation of ZrC was found to occur during ion irradiation. Coarsening of the defective microstructure, as a function of dose, was revealed by transmission electron microscopy analysis. Black dot

defects were observed at low doses (0.5 dpa), and tangled dislocation networks were formed at 5 dpa and above. Diffraction analysis showed a change in the defect structure occurred at doses close to ~2.5 dpa. The evolution of lattice parameter with dose indicated that uptake of adventitious oxygen could occur in specimens irradiated at high doses. Raman spectroscopy analysis indicated an increase in non-stoichiometry after irradiation. This work identified specific relationships between dose and microstructure after irradiation, revealing the mechanisms of damage production in  $\text{ZrC}_x$  ceramics.

**Keywords: Ion Irradiation,  $\text{ZrC}_x$ , XRD, TEM, Raman**

\* Corresponding author

Email: grahamjose@mst.edu

## 1. INTRODUCTION

Zirconium Carbide ( $\text{ZrC}_x$ ) is a ceramic material that exhibits high melting temperature and Vickers hardness [1], excellent high-temperature thermal and mechanical properties [2], adequate corrosion resistance to fission products [3], [4], and low neutron absorption cross section [1], [5]. This unusual combination of properties makes  $\text{ZrC}$  an attractive candidate for a variety of elevated-temperature nuclear applications, including fuel cladding and inert fuel matrix materials for Gen-IV gas-cooled reactors [6], [7], structural components in fusion reactors [8], and as a coating in Trisostructural-Isotropic (TRISO) fuel particles [9-12]. In these applications,  $\text{ZrC}_x$  would be exposed to neutron and ion irradiations [13],[14]. As a result, atomic defects, lattice

disorder, and other radiation-induced microstructural modifications are expected to occur due the substantial amount of energy deposited in the target material under irradiation. The formation and distribution of radiation-induced defects can significantly affect the mechanical, thermophysical, and chemical properties of  $\text{ZrC}_x$  after irradiation [15-17]. Consequently, successful implementation of  $\text{ZrC}_x$  in nuclear systems requires investigation of its radiation response mechanisms and the concomitant radiation effects on the properties.

During the last three decades, a great number of experimental [18-22] and theoretical investigations [23-26] have been dedicated to understanding the fundamental processes that govern the radiation response of  $\text{ZrC}_x$ . The majority of studies to date have focused on characterizing the radiation damage produced by nuclear elastic interactions (*i.e.* ballistic damage), which is most relevant to the operational performance of  $\text{ZrC}_x$  subject to neutron fluxes in nuclear reactors [27]. To this end, intermediate-energy heavy ions and protons from ion accelerator facilities have been widely used to emulate ballistic damage under well-controlled irradiation conditions and high displacement doses [28]. Ballistic collisions displace atoms from their equilibrium positions, initiating a series of structural changes within the target material, which are dependent on the rate of production, annihilation, and agglomeration of the radiation-induced point defects at a given temperature [29]. Using this approach, systematic studies have been conducted for ion irradiation of  $\text{ZrC}_x$  at multiple irradiation conditions over the temperature range of 20-1073 K [30-32]. The ion irradiated microstructures have been characterized with a number of techniques including transmission electron microscopy (TEM) , X-ray diffraction (XRD), ion channeling Rutherford backscattering spectrometry (RBS/c), and

Raman spectroscopy. No amorphization has been observed in any of the above studies, demonstrating the superior structural stability and radiation tolerance of  $\text{ZrC}_x$  over the temperature range investigated.

Previous studies suggested that within the operational temperature range of high temperature nuclear reactors (600-1100° C), the radiation response of  $\text{ZrC}_x$  is driven by interstitial clustering [33]. Due to the high melting point of  $\text{ZrC}$  ( $T_m=3420$  °C [34]), vacancy mobility is not expected when  $T_{irr}<0.3T_m$ . In contrast, interstitial atoms are highly mobile even at RT and immediately tend to cluster to form dislocation loops under far from equilibrium conditions [26]. These observations have been validated experimentally by TEM analysis, through which “black dot” defects and dislocation loops have been observed as the primary type of defects in irradiated  $\text{ZrC}_x$  [13], [31], [32], [35]. The clustering of interstitials in irradiated  $\text{ZrC}_x$  has also been reproduced numerically using DFT-informed Cluster Dynamic simulations [33]. In the low homologous temperature regime, where interstitials are mobile and vacancies are sessile, two competing processes occur simultaneously: dislocation loop nucleation and interstitial capture by dislocation loops. Initially at lower doses ( $\sim <1$  dpa), the rate of nucleation of interstitial clusters outpaces the rate of loop growth because the density of dislocation loops is low. When increasing the irradiation dose, new interstitial clusters are more likely to coalesce with each other to form dislocation loops. These loops will continue to grow in size and density until a critical dose is reached. At this point, the rate of dislocation loop nucleation is reduced because the defect clusters generated by irradiation are more likely to coalesce with the already nucleated dislocation loops. Consequently, irradiation beyond this threshold dose will produce coarsening of dislocation loops that are already

formed. As dislocation loops grow, each will become an increasingly larger sink for defects, so the nucleation rate of loops should continue to drop until saturation is reached. As a result, a saturation in the density of dislocations is also expected with the increase in the irradiation dose.

Although a coarse understanding of the radiation response of  $\text{ZrC}_x$  can be drawn from the existing literature, more studies are needed to complement the previously reported experimental data and provide a comprehensive understanding of the performance of  $\text{ZrC}_x$  within the typical temperature (600-1100° C) and dose range (0.5-50 dpa) of high temperature nuclear reactors (HTRs) [36]. In this regard, only a limited number of studies have been conducted on high-temperature ion irradiation of  $\text{ZrC}$  at high doses. Moreover, knowledge of the radiation response of  $\text{ZrC}_x$  ceramics at different length scales is still scarce. This information is particularly relevant for future fission Gen-IV reactors and fusion reactors which require materials to reliably operate at higher temperatures and/or radiation damage levels than those of existing commercial power reactors [37].

The purpose of the present study was to investigate the microstructural evolution of heavy ion irradiated  $\text{ZrC}_x$  at dose and temperature conditions relevant to the operation of high temperature nuclear reactors.

## 2. EXPERIMENTAL PROCEDURE AND METHODS

### 2.1. SAMPLE PREPARATION

ZrC billets were prepared by the hot pressing commercial ZrC powder (Alfa Aesar, Reactor Grade, USA), which had a reported purity of 99.5 wt%, (impurities (wt.%): Al 0.01, Hf <0.003, Ti 0.009, Cd 0.0002, Cr 0.0003, Mg 0.0006, Pb 0.002). The billets were hot pressed in a graphite die (diameter=25 mm) using cylindrical graphite spacers (thickness=10 mm). The inner walls of the die and the faces of the spacers were lined with a BN-sprayed graphitized foil to prevent a reaction between the powder compact and the graphite die. ZrC powder was loaded into the die and cold-compacted using a uniaxial press with an applied pressure of 4 MPa. The die was then placed into a resistively-heated graphite hot press (Model HP20-3060, Thermal Technology Inc., Santa Rosa, CA). Once loaded into the hot press, the chamber was evacuated and backfilled with argon three times. Billets were hot-pressed at 2200°C and 32 MPa for 2 hours to promote full densification. A heating rate of 20°C/min was used.

The density of the hot-pressed billets was measured by Archimedes' method using distilled water as the immersing medium, according to ASTM C73 [38]. The relative density was calculated by dividing the Archimedes' density by the estimated theoretical density of ZrC.

Following densification, specimens for microscopy and ion irradiations were cut parallel to the hot-pressing direction of the billet with a slow-speed diamond saw and then ground and polished to mirror-finish. The metallographic preparation was carried out by grinding the specimens with 100, 320, 600, and 1200 grit SiC pads and water



lubricant. Felt pads and water-based diamond slurry suspensions were used for abrasive sizes from 3  $\mu\text{m}$  to 0.025  $\mu\text{m}$ . After polishing, the specimens were ultrasonically cleaned with ethanol for 15 minutes at room temperature.

## 2.2. ION IRRADIATION

A rectangular ZrC polished section (13 x 8 mm) was irradiated in the Ion Beam Materials Laboratory (IBML UT-ORNL) at the University of Tennessee, Knoxville [39] with 10 MeV  $\text{Au}^{3+}$  ions at 800° C using a 3.0 MV tandem accelerator. Five different regions of the ZrC specimen (3x3 mm each) were irradiated to doses of 0.5, 2.5, 5, 10 and 15 dpa. The total sample area was thus comprised of the five non-overlapping irradiated regions and one unirradiated control region. An additional ZrC polished section was also irradiated to a dose of 30 dpa at the same temperature. Adjustable beam slits were used to define the irradiation areas. The ion beam was defocused and rastered in the horizontal and vertical directions with the aim of producing a region that was homogeneously irradiated. Beam homogeneity was verified by ion-induced luminescence from quartz targets and was found to be within 10% throughout the irradiated area [40]. The flux was set at  $1.0 \times 10^{12} \text{ cm}^{-2} \text{ s}^{-1}$  for all fluences. Low beam current densities in the range of 5 nA  $\text{mm}^{-2}$  were used to reduce any undesired effect and charge accumulation on the samples [41]. The vacuum chamber pressure was observed to be below  $5 \times 10^{-8}$  torr prior to the sample heating process. During sample heating, the chamber pressure initially rose before decreasing to a range of  $3\text{-}5 \times 10^{-7}$  torr during irradiation. The maximum outgassing of the specimen was observed around 170° C with vacuum pressure levels of  $7.8 \times 10^{-6}$  torr. The Stopping and Range of Ions in Matter binary collision approximation (BCA) code

2013 version (SRIM-2013) [42] was used to estimate the displacement damage depth profile. Cascades were performed in quick-cascade mode (simple Kinchin and Pease model), assuming a target density of  $6.71 \text{ g/cm}^3$  and threshold displacement energies of 37 eV for Zr and 16 eV for C. To compare ion and neutron irradiation results, the use of the quick Kinchin–Pease option in SRIM to compute radiation damage exposure has been recommended [43] within the nuclear community and has been widely used in previous studies of ion-irradiated ZrC [35], [18], [19]. The damage profile estimated from SRIM is determined by the sum of the predicted vacancy concentrations (using 'Knock-Ons' from Au ions and 'Vacancies' from target elements of Zr and C), together with the replacement collisions [44]. Assuming a bulk ZrC sample, the predicted damage profile in displacements per atom (dpa), and the implanted Au ion profile, are shown in Figure 1. The peak dose under 10 MeV Au irradiation is located around 1000 nm. The conversion factor from ion fluence ( $10^{14} \text{ cm}^{-2}$ ) to local dose in the ZrC foil under quick simulation was 0.8343 dpa. The steady state temperature of the sample surface was measured via a K-type (chromel-alumel) thermocouple (TC). The TC was attached to the sample surface by molybdenum spring-loaded clips. Samples mounted on the high temperature stage were conductively heated from the platen. The rear of the platen was radiatively heated using a resistively heated tungsten filament (ERH series heater and EPS-500 power supply, Thermionics Northwest, Inc.). High performance silver paste was used to improve the thermal contact between the bottom surface of the sample and the platen. More details on the experimental apparatus are provided elsewhere [39],[41]. Irradiations were performed with Au ions because of their relatively inert nature and large nuclear stopping cross section, which produces a high damage rate per incident ion and

minimizes artifacts induced by the injected ions. It is worth noting that a 10 MeV energy beam was chosen to obtain a relatively flat profile to a depth of 1  $\mu\text{m}$  without appreciable effects of implanted Au ions (Figure 1). Moreover, intermediate energy heavy ion irradiations produce a displacement cascade density and morphology more similar to fission neutrons than light ion irradiation, which produce a more space sub-scale morphology [45]. The temperature and range of doses were selected with the goal of studying radiation damage mechanisms and their effects on microstructural evolution and physical property changes in Gen-IV high temperature gas-cooled reactors [37] .

## 2.3. MATERIAL CHARACTERIZATION

In this section, the different experimental techniques and methods that were used for material characterization of the specimens are described.

**2.3.1. Grazing Incidence X-Ray Diffraction (GIXRD).** Grazing incidence X-ray diffraction measurements were performed to evaluate structural modifications in the near surface region following high temperature ion irradiations. GIXRD profiles were collected on a PANalytical X'Pert Pro Multipurpose Diffractometer (MPD) fitted with a Cu X-ray tube and an X'Celerator detector. Diffraction patterns were acquired in grazing incidence geometry over the  $2\theta$  range  $25-90^\circ$  with a step size of  $0.03^\circ$  and counting time of 0.5 s at each step. The scans were recorded at several incident angles between  $0.5^\circ$  and  $5^\circ$  in order to probe microstructural changes at different depths from 0.6 to 1.5  $\mu\text{m}$  (Figure 2). X-ray tube operation conditions were 40 kV and 40 mA. The lattice parameter was refined by Rietveld analysis in the full matching pattern mode with the Fullprof suite software [46].

**2.3.2. Line Profile Analysis.** The values for the size of coherent diffracting domains and microstrains were determined using Williamson-Hall analysis. Peaks obtained from only Cu  $k_{\alpha 1}$  radiation were analyzed after stripping Cu  $k_{\alpha 2}$  peaks using the classical Rachinger's method [47]. Instrumental broadening was described using a Caglioti polynomial expression obtained by line profile fitting of LaB<sub>6</sub> standard powder (SRM 660a) over the  $2\theta$  range investigated. The instrumental integral broadening, thus defined, was subsequently subtracted from the measured integral breadth of the samples to obtain the structural line broadening  $\beta$ .

The coherent diffracting domain sizes ( $D_v$ ) and microstrains ( $\varepsilon$ ) were obtained from the ordinate intercepts and the slopes, respectively, of straight lines in the Williamson–Hall plots, according to the following equation:

$$\beta \cos(\theta) = \frac{\lambda}{D_v} + 4\varepsilon \sin(\theta) \quad (1)$$

where  $\beta$  is structural line broadening of the reflection,  $2\theta$  is the peak position angle, and  $\lambda$  is the monochromatic x-ray wavelength.

## 2.4. ELECTRON MICROSCOPY

Surface morphology and composition were examined for both pristine and irradiated materials by focused ion beam (FIB)-scanning electron microscopy (FIB SEM, Scios<sup>TM</sup> DualBeam<sup>TM</sup>, FEI, Hillsboro, Oregon) coupled with energy dispersive spectroscopy (EDS; Oxford Instrument Avignon UK). TEM specimens were also prepared using the focused-ion-beam (FIB) lift-out technique. Before milling, a 2  $\mu\text{m}$  thick Pt layer was deposited on the top surface of the specimen to protect it from ion beam-induced damage and unwanted surface milling during the FIB preparation. The

trenching on both sides was performed at an ion beam voltage of 30 kV with a beam current of a few nanoamps. After lift-out, thinning of the lamella was first conducted with a beam current of hundreds of picoamps at 30 kV at  $\pm 5^\circ$  on both sides using cleaning cross-section mode until the lamella was  $\sim 1 \mu\text{m}$  thick. Voltages and currents were gradually reduced, and the milling angles decreased, as the lamella got thinner. To complete the preparation, gentle polishing with  $\text{Ga}^+$  ions (5 keV and 48 pA) at  $\pm 7^\circ$  in regular rectangular mode was used to reduce damage and artifacts of ion implantation caused by higher energy Ga bombardment. Microstructure characterization was performed using a 300 kV Tecnai F30 Supertwin transmission electron microscope (TEM). Bright field (BF) images were acquired under a  $g = \mathbf{220}$  two beam condition with the deviation vector  $s$  being slightly positive.

## 2.5. RAMAN SPECTROSCOPY

Raman measurements were collected using a HORIBA Jobin Yvon LabRAM ARAMIS microRaman spectrometer (Horiba, Edison, NJ). The specimens were excited by a 632 nm He/Ne laser focused to a spot 2-3  $\mu\text{m}$  in size on the sample using a 50x microscope objective lens. Raman spectra were acquired in the backscattering geometry. The laser power was below 2 mW to prevent local heating of the sample. Five spectra were taken from each specimen, with all measurements conducted at room temperature.

### 3. RESULTS AND DISCUSSION

#### 3.1. CONTROL SPECIMEN

The relative density of the as-sintered billet was approximately 93%. Figure 3a shows survey GIXRD patterns, obtained at  $\omega$  values of 0.5, 1, 1.5, 3 and 5°, from the unirradiated ZrC sample after annealing for 5h at 800°C in the ion beam line vacuum chamber. The XRD profiles show the expected FFC peaks for ZrC from the (111), (002), (022), (113), (222), and (004) planes corresponding to  $2\theta$  values of 32.98, 38.27, 55.26, 65.90, 69.23, and 82.03°, respectively. In addition, the patterns exhibited a low intensity peak at  $2\theta=30.11^\circ$ , that was attributed to the presence of ZrO<sub>2</sub>. This peak could not be indexed unequivocally because the monoclinic, tetragonal and cubic forms of ZrO<sub>2</sub> all have peaks close to  $2\theta=30^\circ$ ; making them undistinguishable from each other using just this single peak. However, the unirradiated ZrC specimens appear to contain some ZrO<sub>2</sub> in the near surface region, after annealing, that was not detected in the as-processed materials.

Figure 3b shows a magnified view of the most intense (111) ZrC diffraction peak. Increasing the incident angle (i.e., increasing the x-ray penetration depth into the specimen) led to increased peak intensity and a reduction of the peak breadth. Similar behavior was also observed for the other ZrC peaks. Concurrent reduction in peak breadth and increased peak intensity with increasing incident angle are indicative of heterogeneous microstrain near the surface [48]. The average microstrain values as a function of the incident angle were determined using Williamson-Hall analysis (Figure 4a). The unirradiated sample exhibited a microstrain of  $\epsilon=0.26 \pm 0.02\%$  at the lowest incidence angle ( $\omega=0.5^\circ$ ). The microstrain decreased at a larger penetration depth

probed using  $\omega=1, 1.5, 3$  and  $5^\circ$ , suggesting that the region of highest strain is localized within the first 20 nm of depth from the top surface. The main sources of microstrain could be the difference in the molar volume and thermal expansion coefficient between the major phase, ZrC, and the minor phase of ZrO<sub>2</sub> that was detected; although some residual microstrain could have been introduced during polishing steps used to prepare the surfaces that were irradiated.

The formation of the oxide phase near the surface of the annealed ZrC was confirmed by SEM observations (Figure 5). Annealing produced discrete nanosized nodules distributed across the surface of annealed specimen that were not present in the original polished surface. The nanoprecipitates ranged in sizes between 20 and 100 nm. Energy dispersive spectroscopy (EDS) analysis indicated that Zr, C and O were the major constituents on the top surface area of the annealed sample. This suggests that the nanoprecipitate nodules observed in the SEM images correspond to the nuclei of the oxide phase detected by GIXRD measurements. Some precipitate-free zones were observed near the grain boundaries of the substrate, which were also revealed due to thermal etching during annealing.

Further analysis of the (111) ZrC reflection (Figure 3b) revealed that the location of the diffraction maxima shifted to higher  $2\theta$  angles as  $\omega$  decreased. This suggests that the lattice parameter of ZrC was lower near the surface (Figure 4b), which could arise from dissolution of adventitious oxygen into the ZrC lattice during annealing. Oxygen uptake result, which is sometimes described as the formation of an oxycarbide (ZrC<sub>x</sub>O<sub>y</sub>) compound, does not change the structure of ZrC, but decreases the lattice parameter [49]. The contraction of the unit cell results from the strengthening of the metal-non-metal

bonds upon incorporation of oxygen into vacant sites in the unit cell [50]. This agrees with the previous work by Gendre, who showed the lattice size of ZrC decreased with oxygen content up to a stoichiometry of around  $\text{ZrC}_{0.79}\text{O}_{0.13}$  [51].

### 3.2. IRRADIATED SPECIMENS

Next, the results of the GIXD, TEM and Raman spectroscopy analyses for the ion-irradiated samples are presented.

**3.2.1. GIXRD and TEM Analysis.** Figure 6a shows representative GIXRD patterns of ZrC samples after irradiation with 10 MeV  $\text{Au}^{3+}$  at 800°C. The diffraction patterns were acquired at  $\omega=1.5^\circ$  to probe a suitable artifact-free midrange region of the implantation profile (see Figure 2). Similar to the control specimen, the main peaks indexed to ZrC, and low intensity  $\text{ZrO}_2$  peaks were observed at  $2\theta=30.11^\circ$  for the irradiated specimens. Upon irradiation, three major changes were observed in the XRD patterns: shifts of the diffraction maxima, peak broadening, and reduction in the intensities. No evidence of amorphization was observed in any of the samples irradiated at 800°C, confirming the outstanding stability of ZrC under irradiation. Similar results have been previously reported in neutron and ion irradiation experiments of ZrC at both room temperature and high temperature [30], [31], [32]. The most obvious effects of increasing the irradiation dose are a decrease in ZrC peak intensity and an increase in peak broadening. These changes occur due to the microstructural distortions and heterogeneous microstrain associated with the formation of radiation-induced defects. In this regard, the defects present in the irradiated materials distort the long range symmetry of the ideal rock-salt crystal structure, resulting in a partial loss of the coherent scattering



and the concomitant decrease in peak intensity. On the other hand, the increased peak broadening can also be ascribed to the accumulation of heterogeneous microstrain and/or the reduction of the coherent scattering domain size.

Williamson-Hall analysis was applied to irradiated samples. W-H plots for the irradiated samples are shown in Figure 7(a). With the exception of the specimen irradiated to 2.5 dpa (Figure 7b), no anisotropic peak broadening was observed along any specific crystallographic direction in the diffraction pattern of the irradiated samples. The strong peak broadening anisotropy at 2.5 dpa was accompanied by an increased diffuse scattering and a significant reduction of the peak intensity. These concurrent changes are indicative of an increased atomic disorder, which could be due to point defects and dislocation loops. The scattering of X rays from point defects and clusters contribute to diffuse scattering very close to the Bragg peak, which is known as Huang scattering [52]. This type of scattering can be evaluated to analyze the defects in the irradiated sample; however, the GIXRD measurements in this study were conducted at room temperature and the Huang scattering near the Bragg region is superimposed by thermal diffusion scattering, making its evaluation difficult. Since the W-H analysis for the sample irradiated to 2.5 dpa was confounded by these other effects, this specimen was not considered in the subsequent line-broadening analysis. The W-H plots indicated that grain size did not change significantly, but strain increased with increasing dose. This indicates that the XRD peak broadening is primarily due to strain, rather than a reduction in grain size. The average microstrain values for the irradiated samples obtained are shown in Figure 8(a). It is noted that the average microstrain increased with the irradiation dose and then saturated at doses above 5 dpa with  $\varepsilon_{sat} \sim 2.2 \times 10^{-3}$ .

Saturation of the dislocation density at high doses could explain the microstrain trend observed in this work. At low doses (0.5 dpa), the radiation-induced interstitial clusters have sizes in the order of a few nanometer ( $< 5$  nm) and their density is low. Therefore, the microstrain value observed at 0.5 dpa is also low ( $\sim 1.2 \times 10^{-3}$ ). Figure 9a shows an on-zone axis bright field TEM micrograph of the sample irradiated at 0.5 dpa. The image reveals the presence of “black dot” defects, which are likely to be small interstitial clusters formed by the ion irradiation. No dislocation loops, with or without double arc-contrast, are observed in the micrograph. Similar results have been obtained in previous TEM work of ion irradiated ZrC at low doses and high temperatures [30], [35]. On the other hand, at doses higher than 5 dpa, it can be hypothesized that ZrC has already reached the saturation point in the coarsening-dominant regime. In other words, the rate of dislocation loop nucleation has dropped to a steady state value, and therefore the radiation-induced dislocation structure does not undergo further coarsening. This hypothesis is consistent with the previous in-situ TEM study by Ulmer *et al.* [35], which noted that the microstructure of ZrC, irradiated with 1MeV Kr ions at 800°C, continued to coarsen until doses of 5.1–7.7 dpa. Beyond this dose, a tangled dislocation network formed, and little change was observed in the irradiated microstructure. In this work, “cellular-like” dislocation networks were also observed in bright-field (BF) images of the irradiated microstructure at doses above 5 dpa (Figure 9b and c). This suggests that at high doses ( $>5$  dpa), a balance was reached between irradiation-induced damage buildup and dynamic annealing of defects at 800°C.

Figure 8b shows the evolution of the ZrC lattice parameter as a function of the dose obtained by refinement of the peak shifts in the XRD patterns. Interestingly, the

evolution of the unit cell parameter in this study is not consistent with a single impact mechanism for damage accumulation. This result differs from previous observations by Gosset *et al.* [53], who reported a saturation of the cell parameter evolution for ZrC irradiated with 4 MeV Au ions at room temperature. In the present study, the unit cell parameter of ZrC exhibited a complex, non-monotonic behavior as a function of dose. Initially, the unit cell parameter increased until reaching a dose of 2.5 dpa. Then, above this critical dose, the lattice parameter decreased. The recovery of the unit cell parameter is consistent with a two-step damage accumulation process, which has been previously observed in single crystal ZrC and other non-amorphizable ceramics under irradiation in the nuclear energy loss regime [54], [55]. According to this mechanism, a build-up of elastic strain is observed at the early stages of the damage process due to the production and clustering of Frenkel Pair (FP) defects. The accumulation of FPs leads rapidly to the formation of dislocation loops that continue to grow in size as the dose level is increased. Eventually, at the threshold dose, the dislocation loops come into contact with each other and form an entangled dislocation network. This transformation in the defect structure is accompanied by an elastic strain relaxation due to the plastic deformation associated with the production of extended defects. According to Pellegrino *et al* [33], the critical fluence for this transition is about  $5 \times 10^{18}$  ions/m<sup>2</sup> (~2.2 dpa) for Au ions in ZrC. This value is close to the transition dose for unit cell parameter recovery that is observed in this work. However, another explanation will be required to account for the reduction of the unit lattice parameter at higher doses, where the structure of the dislocation network is no longer coarsening.

One possible explanation for the decrease of the lattice parameter at high doses could be the uptake of adventitious oxygen during the irradiation process. As mentioned above, the incorporation of oxygen into the crystalline structure of ZrC is accompanied by a contraction of the unit cell parameter. Zirconium carbide is well known for its high chemical sensitivity to oxygen impurities. Although the ion irradiations in this study were conducted in high vacuum conditions ( $<10^{-6}$  Pa), some residual oxygen and other hydrocarbon impurities are present in the irradiation chamber [56]. These impurities could oxidize target materials that are oxygen-sensitive during ion irradiation studies. ZrC has been reported to be subject to radiation-enhanced or radiation-induced oxidation at room temperature, even under vacuum (on the order of  $10^{-6}$  Pa) [53]. Oxygen enrichment has also been observed in ZrC implanted with argon and xenon ions [57], [58]. In the present work, the formation of  $\text{ZrO}_2$  phases in the irradiated samples was supported by GIXRD measurements at low incident angles. Based on these findings, it is possible that the diffusion of oxygen atoms may be enhanced during the high temperature irradiation of ZrC. Radiation enhanced diffusion (RED) is assisted by a linear superposition of different possible diffusion paths, such as monovacancies, divacancies, and dislocation lines, among others. These diffusion pathways can facilitate the ingress of oxygen atoms into the implantation layer, producing an oxycarbide compound that is isostructural with ZrC. Gosset *et al.* [18] investigated the influence of oxygen content on the radiation response of ZrC. They found that ZrC and  $\text{ZrO}_x\text{C}_y$  compounds follow the same type of microstructural evolution under radiation conditions, with oxycarbides showing a delay in the saturation fluence with respect to carbides. At high doses, such as those used in this study, entangled dislocation networks and vacancies may favor the

dissolution of oxygen into ZrC. However, the exact mechanism of oxygen uptake under irradiation conditions remains to be elucidated in future work.

**3.2.2. Raman Spectroscopy.** Figure 10 shows the Raman spectra of the control and irradiated samples. The spectra exhibit four predominant Raman bands centered around 200, 275, 515, and 600  $\text{cm}^{-1}$ . These spectra are very similar to those obtained in single crystals of ZrC with sub-stoichiometric compositions [59], [60]. The first-order Raman spectrum in  $\text{ZrC}_{1-x}$  has been attributed to the presence of carbon vacancies that destroy the local inversion symmetry of the ideal NaCl rock-salt structure, enabling defect-induced Raman scattering to be observed. The vacancy-induced first-order Raman spectrum resembles the phonon density of states (DOS) in ZrC. The low frequency Raman peaks (transverse acoustic  $\sim 204 \text{ cm}^{-1}$  and longitudinal  $\sim 275 \text{ cm}^{-1}$ ) are produced by acoustic phonons, while the high frequency peaks (transverse optic  $\sim 515 \text{ cm}^{-1}$  and longitudinal optic  $\sim 600 \text{ cm}^{-1}$ ) are due to optical phonons.

A comparison of the unirradiated and as-irradiated spectra shows that the Raman peaks associated with vacancy defects became more intense and broader when increasing the radiation dose. Similar radiation-induced changes have been previously observed in Raman studies of ion irradiated ZrC [60],[61]. These variations of the peak properties have been ascribed to the increasing number of carbon vacancies generated by irradiation. Heavy ion irradiation of ZrC results in the formation of point defects that distort the local structure of the material causing the appearance of the defect-induced Raman scattering as described above. Previous *ab initio* calculations have shown that carbon-related defects ( $V_c$  and  $C_i$ s) have lower defect formation energy than other types of point defects in  $\text{ZrC}_x$  [62], [23]. Consequently, extended non-stoichiometric regions

with a high concentration of carbon vacancies are expected to occur under irradiation conditions. For this reason, it is not surprising that a direct correlation exists between the irradiation dose and the concentration of carbon vacancies, as indicated qualitatively by the changes in the Raman spectra for the irradiated samples. Besides these variations in vacancy-induced Raman bands, no new peaks are observed in the Raman spectrum of the irradiated samples. The similarity between the spectra for the irradiated and unirradiated specimens is indicative of the high microstructural stability of  $\text{ZrC}_x$  under irradiation conditions. This result is consistent with numerous computational and experimental studies which have shown the excellent radiation amorphization resistance of  $\text{ZrC}_x$ , [1], [13], [18], [24], [26], [33], [35], [53].

#### 4. CONCLUSIONS

The microstructural evolution was examined for  $\text{ZrC}_x$  irradiated with 10 MeV  $\text{Au}^{3+}$  ions at 800°C. No amorphization was observed in any of the irradiated samples, confirming the superior radiation stability of  $\text{ZrC}$ . Oxidation of the near surface area of the control and irradiated specimens was detected by GIXRD. Nanosized, discrete  $\text{ZrO}_2$  nodules were observed to grow over the surface. BFTEM micrographs revealed that “black dot” defects were formed after irradiation to ~0.5 dpa. A further dose increase to 5 dpa produced coarsening of the microstructure and formation of tangled dislocation networks. Beyond this dose, little change was observed in the irradiated microstructure, which suggested that a balance had been reached between irradiation damage buildup and dynamic annealing of defects. The dose dependence of the lattice parameter, and

microstrain, indicated that the defect structure changed at doses close to  $\sim 2.5$  dpa. This change could be ascribed to the coalescence of dislocation loops to form tangled dislocation networks. Additionally, the evolution of the unit cell also showed that oxygen uptake could occur in samples irradiated to high doses. The oxygen uptake at high doses might be assisted by radiation-enhanced diffusion processes and by the changing microstructure (i.e. pipe diffusion at high doses). Finally, Raman spectroscopy analysis showed an increase in  $\text{ZrC}_x$  non-stoichiometry after irradiation. This is due to an increase in carbon vacancies produced by the irradiation.

The coupling of synergistic techniques used in this study provided a more comprehensive view of the irradiation response of  $\text{ZrC}_x$  ceramics in the operational range of high temperature gas-cooled nuclear reactors. This work identified specific relationships between dose and microstructure after irradiation, revealing the mechanisms of damage production in  $\text{ZrC}_x$ , i.e., black-spot nucleation, as well as formation and evolution of dislocation loops. The results indicated that  $\text{ZrC}_x$  is a promising candidate for high temperature nuclear applications, although precautions must be taken to prevent its oxidation during reactor operation.

## **ACKNOWLEDGEMENTS**

This research was supported by a Nuclear Regulatory Commission Faculty Development Grant NRC-HQ-84-15-G-0044 and by the Ceramics program of the U.S. National Science Foundation as part of project DMR 1742086. The microscopy work was

conducted at the Electron Microscopy Center (EMC) of the University of Missouri Columbia with partial funding through the EMC Excellence Microscopy Award.

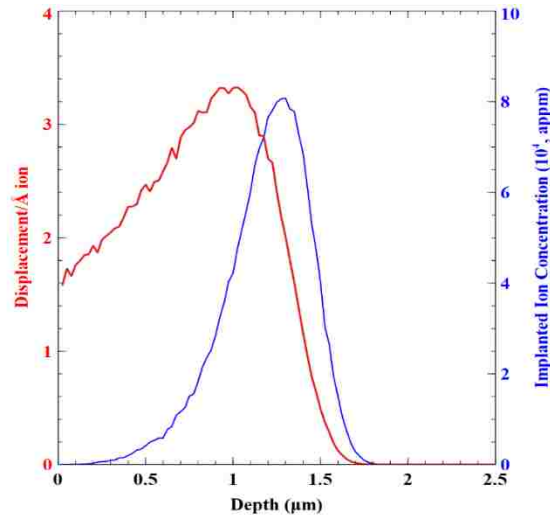


Figure 1. Depth profile of damage level using SRIM Kinchin and Pease calculations, and Au concentration as a function of depth for a fluence of  $3.59 \times 10^{15} \text{ cm}^{-2}$ .

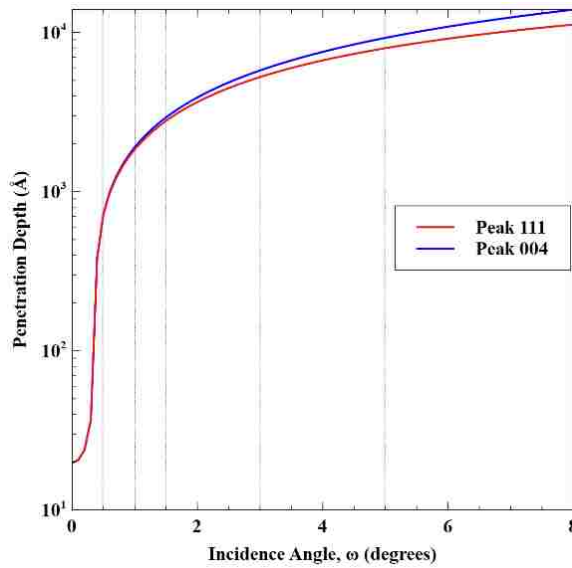


Figure 2. The scattering depth,  $\Lambda$ , from which diffraction data was collected as a function of the x-ray incident angle for two diffraction peaks, (111) and (400). The x-ray incident angles used in this work are denoted by vertical dashed lines.



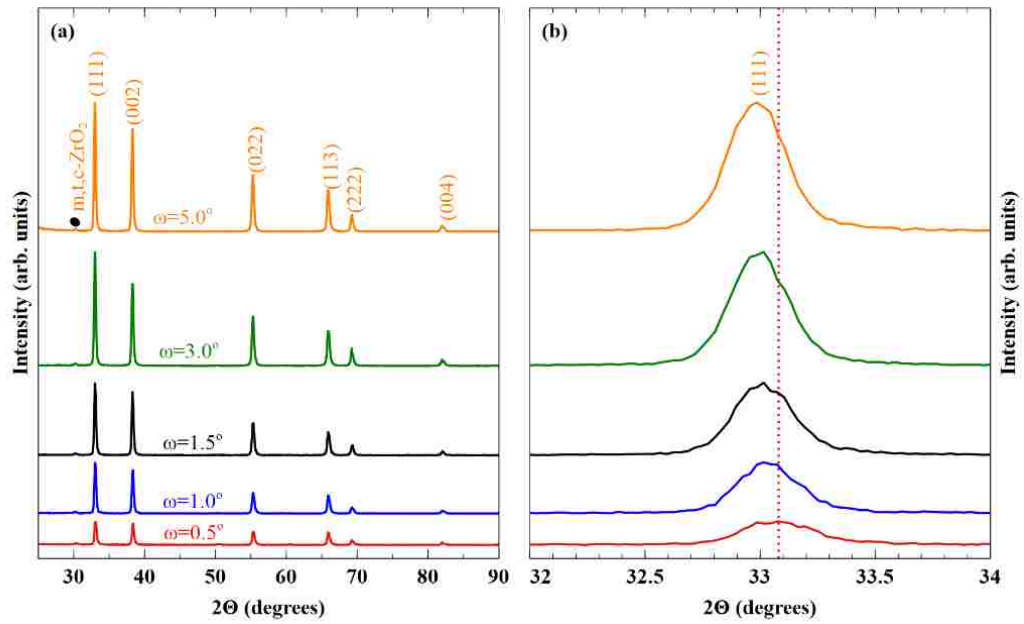


Figure 3. (a) GIXRD obtained from ZrC after thermal annealing in the ion irradiation chamber at 800 °C, collected at various x-ray incident angles. (b) An enlarged view of the most intense (111) ZrC diffraction maxima.

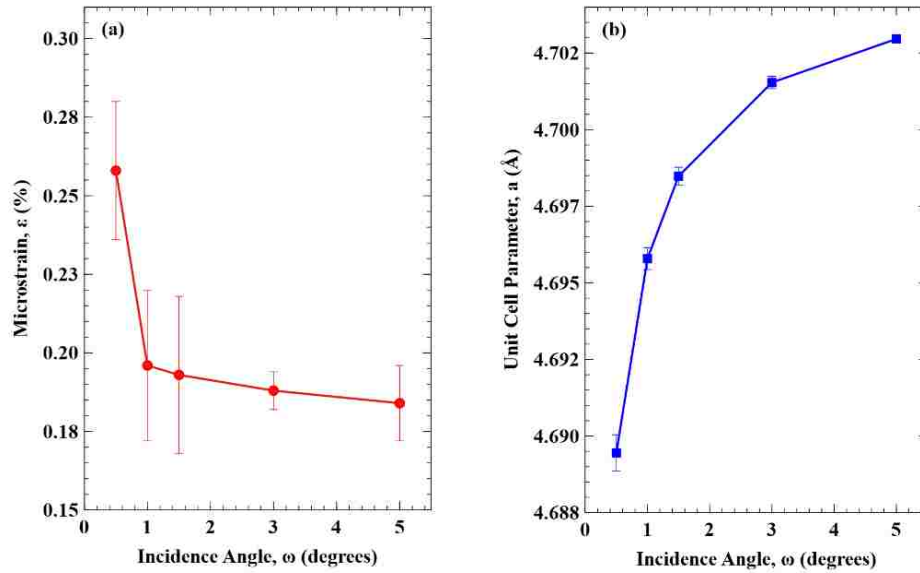


Figure 4. (a) Heterogeneous microstrain of control sample determined using Williamson–Hall plots as a function of the X-ray incident angle. (b) Unit cell parameter of ZrC for the control specimen as a function X-ray incident angle.

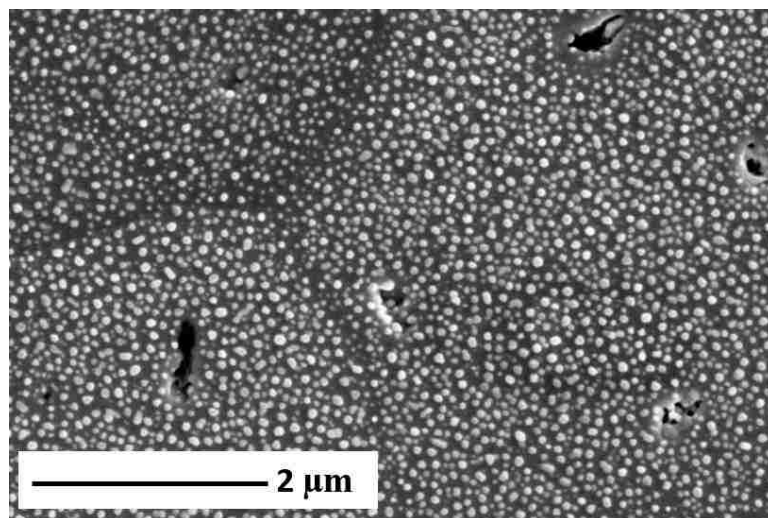


Figure 5. A secondary electron SEM image of the surface topography showing  $\text{ZrO}_2$  nanometric nodules.

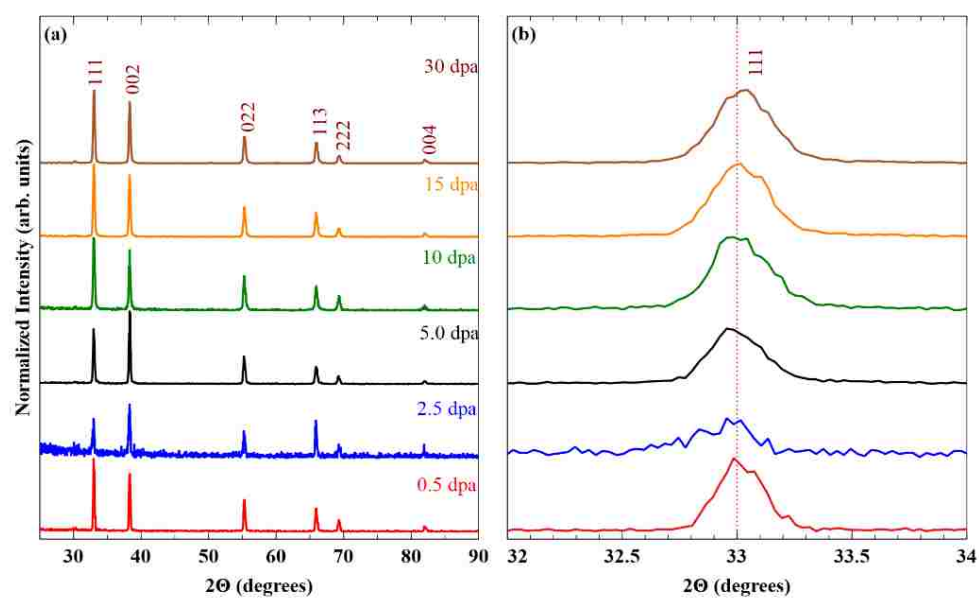


Figure 6. GIXRD patterns of ZrC after irradiation with 10 MeV  $\text{Au}^{3+}$  ions to different doses showing (a) the entire pattern and (b) an enlarged view of the (111) diffraction peak.

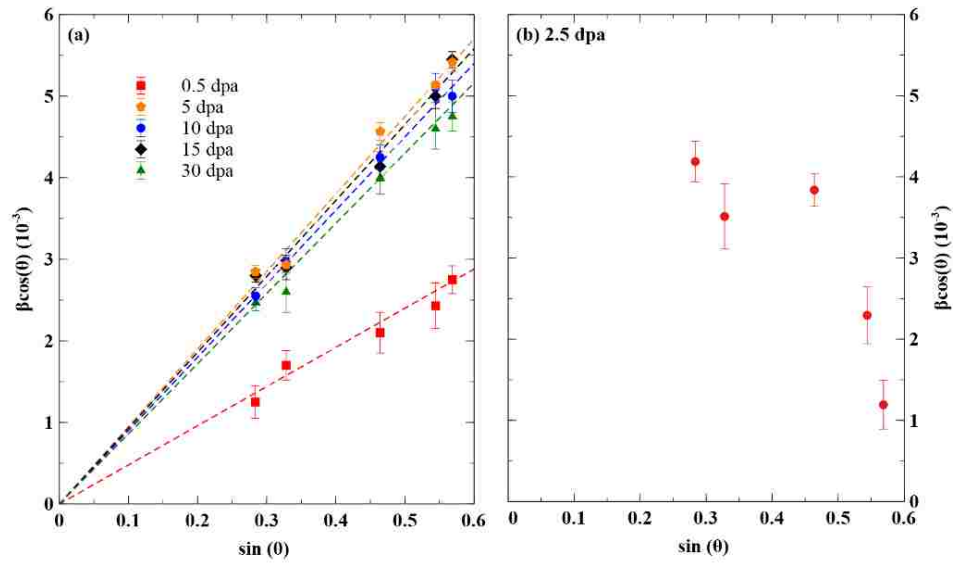


Figure 7. (a) Williamson-Hall plots of the representative XRD data from irradiated ZrC. Straight lines correspond to the linear fit to the peaks for each dose. The slopes are proportional to the amount of heterogeneous strain present, while their y-intercepts are inversely proportional to the average grain size, (b) Williamson-Hall plot of the specimen irradiated to 2.5 dpa.

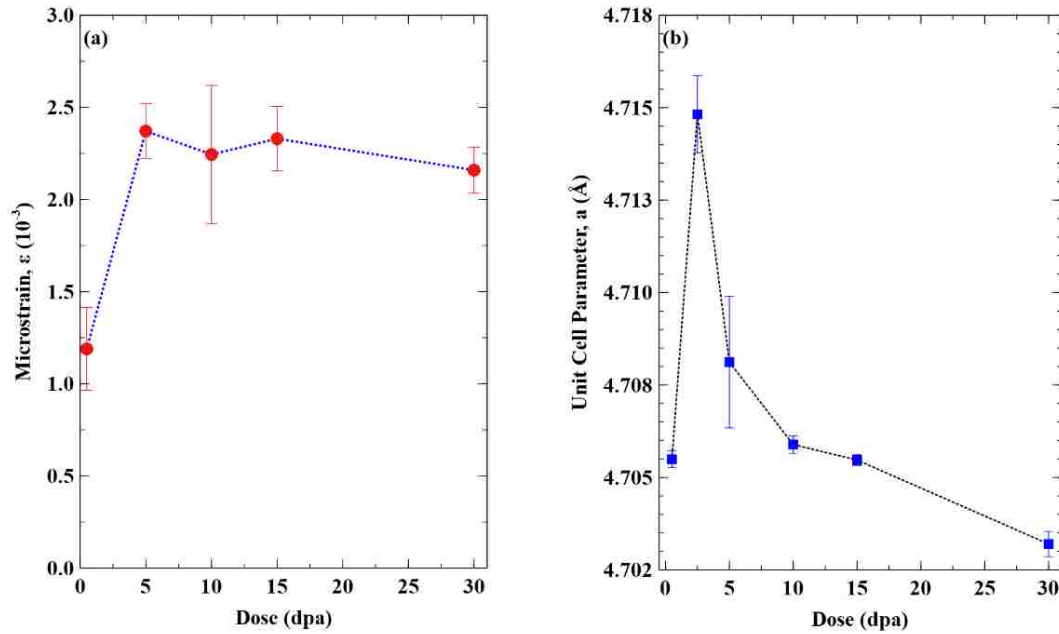


Figure 8. (a) Heterogeneous microstrain determined using Williamson-Hall plots as a function of dose, (b) Changes in the unit cell parameter of ZrC as a function of dose based on the refinement of the corresponding XRD patterns.

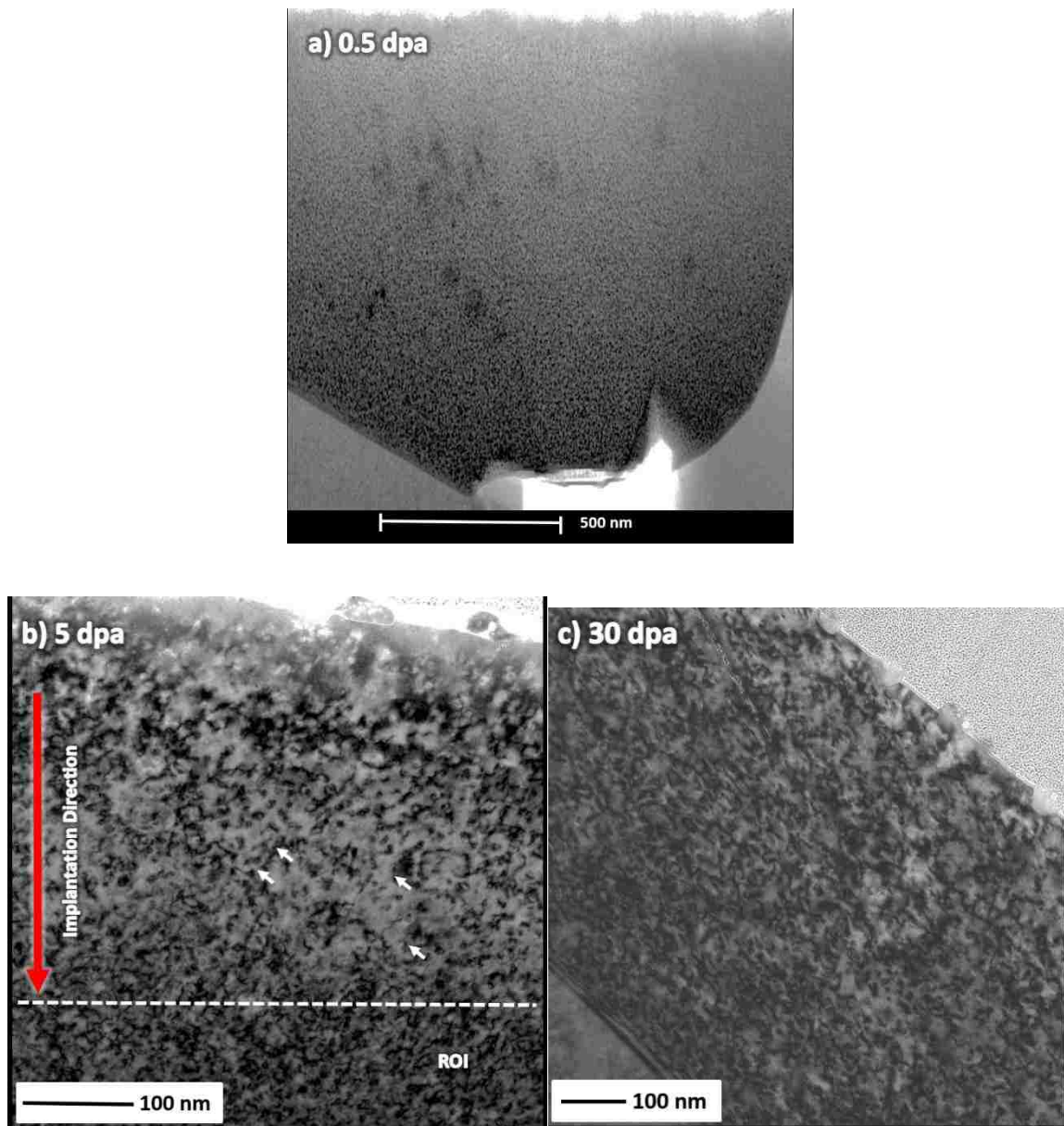


Figure 9. (a) On-Zone STEM Bright Field Image of the specimen irradiated to 0.5 dpa showing black dot defects, (b) Bright Field Image of the specimen irradiated to 5 dpa showing the tangle dislocation network. Some dislocation loops with boudle arc contrast are indicated by white arrows, (c) Bright Field Image of the specimen irradiated to 30 dpa showing the tangle dislocation network.

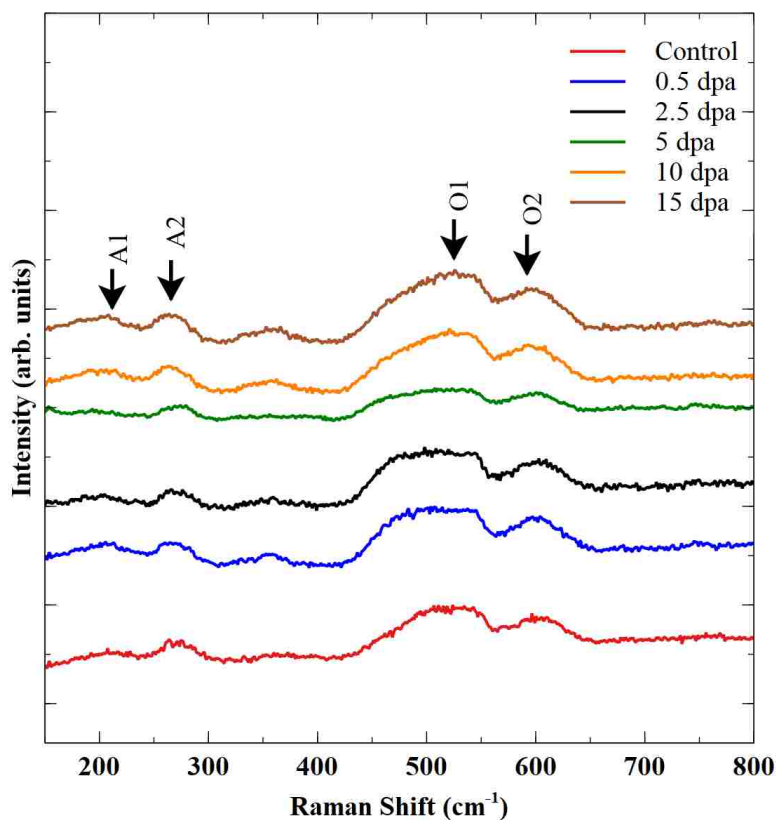


Figure 10. Raman spectra for ZrC irradiated at various doses.

## REFERENCES

- [1] H. F. Jackson and W. E. Lee, "Properties and characteristics of zrc," in *Comprehensive Nuclear Materials*, 2012.
- [2] M. M. Opeka, I. G. Talmy, E. J. Wuchina, J. A. Zaykoski, and S. J. Causey, "Mechanical, Thermal, and Oxidation Properties of Refractory Hafnium and zirconium Compounds," *J. Eur. Ceram. Soc.*, vol. 19, no. 13–14, pp. 2405–2414, 1999.
- [3] T. Ogawa and K. Ikawa, "Reaction of Pd with SiC and ZrC," *High Temp. Sci.*, 1986.
- [4] Y.-K. Yang and T. R. Allen, "The measurement of silver diffusivity in zirconium carbide to study the release behavior of 110mAg in the ZrC TRISO-coated nuclear fuel particle," *J. Nucl. Mater.*, vol. 470, pp. 76–83, 2016.

- [5] Y. Katoh, G. Vasudevamurthy, T. Nozawa, and L. L. Snead, "Properties of zirconium carbide for nuclear fuel applications," *J. Nucl. Mater.*, vol. 441, no. 1–3, pp. 718–742, 2013.
- [6] G. Vasudevamurthy, T. W. Knight, E. Roberts, and T. M. Adams, "Laboratory production of zirconium carbide compacts for use in inert matrix fuels," *J. Nucl. Mater.*, vol. 374, no. 1-2, pp. 241–247, 2008.
- [8] X.D. Yang, Z.M. Xie, S. Miao, R. Liu, W.B. Jiang, T. Zhang, X.P. Wang, Q.F. Fang, C.S. Liu, G.N. Luo, and X. Liu, "Tungsten-zirconium carbide-rhenium alloys with extraordinary thermal stability," *Fusion Eng. Des.*, vol. 173, no. 2, pp. 200–209, 2016.
- [9] K. Minato, T. Ogawa, K. Sawa, A. Ishikawa, T. Tomita, S. Iida, and H. Sekino, "Irradiation Experiment on ZrC-Coated Fuel Particles for High-Temperature Gas-Cooled Reactors," *Nucl. Technol.*, vol. 130, no. 3, pp. 272–281, 2000.
- [10] K. Minato and T. Ogawa, "Advanced concepts in triso fuel," R.J.M. Konings (Ed.), *Compr. Nucl. Mater.*, Elsevier, Oxford (2012), pp. 215-236.
- [11] I. E. Porter, T. W. Knight, M. C. Dulude, E. Roberts, and J. Hobbs, "Design and fabrication of an advanced TRISO fuel with ZrC coating," *Nucl. Eng. Des.*, vol. 259, pp. 180–186, 2013.
- [12] G. Vasudemurthy, Y. Katoh, J. D. Hunn, and L. L. Snead, "Pre- and Post-Irradiation Characterization and Properties Measurements of ZrC-coated Surrogate TRISO Particles," *Current*, 2010.
- [13] L. L. Snead, Y. Katoh, and S. Kondo, "Effects of fast neutron irradiation on zirconium carbide," *J. Nucl. Mater.*, vol. 399, no. 2–3, pp. 200–207, 2010.
- [14] G. Vasudevamurthy, Y. Katoh, J. Aihara, K. Sawa, and L. L. Snead, "Microstructure and mechanical properties of heat-treated and neutron irradiated TRISO-ZrC coatings," *J. Nucl. Mater.*, vol. 464, pp. 245–255, 2015.
- [15] D. Craciun, G. Socol, D. Simeone, S. Behdad, B. Boesl, B.S. Vasile, and V. Craciun, "Structural and mechanical properties changes induced in nanocrystalline ZrC thin films by Ar ion irradiation," *J. Nucl. Mater.*, vol. 468, pp. 78–83, 2016.
- [16] S. Gomès, L. David, J.-P. Roger, G. Carlot, D. Fournier, C. Valot, and M. Raynaud, "Thermal conductivity degradation induced by heavy ion irradiation at room temperature in ceramic materials," *Eur. Phys. J. Spec. Top.*, vol. 153, no. 1, pp. 87–90, 2008.

- [17] C. Jensen, M. Chirtoc, N. Horny, J. S. Antoniow, H. Pron, and H. Ban, “Thermal conductivity profile determination in proton-irradiated ZrC by spatial and frequency scanning thermal wave methods,” *J. Appl. Phys.*, vol. 114, no. 13, p. 133509, 2013.
- [18] D. Gosset, M. Dollé, D. Simeone, G. Baldinozzi, and L. Thomé, “Structural behaviour of nearly stoichiometric ZrC under ion irradiation,” *Nucl. Instruments Methods Phys. Res. Sect. B Beam Interact. with Mater. Atoms*, vol. 266, no. 12-13, pp. 2801–2805, 2008.
- [19] Y. Huang, B. R. Maier, and T. R. Allen, “Irradiation-induced effects of proton irradiation on zirconium carbides with different stoichiometries,” *Nucl. Eng. Des.*, vol. 277, pp. 55–63, 2014.
- [20] S. Pellegrino, L. Thomé, A. Debelle, S. Miro, and P. Trocellier, “Damage production in carbide single crystals irradiated with MeV heavy ions,” *Nucl. Instruments Methods Phys. Res. Sect. B Beam Interact. with Mater. Atoms*, vol. 307, pp. 294-298, 2013.
- [21] S. Agarwal, A. Bhattacharya, P. Trocellier, and S. J. Zinkle, “Helium induced microstructure damage, nano-scale grain formation and helium retention behaviour of ZrC,” *Acta Mater.*, vol. 163, pp. 14–27, 2019.
- [22] B. Wei, Y. Wang, H. Zhang, D. Wang, S. Peng, and Y. Zhou, “Microstructure evolution of nonstoichiometric ZrC<sub>0.6</sub> with ordered carbon vacancies under ion irradiation,” *Mater. Lett.*, vol. 228, pp. 254–257, 2018.
- [23] S. Kim, I. Szlufarska, and D. Morgan, “Ab initio study of point defect structures and energetics in ZrC,” *J. Appl. Phys.*, vol. 107, no. 5, p. 053521, 2010.
- [24] M.-J. Zheng, I. Szlufarska, and D. Morgan, “Defect kinetics and resistance to amorphization in zirconium carbide,” *J. Nucl. Mater.*, vol. 457, pp. 343–351, 2015.
- [25] M. Jiang, J. W. Zheng, H. Y. Xiao, Z. J. Liu, and X. T. Zu, “A comparative study of the mechanical and thermal properties of defective ZrC, TiC and SiC,” *Sci. Rep.*, vol. 7, no. 1, p. 9344, 2017.
- [26] L. Van Brutzel and J. P. Crocombette, “Classical molecular dynamics study of primary damage created by collision cascade in a ZrC matrix,” *Nucl. Instruments Methods Phys. Res. Sect. B Beam Interact. with Mater. Atoms*, vol. 255, no. 1, pp. 141-145, 2007.
- [27] G. S. Was, *Fundamentals of Radiation Materials Science*. New York, NY: Springer New York, 2017.



- [28] G. S. Was and R. S. Averback, "Radiation damage using ion beams," Konings (Ed.), *Compr. Nucl. Mater.*, Elsevier, Oxford (2012), pp. 195-221.
- [29] G. S. Was, "The Radiation Damage Event," in *Fundamentals of Radiation Materials Science*, New York, NY: Springer New York, 2017, pp. 3–76.
- [30] J. Gan, Y. Yang, C. Dickson, and T. Allen, "Proton irradiation study of GFR candidate ceramics," *J. Nucl. Mater.*, vol. 389, no. 2, pp. 317-325, 2009.
- [31] C. J. Ulmer, A. T. Motta, and M. A. Kirk, "In situ ion irradiation of zirconium carbide," *J. Nucl. Mater.*, vol. 466, pp. 606–614, 2015.
- [32] J. Gan, M. Meyer, R. Birtcher, and T. Allen, "Microstructure Evolution in ZrC Irradiated with Kr ions," *J. ASTM Int.*, vol. 3, no. 4, p. 12376, 2006.
- [33] S. Pellegrino, J. P. Crocombette, A. Debelle, T. Jourdan, P. Trocellier, and L. Thomé, "Multi-scale simulation of the experimental response of ion-irradiated zirconium carbide: Role of interstitial clustering," *Acta Mater.*, vol. 102, pp. 79–87, 2016.
- [34] R. V. Sara, "The System Zirconium-Carbon," *J. Am. Ceram. Soc.*, vol. 48, no. 5, pp. 243–247, 1965.
- [35] C. J. Ulmer, A. T. Motta, and M. A. Kirk, "In situ ion irradiation of zirconium carbide," *J. Nucl. Mater.*, vol. 466, pp. 606–614, 2015.
- [36] S. J. Zinkle and J. T. Busby, "Structural materials for fission and fusion energy," *Mater. Today*, vol. 12, no. 11, pp. 12–19, 2009.
- [37] S. J. Zinkle and G. S. Was, "Materials challenges in nuclear energy," *Acta Mater.*, vol. 61, no. 3, pp. 735–758, 2013.
- [38] ASTM, "ASTM C373-14 Standard Test Method for Water Absorption, Bulk Density, Apparent Porosity, and Apparent Specific Gravity of Fired Whiteware Products," *Astm C373-88*, 1999.
- [39] Y. Zhang, M.L. Crespillo, H. Xue, K. Jin, C.H. Chen, C.L. Fontana, J.T. Graham, and W.J. Weber, "New ion beam materials laboratory for materials modification and irradiation effects research," *Nucl. Instruments Methods Phys. Res. Sect. B Beam Interact. with Mater. Atoms*, vol. 338, pp. 19-30, 2014.
- [40] M. L. Crespillo, J. T. Graham, Y. Zhang, and W. J. Weber, "In-situ luminescence monitoring of ion-induced damage evolution in SiO<sub>2</sub> and Al<sub>2</sub>O<sub>3</sub>," *J. Lumin.*, vol. 172, pp. 208-218, 2016.



- [41] M. L. Crespillo, J. T. Graham, Y. Zhang, and W. J. Weber, "Temperature measurements during high flux ion beam irradiations," *Rev. Sci. Instrum.*, vol. 87, no. 2, p. 024902, Feb. 2016.
- [42] J. F. Ziegler, M. D. Ziegler, and J. P. Biersack, "SRIM - The stopping and range of ions in matter (2010)," *Nucl. Instruments Methods Phys. Res. Sect. B Beam Interact. with Mater. Atoms*, 2010.
- [43] R. E. Stoller, M. B. Toloczko, G. S. Was, A. G. Certain, S. Dwaraknath, and F. A. Garner, "On the use of SRIM for computing radiation damage exposure," *Nucl. Instruments Methods Phys. Res. Sect. B Beam Interact. with Mater. Atoms*, vol. 310, pp. 75–80, 2013.
- [44] Y. Zhang *et al.*, "Thermal stability and irradiation response of nanocrystalline CoCrCuFeNi high-entropy alloy," *Nanotechnology*, 2019.
- [45] G. S. Was, *Fundamentals of radiation materials science: Metals and alloys, second edition*. 2016.
- [46] FullProf Team, "FullProf Suite," *FullProf Suite*, 2006.
- [47] W. A. Rachinger, "A Correction for the  $\alpha_1$  and  $\alpha_2$  Doublet in the Measurement of Widths of X-ray Diffraction Lines," *J. Sci. Instrum.*, vol. 25, no. 7, pp. 254–255, 1948
- [48] A. R. Stokes and A. J. C. Wilson, "The diffraction of X rays by distorted crystal aggregates - I," *Proc. Phys. Soc.*, vol. 56, no. 3, pp. 174–181, 1944.
- [49] F. Réjasse, O. Rapaud, G. Trolliard, O. Masson, and A. Maître, "Experimental investigation and thermodynamic evaluation of the C–Hf–O ternary system," *J. Am. Ceram. Soc.*, vol. 100, no. 8, pp. 3757–3770, 2017.
- [50] P. Barnier and F. Thévenot, "Synthesis and hot-pressing of single-phase  $\text{ZrC}_x\text{O}_y$  and two-phase  $\text{ZrC}_x\text{O}_y\text{-ZrO}_2$  materials," *Int. J. High Technol. Ceram.*, vol. 2, no. 4, pp. 291–307, 1986.
- [51] M. Gendre, A. Maître, and G. Trolliard, "Synthesis of zirconium oxycarbide ( $\text{ZrC}_x\text{O}_y$ ) powders: Influence of stoichiometry on densification kinetics during spark plasma sintering and on mechanical properties," *J. Eur. Ceram. Soc.*, vol. 31, no. 13, pp. 2377–2385, 2011.
- [52] B. C. Larson, "X-ray diffuse scattering near Bragg reflections for the study of clustered defects in crystalline materials," in *Diffuse Scattering and the Fundamental Properties of Materials*, 2009.

- [53] D. Gosset, M. Dollé, D. Simeone, G. Baldinozzi, and L. Thomé, “Structural evolution of zirconium carbide under ion irradiation,” *J. Nucl. Mater.*, vol. 373, no. 1–3, pp. 123–129, 2008.
- [54] A. Debelle *et al.*, “Lattice strain in irradiated materials unveils a prevalent defect evolution mechanism,” *Phys. Rev. Mater.*, vol. 2, no. 1, p. 013604, 2018.
- [55] S. Moll *et al.*, “Damage processes in MgO irradiated with medium-energy heavy ions,” *Acta Mater.*, vol. 88, pp. 2015, 2015.
- [56] J. Wang *et al.*, “Carbon Contamination During Ion Irradiation - Accurate Detection and Characterization of its Effect on Microstructure of Ferritic/Martensitic Steels,” *Sci. Rep.*, vol. 7, no. 1, p. 15813, 2017.
- [57] G. Gutierrez *et al.*, “High temperature annealing of Xe implanted ZrC<sub>0.95</sub>O<sub>0.05</sub> investigated by RBS, TEM and PAS-DBS,” *Prog. Nucl. Energy*, vol. 57, pp. 57–61, 2012.
- [58] C. Martin, K. H. Miller, H. Makino, D. Craciun, D. Simeone, and V. Craciun, “Optical properties of Ar ions irradiated nanocrystalline ZrC and ZrN thin films,” *J. Nucl. Mater.*, vol. 488, pp. 16–21, 2017.
- [59] H. Wipf, M. V. Klein, and W. S. Williams, “Vacancy-Induced and Two-Phonon Raman Scattering in ZrCx, NbCx, HfCx, and TaCx,” *Phys. status solidi*, vol. 108, no. 2, pp. 489–500, 1981.
- [60] S. Pellegrino, L. Thomé, A. Debelle, S. Miro, and P. Trocellier, “Radiation effects in carbides: TiC and ZrC versus SiC,” *Nucl. Instruments Methods Phys. Res. Sect. B Beam Interact. with Mater. Atoms*, vol. 327, no. 1, pp. 103–107, 2014.
- [61] W. Bao, J. Liu, X. Wang, H. Zhang, J. Xue, S. Sun, F. Xu, J. Xue, and G. Zhang, “Structural evolution in ZrC-SiC composite irradiated by 4 MeV Au ions,” *Nucl. Instruments Methods Phys. Res. Sect. B Beam Interact. with Mater. Atoms*, vol. 434, no. 1, pp. 23–28, 2018.
- [62] Y. Zhang, J. Wang, B. Liu, J. Wang, and H. Zhang, “Understanding the Behavior of Native Point Defects in ZrC by First-Principles Calculations,” *J. Am. Ceram. Soc.*, vol. 97, no. 12, pp. 4024–4030, 2014.

## II. EARLY STAGE OXIDATION OF $\text{ZrC}_x$ UNDER ION-IRRADIATION AT ELEVATED TEMPERATURES

Raul Florez<sup>a</sup>, Miguel L. Crespillo<sup>b</sup>, Xiaoqing He<sup>c,d</sup>, Tommi A. White<sup>c,e</sup>,  
Gregory Hilmas<sup>f</sup>, William G. Fahrenholtz<sup>f</sup>, Joseph Graham<sup>a,f\*</sup>

- <sup>a.</sup> Nuclear Engineering Program, Missouri University of Science and Technology,  
65409 Rolla, MO, United States
- <sup>b.</sup> Department of Material Science and Engineering, University of Tennessee, 37996  
Knoxville, TN, United States
- <sup>c.</sup> Electron Microscopy Core, University of Missouri, Columbia,  
Missouri 65211, United States
- <sup>d.</sup> Department of Mechanical and Aerospace Engineering, University of Missouri,  
Columbia, MO 65211, USA
- <sup>e.</sup> Department of Biochemistry, University of Missouri, Columbia,  
Missouri 65211, United States
- <sup>f.</sup> Department of Materials Science and Engineering, Missouri University of Science  
and Technology, 65409 Rolla, MO, United States

### ABSTRACT

The effects of irradiation on the morphology and microstructure of the oxide formed on the surface of  $\text{ZrC}_x$  during irradiation with 10 MeV  $\text{Au}^{3+}$  ions at 800° C were investigated. Nanosized oxide islands were observed on both unirradiated and irradiated sample areas, indicating that the early stage oxidation of  $\text{ZrC}_x$  proceeded via nucleation and growth. The reduction in size and surface coverage of oxide nodules at high doses, indicated that oxide dissolution was the predominant mechanism under irradiation

conditions. Nanometric cavities were observed in oxide islands for samples irradiated above 2.5 dpa. The underlying mechanisms driving these changes were discussed.

**Keywords: ZrC, ZrO<sub>2</sub>, Oxidation, Ion irradiation, Electron Microscopy, GIXRD.**

\* Corresponding author:

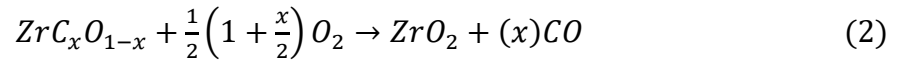
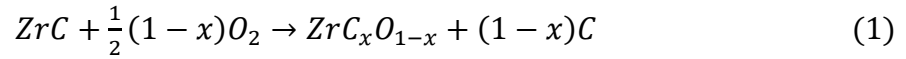
Email: grahamjose@mst.edu

## 1. INTRODUCTION

Zirconium carbide (ZrC<sub>x</sub>) is an ultra-high-temperature ceramic (UTHC) material with outstanding mechanical strength, high thermal and electrical conductivity, and low neutron absorption cross section [1], [2]. This unusual combination of properties makes ZrC<sub>x</sub> an attractive material for a variety of applications, including nuclear reactors [2], aerospace and propulsion devices [3], high power density microelectronics [4], and solar power concentrators [5]. Particularly in the nuclear field, ZrC<sub>x</sub> ceramics have gained significant interest as promising contenders for future advanced Generation-IV nuclear reactors and fusion systems. In these type of nuclear reactors ZrC<sub>x</sub> could potentially be used as an inert fuel matrix [6], a plasma facing component (PFC) [7], an oxygen getter for microencapsulated fuels [8], an alternative cladding for advanced non-light water reactors [9], and a fission product barrier in Tri-structural Isotropic (TRISO) fuel particles [10]. As a potential in-core material for the next generation of nuclear systems, ZrC would be subject to extreme operation conditions combining high radiation fluxes, elevated temperatures, mechanical stresses, and aggressive chemical environments.

The primary coolant system considered for Gen-IV high-temperature and very-high-temperature gas-cooled reactors (HTGRs and VHTRs) is helium gas, which is known for its chemical inertness [11]. Although the primary coolant system of HTRs and VHTRs is fitted with purification systems, impurities including  $H_2$ ,  $CO$ ,  $H_2O$ ,  $CO_2$ ,  $CH_4$ ,  $O_2$ , and  $N_2$  are inevitable in the coolant [12], [13], [14]. These impurities might arise from different sources including leaks into the cooling system, gas desorption from the nuclear fuel and other structural components, and nuclear fission reactions. Under prototypic operation conditions for gas-cooled reactor, the concentrations of impurities in the coolant system are in the part per million range [15]. Despite that, these impurities can induce corrosion reactions at high temperatures ( $>500^\circ C$ ), which can strongly affect the properties of the in-core reactor materials [16]. Previous studies have demonstrated that oxygen partial pressures ( $P_{O_2}$ ) as low as  $10^{-5}$  Pa can lead to the oxidation of  $ZrC_x$  ceramics at temperatures above  $500^\circ C$  [17]. As a result, the oxidizing impurities in the helium coolant bear the risk of oxidation of the  $ZrC$ -based components during the operation of gas-cooled reactors. In-service oxidation of  $ZrC_x$  may induce significant changes in thermophysical and mechanical properties of  $ZrC_x$  [18]. Moreover, the in-service oxidation of  $ZrC_x$  can enhance the release of gaseous fission products such as xenon (Xe) and helium (He) [19], [20]. Likewise, nanometric  $ZrO_2$  precipitates exhibit catalytic properties towards water splitting and hydrocarbon cracking [21], [22], which could enhance the uptake of other impurities into  $ZrC_x$ . Since the properties of  $ZrC_x$  can be seriously compromised by in-service oxidation, it is of important to elucidate the morphological and structural changes induced by oxidation of  $ZrC_x$ .

The oxidation behavior of  $ZrC_x$  ceramics at various experimental conditions has been extensively studied by a number of investigators [23], [24], [25] [26], [27], [28], [29], [30], [31]. When  $ZrC_x$  is exposed to an oxidizing atmosphere at elevated temperatures ( $> 500$  °C),  $ZrO_2$  and C are formed according to the following reactions:



Previous studies have recognized four different temperature regimes of oxidation for  $ZrC_x$  [18]. The low temperature regime occurs between 400 and 600 °C. In this regime, an oxide scale composed of amorphous  $ZrO_2$  and free carbon forms on the surface of the unoxidized  $ZrC_x$  matrix. Before the formation of  $ZrO_2$ ,  $ZrC$  goes through an oxycarbide transformation phase as described by reactions (1) and (2). The formation of the oxycarbide phase is quite rapid and the rate is controlled by the phase boundary reaction. The second oxidation regime occurs between 600 °C and 800 °C. In this temperature range, cubic zirconia (c- $ZrO_2$ ) starts to nucleate from the amorphous zirconia and the crystals begin to growth. Also, low levels of CO start to form by oxidation of free carbon. The kinetics in this regime are controlled by diffusion of oxygen through the scale with no significant stress on the c- $ZrO_2$  grains. The third regime occurs between 800 °C and 1000 °C. At these temperatures, the c- $ZrO_2$  crystals grow larger than 10 nm and monoclinic and tetragonal  $ZrO_2$  polymorphs begin to appear. Nearly all the free carbon inclusions are oxidized during this regime; therefore, a porous  $ZrO_2$  layer covers the surface. The kinetics in the third regime are controlled by oxygen grain boundary diffusion. Finally, at temperatures above 1200 °C, the zirconia layer (mostly m- $ZrO_2$ )

begins to sinter closing the pores created by CO<sub>2</sub> effusion. Uncertainty exists on the actual temperature and oxygen partial pressure values at which phase and rate controlling mechanism transitions occur.

Although the high temperature oxidation behavior of ZrC<sub>x</sub> has been extensively investigated during the last three decades, experimental data are lacking for the oxidation of ZrC under normal operating conditions in high temperature gas-cooled reactors. Until now, most of the published work has dealt with the oxidation of ZrC<sub>x</sub> following a loss of coolant accident (LOCA) [26], [27]. Under LOCA conditions, an oxide scale is rapidly formed on the surface of ZrC<sub>x</sub> due to the undesirable high-temperature exposure to an air-steam atmosphere. In contrast, in-service oxidation of ZrC<sub>x</sub> does not occur in oxygen-rich atmospheres; therefore, one can expect that the oxidation rate, surface composition and oxide structures would be different from those observed during LOCA scenarios. Many questions remain about the formation mechanism and the structure of the oxide formed on ZrC<sub>x</sub> during in-service operation in high temperature gas-cooled reactors. Particularly, the physical and chemical transformations that occur during the early stage of oxidation of ZrC<sub>x</sub> are not understood. A recent study by Pipon et al [32] indicated that the early stages of ZrC<sub>x</sub> oxidation are controlled by the nucleation and growth of discrete oxide nuclei, which are particularly prominent at low oxygen partial pressure and high temperatures. To the best of our knowledge, a detailed microstructural characterization of the initial oxides formed on the ZrC<sub>x</sub> surface during the early stages of the oxidation is not available. Therefore, elucidating the oxidation reaction and the microstructural evolution of the oxide scale at the early stages is essential to mitigate ZrC<sub>x</sub> oxidation in nuclear reactor systems. Additionally, the effects of radiation on the oxidation behavior

of  $\text{ZrC}_x$  remain largely unknown. Most studies listed above have performed only out-pile  $\text{ZrC}_x$  oxidation experiments. The main limitation of out-pile oxidation experiments is the absence of irradiation effects, which are ubiquitous in nuclear reactors. Radiation can significantly modify the oxidation behavior of  $\text{ZrC}_x$  compared to out-pile oxidation experiments by changing the properties of the ceramic matrix, the oxide formed on the surface, and the oxidizing environment [33],[34]. As far as we know, no previous studies have focused on in-pile oxidation of  $\text{ZrC}$ . Consequently, more experiments must be conducted to understand the effects of radiation on the oxidation behavior of  $\text{ZrC}_x$ . To this end, specimens must be irradiated under conditions of direct relevance to high temperature gas-cooled reactors, while simultaneously exposed to an oxidizing atmosphere with impurity levels similar to those encountered in the helium coolant of HTRs and VHTRs.

The purpose of this paper was to investigate the microstructure of the oxides formed on the surface of  $\text{ZrC}_x$  during ion irradiation with  $\text{Au}^{3+}$  ions at  $800^\circ\text{C}$ . The oxides were characterized for both the irradiated and unirradiated specimens to understand the effect of irradiation on the morphology and microstructure of the oxide scale. The results provide new insights into the early stage oxidation of  $\text{ZrC}_x$  under in-pile conditions relevant to high temperature gas-cooled nuclear reactors.



## **2. EXPERIMENTAL PROCEDURE**

### **2.1. SAMPLE PREPARATION**

A pellet of ZrC was prepared by hot-pressing commercial ZrC powder (Alfa Aesar, Reactor Grade, USA). The as-received powder was hot pressed in a 25.4 mm cylindrical graphite die lined with BN-coated (SP-180 Cerac, Milwaukee, WI) graphite foil (2010-A; Mineral Seal Corp, Tucson, Arizona). Before hot pressing, the powder was loaded into the die and cold compacted in a uniaxial press at ~2MPa. The powder was then heated under vacuum to 1600 °C with an average heating rate of 20 °C/min. At that time, the furnace was backfilled with helium and a uniaxial pressure of 32 MPa was applied to the powder compact. The furnace was then heated at 50 °C/min to 2200 °C. After 90 min, the furnace was cooled at ~50 °C/min. The load was removed when the die temperature dropped below 1600 °C.

Following densification, specimens for microscopy and ion irradiations were cut parallel to the hot pressing of the billet direction with a slow-speed diamond saw and then ground and polished to mirror-finish. The metallographic preparation was carried out by grinding the specimens with 100, 320, 600 and 1200 grit SiC pads with water as the lubricant. Felt pads and water-based diamond slurry suspensions were used for abrasive sizes from 3 µm to 0.25 µm. After polishing, the specimens were ultrasonically cleaned with ethanol for 15 min at room temperature.

### **2.2. ION IRRADIATIONS**

A rectangular ZrC foil (13 x 8 mm) was irradiated in the Ion Beam Materials Laboratory (IBML UT-ORNL) at the University of Tennessee, Knoxville [35] with 10

MeV Au<sup>3+</sup> ions at 800 C using a 3.0 MV tandem accelerator. Five different regions of the ZrC foil (3x3 mm each) were irradiated to doses of 0.5, 2.5, 5, 10, and 15 dpa. The total sample area comprised the five non-overlapping irradiated regions and one unirradiated control spot. Adjustable beam slits were used to define the irradiation areas. The ion beam was defocused and rastered in the horizontal and vertical directions with the aim of producing a region that was homogeneously irradiated. Beam homogeneity was verified by ion-induced luminescence from quartz targets and was found to be within 10% throughout the irradiated area [36]. The flux was set at  $1.0 \times 10^{12} \text{ cm}^{-2} \text{ s}^{-1}$  for all fluences. Low beam current densities in the range of  $5 \text{ nA mm}^{-2}$  were used to reduce any undesired effect and charge accumulation on the samples [37]. The vacuum chamber pressure was observed to be below  $5 \times 10^{-8}$  torr prior heating. Sample heating caused the pressure in the irradiation chamber to rise initially, but it decreased into the range of  $3\text{-}5 \times 10^{-7}$  torr during irradiation. The maximum outgassing of the specimen was observed around 170° C with vacuum pressure levels of  $7.8 \times 10^{-6}$  torr (Figure 1a). The Stopping and Range of Ions in Matter binary collision approximation (BCA) code 2013 version (SRIM-2013) [38] was used to estimate the displacement damage depth profile. Cascades were performed in quick-cascade mode (simple Kinchin and Pease model) assuming a density of  $6.71 \text{ g/cm}^3$  and threshold displacement energies of 37 eV for Zr and 16 eV for C [39] and C respectively. To compare ion and neutron irradiation results, the use of the quick Kinchin–Pease option in SRIM to compute radiation damage exposure has been recommended within the nuclear community [40]. The damage profile estimated from SRIM is determined by the sum of the predicted vacancy concentrations (using 'Knock-Ons' from Au ions and 'Vacancies' from target elements of Zr and C, together with the

replacement collisions [41]. Assuming a bulk ZrC sample, the predicted damage profile in displacements per atom (dpa) and the implanted Au ion profile are shown in Figure 1a. The peak dose under 10 MeV Au irradiation was located around 1000 nm below the surface. The conversion factor from ion fluence ( $10^{14} \text{ cm}^{-2}$ ) to local dose in the ZrC foil under quick simulation was 0.8343 dpa. The steady state temperature of the sample surface was measured via a K-type (chromel-alumel) thermocouple (TC). The TC was attached to the sample surface by molybdenum spring-loaded clips. Samples mounted on the high temperature stage were conductively heated from the platen. The rear of the platen was radiatively heated using a resistively heated tungsten filament. (ERH series heater and EPS-500 power supply, Thermionics Northwest, Inc.). High performance silver paste was used to improve the thermal contact between the bottom surface of the sample and the platen. More details on the experimental apparatus are provided elsewhere [35],[37]. Irradiations were performed with Au ions because of their relatively inert nature and large nuclear stopping cross section, which allows for a high damage rate per incident ion and minimal artifacts induced by the injected ions. It is worth noting that 10 MeV energy beam was chosen to obtain a relatively flat profile to a depth of 1  $\mu\text{m}$  without appreciable effects of implanted Au ions (Figure 1b). Moreover, intermediate energy heavy ion irradiations produce a displacement cascade density and morphology more similar to fission neutrons than light ions irradiation, which produces a more sparse sub-cascade morphology [42]. The temperature and range of doses were selected with the goal of studying radiation damage mechanisms in regimes relevant to the conditions in Gen-IV high temperature gas-cooled reactors and advanced fission and fusion reactor systems [43].

## 2.3. MATERIAL CHARACTERIZATION

This section presents a description of the different experimental techniques that were used in the present work to examine the samples.

**2.3.1. Density and Chemical Analysis.** The bulk density of the hot-pressed billet was measured by the Archimedes' method using distilled water as the immersing medium, according to ASTM C73-88 [44]. The relative density was calculated by dividing the Archimedes' density by the estimated theoretical density of ZrC ( $\rho=6.71 \text{ g/cm}^3$ ). The chemical analysis for carbon, oxygen and nitrogen contents of the billet was conducted by direct combustion method using the infrared absorption detection technique. Carbon (CS600; Leco, St. Joseph, MI), oxygen and nitrogen (TC500; Leco, St. Joseph, MI) contents were measured by crushing dense specimens to ~200 mesh. Three measurements were conducted for each element to establish repeatability.

**2.3.2. Grazing Incidence X-Ray Diffraction.** Grazing incidence X-ray diffraction (GIXRD) measurements were performed to evaluate structural modifications in the near surface region following high temperature ion irradiations. GIXRD profiles were collected on a PANalytical X'Pert Pro Multipurpose Diffractometer (MPD) fitted with a Cu X-ray tube and a X'Celerator detector. The diffraction patterns were acquired in grazing incidence geometry over the  $2\theta$  range 25 to 90 degrees with a step size of  $0.03^\circ$  and counting time of 0.5 s at each step. X-ray tube operation conditions were 40 kV and 40 mA.

**2.3.3. Electron Microscopy.** The surface morphology and composition were examined for both pristine and irradiated by focused ion beam (FIB)- scanning electron microscopy (FIB SEM, Scios<sup>TM</sup> DualBeam<sup>TM</sup>, FEI, Hillsboro, Oregon) coupled with

energy dispersive spectroscopy (EDS; Oxford Instrument Avignon UK). TEM specimens were also prepared using focused-ion-beam (FIB) lift out technique with a Scios<sup>TM</sup> DualBeam<sup>TM</sup> equipped with Ga focused ion beam. Before milling, a 2  $\mu\text{m}$  thick Pt layer was deposited the top surface of the specimen to protect it from ion beam induced damage and unwanted surface milling during FIB preparation. Trenching was performed at an ion beam voltage of 30 kV with a beam current of a few nanoamps. After lift-out, thinning of the lamella was first conducted with a beam current of hundreds of picoamps at 30 kV at  $\pm 5^\circ$  on both sides of the lamella using cleaning cross section mode until the lamella was  $\sim 1$   $\mu\text{m}$  thick. Voltages and currents were gradually reduced, and the milling angles decreased as the lamella got thinner. To complete preparation, a gentle polishing with  $\text{Ga}^+$  ions (5 keV and 48 pA) was used to remove damage caused by higher energy Ga bombardment. Microstructure characterization was performed using a 300 kV Technai F30 Supertwin transmission electron microscope (TEM). High resolution transmission electron microscopy (HRTEM) was used to reveal microstructural details of the oxide scale. Bright field (BF) imaging techniques were used to elucidate the radiation induced microstructural defects. Energy dispersive X-ray spectroscopy (EDX) and electron energy loss spectroscopy (EELS) were used for chemical composition studies.

### 3. RESULTS

#### 3.1. AS-SINTERED SAMPLE

The as-sintered ZrC pellet had a relative density of 93%. The carbon, oxygen and nitrogen content were 11.62, 0.144, and 0.0251 wt % respectively. Before annealing, the surface of the control specimen consisted of a homogeneous microstructure of ZrC grains with some residual porosity characteristic of non-fully densified billets. The average grain size was  $5.1 \pm 1.8 \mu\text{m}$ .

#### 3.2. ANNEALED UNIRRADIATED SAMPLE

GIXRD patterns obtained at  $\omega=0.5^\circ$  for the control specimen before and after thermal annealing in the ion irradiation vacuum chamber are presented in Figure 2a. The analyzed  $2\theta$  range included six peaks of the typical rock salt structure of ZrC ( $Fm\bar{3}m$ ) and the expected diffraction reflections for ZrO<sub>2</sub> polymorphs produced by the oxidation. Before annealing, XRD analysis revealed that nominally pure ZrC was the only crystalline phase present in the as-sintered billet. After annealing, new peaks corresponding to ZrO<sub>2</sub> polymorphs were observed in the XRD pattern. This result clearly indicates that the near surface area of the specimen was oxidized after exposure to the residual vacuum ( $<10^{-7}$  torr) of the ion accelerator chamber at 800 °C. The assignment of type of ZrO<sub>2</sub> polymorph could not be done unambiguously due to the closeness of the XRD peak positions for monoclinic (m), tetragonal (t) and cubic (c) ZrO<sub>2</sub> in the evaluated  $2\theta$  range. The peak at  $2\theta=30^\circ$  is due to the presence of either t- or c-ZrO<sub>2</sub> polymorph(s) and/or oxygen-deficient m-ZrO<sub>2-x</sub>.

Figure 2b shows GIXRD patterns, obtained at  $\omega$  values of 0.5, 1, 1.5, 3 and 5°, from the unirradiated ZrC sample after annealing for 5h at 800° C. The scans were recorded at several incident angles to probe microstructural changes at different penetration depths. The intensity of the ZrO<sub>2</sub> peaks decreased as the incident angle  $\omega$  increased, suggesting that the oxide phase was concentrated in the near surface region. Further analysis of the ZrC reflections revealed changes in the broadening and position of the peaks as a function of the incident angle  $\omega$ . ZrC peaks shifted to higher angles when the X-ray incident angle decreased. Peak shifting to higher  $2\theta$  angles is indicative of a contraction of the unit cell parameter, which could be produced by compositional changes across the probed area. In this case, the peak shifting could be attributed to the incorporation of adventitious oxygen into the ZrC lattice to form zirconium oxycarbide (ZrC<sub>x</sub>O<sub>y</sub>) [45]. The change in lattice parameter for ZrC is consistent with increasing oxygen content closer to the surface of the specimen.

FESEM plain view micrographs of the unirradiated specimen after annealing (Figure 3a) showed several morphological changes with respect to the original polished surface. First, the grain boundaries of the specimen were revealed due to the preferential thermal etching during annealing. Second, the surface was covered by discrete nanoprecipitates distributed homogeneously across the grains of the underlying ZrC<sub>x</sub>. The nanoprecipitates ranged in sizes between 20 and 100 nm. EDX elemental maps were acquired in the box area marked in Figure 3a to analyze the composition after annealing. The area selected for analysis included grain boundary regions where fewer of precipitates was observed. The elemental maps indicated that Zr, C and O were the major constituents on the surface area of the annealed sample (Figure 3b). The concentration of

zirconium and carbon was uniform across the analyzed area; whereas the concentration of oxygen was lower at the grain boundaries. This suggests that the nanoprecipitates observed in the SEM images contain oxygen, which is consistent with the detection of zirconium oxide by GIXRD. A standardless semi-quantitative EDX analysis of the mapping area (Figure 3c) gave the composition of 51 at% C, 45 at% Zr, and 4 at% O. Although oxygen enrichment is evident in the near surface area of oxidized specimen, the EDX signal from the nanoprecipitates on the surface can be easily overcome by contributions from the underlying  $\text{ZrC}_x$  matrix due to the large interaction volume of 20 keV electrons. Moreover, an accurate quantification of oxygen and carbon is not possible by EDX due to the low sensitivity of the technique for the light elements.

The density and sizes of the precipitates appeared to vary from grain to grain, suggesting that the nucleation and growth of the oxide islands was influenced by the crystallographic orientation of the underlying  $\text{ZrC}_x$ . The oxide nanoprecipitates seem to grow preferentially within the grain areas, while precipitate-denuded zones were observed near the grain boundaries. In general, the oxide particles had a lenticular shape with a faceted free surface and a rounded  $\text{ZrC}/\text{ZrO}_2$  interface (Figure S1a). The latter suggested high wettability of the oxide phase on the underlying  $\text{ZrC}_x$  substrate. Additionally, some of the oxide nanoislands began to coalesce with neighboring precipitates leading to the formation of larger oxide islands (Figure S1b). The coalescence indicated that coarsening of the oxide nanoprecipitates began at the early stages of the oxidation process, even when the grain boundaries were free of oxide nodules.



Cross-sectional HRTEM images of the unirradiated specimen after annealing is shown in Figure 4a. A multilayer structure was observed in the near region. The surface of the ZrC specimen was covered by a nanocrystalline layer  $\sim 4$  nm thick and, an amorphous layer. The chemical composition of the amorphous and nanocrystalline layers was probed by EELS. The STEM-high angle annular dark field (HAADF) image of the analyzed region (Figure 4b) showed a dark layer (Point A) and a uniform gray layer (Point B), which correspond to the amorphous and nanocrystalline layers observed in Figure 4a. The EELS spectrum obtained at point A (Figure 4c) confirmed that the amorphous layer was carbon rich. This carbon-rich layer could have been deposited on the surface of the specimen during preparation for TEM analysis. On the other hand, the EELS spectrum acquired at point B (Figure 4d) indicated that the nanocrystalline layer was most likely  $\text{ZrO}_2$ . Interestingly, the nanocrystalline  $\text{ZrO}_2$  layer showed conformal coverage on the surface of ZrC (Figure S3). Two elemental EELS line profiles reconstructed for O and Zr are shown in Figure 4e and 4f. Notably, the onsets of the O and Zr agreed with each other and can be clearly linked with the interface between the dark and the grey layers in the HAADF image. Furthermore, as shown in Figure 4f, underneath the nanocrystalline  $\text{ZrO}_2$  layer (layer I) was a layer of crystalline ZrC (layer II) that was  $\sim 25$  nm thick and oxygen rich compared to the bulk ZrC. The oxygen content decreased continuously from the top surface towards the unoxidized ZrC matrix. Such oxygen gradient suggested that the oxidation was promoted by the uptake of residual oxygen from the ion accelerator chamber during the annealing experiment.

Figure 5a shows a HRTEM image of an area of the annealed unirradiated sample where the continuity of the nanocrystalline oxide layer was interrupted by the formation

of larger nanosized islands. The chemical composition of the islands was consistent with  $\text{ZrO}_2$  as confirmed by EELS analysis (Figure 5d). The oxide islands had a characteristic elongated shape with the elongation direction roughly along the  $\{110\}$  direction of the ZrC substrate. Additionally, the islands were partially embedded into the ZrC matrix forming a sigmoidal interface between the oxide and the substrate. This interface appeared to be regular, well adhered and coherent. No precipitates of amorphous and/or crystalline carbon were observed at the interfacial region of the analyzed nanoislands. The intruded regions of the oxide precipitates had contact angles with the ZrC substrate ranging from 55 to 65°; whereas the protruded regions of the oxide nodule had wetting angles between 30 and 55°.

A Fast Fourier Transform (FFT) pattern was acquired at the red squared region indicated in Figure 5a. The obtained FFT pattern is shown in Figure 5b and can be well indexed along the  $[-121]$  zone axis based on a tetragonal  $\text{ZrO}_2$  structure (Inorganic Crystal Structure Database-66784). To confirm the validity of the indexing, a simulated electron diffraction pattern of the  $\text{ZrO}_2$  tetragonal structure was obtained using the Crystalmaker<sup>TM</sup> software (Figure 5c). Good agreement is obtained between the experimental and simulated FFT patterns. Fig. 5e shows the FFT pattern acquired from an area in Figure 5a that included both the nanoisland precipitate and the ZrC matrix. It is noted that the precipitate was epitaxially grown on the ZrC surface with the epitaxial relationship being  $(\bar{1}0\bar{1})_{\text{T}} // (002)_{\text{M}}$  and  $[\bar{1}21]_{\text{T}} // [110]_{\text{M}}$ .

### 3.3. IRRADIATED SAMPLES

The XRD patterns for the irradiated samples (Fig. S2) revealed the presence of defective but crystalline ZrC phase at all doses. Additionally, weak peaks were observed around  $2\theta=30^\circ$  in some of the irradiated specimens; although the intensity of this peak was too weak to be clearly deconvoluted from the background. The low intensity of the ZrO<sub>2</sub> peak in the irradiated samples could be because the volume fraction of ZrO<sub>2</sub> was too small to produce XRD peaks that were discernible from the background signal. Another possibility is that the oxide phase amorphized during irradiation. The surfaces of irradiated samples were analyzed as discussed below to characterize changes that occur during irradiation.

Figure 6 presents high resolution SEM micrographs of the surface of the control specimen and samples irradiated to 2.5, 10 and 15 dpa. Each image is shown together with the histogram of the maximum diameter of ZrO<sub>2</sub> nanoislands. Given the polyhedral shape of the precipitates, the maximum diameter was considered to provide information about both nanoisland size and shape. The morphological evolution of the oxide nanoislands coverages as a function of irradiation dose is shown in Figure 6. After annealing, the surface of control sample was decorated with large oxide islands with complex shapes, reflecting some coalescence of the oxide precipitates as the thermal annealing proceeded as discussed above. Irradiation shifted the distribution to finer sizes, increased the circularity of the islands, and reduced the grain area that was covered (Table 1). The shrinking and reshaping of the precipitates at higher doses suggested that radiation influenced the stability of the nanoislands.

High resolution TEM images of the oxide islands formed at different doses were taken from the [110] zone axis of the ZrC matrix (Figure 7.) Morphological and interfacial changes were observed in the oxide nodules as the irradiation dose is increased. At low doses (0.5 dpa), the oxide particles showed a double cap morphology with approximately half of the oxide island semi-embedded into the ZrC matrix and the other half protruded above the surface. Further analysis of the interfacial area revealed no coherent relationship between the oxide nodule and the ZrC matrix. As dose increased, the oxide islands tended to become more faceted and the interfacial region became more diffuse (Figure 7c, d and e). Interestingly, the phases of ZrO<sub>2</sub> tended to be monoclinic above 2.5 dpa after analyzing all the HRTEM images acquired, suggesting that irradiation affected the phase of the ZrO<sub>2</sub> that formed. Moiré fringes were observed at the oxide/matrix interface in some of the HRTEM images of irradiated samples. Faceted regions were also observed within the ZrO<sub>2</sub> islands irradiated above 2.5 dpa. Some of these regions had a characteristic octahedral shape with sizes ranging between 3 and 10 nm. Overfocus/underfocus TEM analysis was conducted on oxide nodules with faceted regions to elucidate the character of these microstructural features. Figure 8 shows the Fresnel contrast change under different focusing conditions in an oxide nodule irradiated to 5 dpa. The faceted regions appeared as white features in under-focused conditions and black features in over-focused conditions. This contrast change is characteristic of cavities, suggesting that the faceted regions could be voids or bubbles that formed under irradiation conditions [46].

## 4. DISCUSSION

### 4.1. EARLY STAGE OXIDATION OF ZrC

As shown in Figure 1, the gas pressure in the irradiation chamber increased substantially during heating of the target at temperatures between 150-170 °C. This observation indicates that gases desorbed from the specimen during this stage of the heating processes. The chemical composition of the outgassing products could not be identified in this study because the ion accelerator chamber at the IBML is not currently fitted with a residual gas analyzer. However, the pressure increase was probably produced by the release of carbon impurities and/or water vapor previously trapped or adsorbed in the solid during metallurgical preparation steps and handling of the sample. We speculate that these impurities could have played a role in the initial oxidation of ZrC. Similar outgassing processes could occur during the start-up and refueling stages of high temperature gas-cooled reactors [47]. Therefore, the experimental conditions inside the irradiation chamber observed in this experiment are akin to those expected in the nuclear reactor core.

The discrete oxide nanostructure observed on the surface of the unirradiated sample after annealing indicates that the oxidation process was on going. At the early stages, the oxidation of ZrC proceeds through nucleation and growth of oxide precipitates as depicted in Figure 3 and 5. These results are similar to those obtained by Pipon et al. [19] after annealing  $\text{ZrC}_{0.95}\text{O}_{0.05}$  at 1400°C in dynamic secondary vacuum ( $10^{-5}$  Pa) for 3 hours. The early oxidation of other UTHCs and metals has also been found to proceed via nucleation and growth of oxide nanoislands under high temperature and vacuum

conditions [48], [49], [50]. Alternatively, the formation of oxide islands can be due to dewetting of the thin oxide passivation layer formed at the early stages of the oxidation process. Due to excess surface free energy, thin oxide films are unstable and when they are heated, they will dewet or agglomerate to form islands [51]. Dewetting and nanopattern formation can be further induced by ion-irradiation [52]. Future work *In-situ* oxidation experiments in an environmental TEM instrument to confirm oxide dewetting at the early stages of  $ZrC_x$  oxidation.

The double-layer structure of the oxide scale observed in the unirradiated specimen after annealing (Figure 4) is consistent with the morphological changes expected according to the oxidation mechanism proposed by Katoh [2]. In the present work, an oxygen gradient was detected by EELS analysis in the near surface area of the annealed specimen (Figure 4b). The decrease in oxygen content with increasing distance from the surface suggests that oxygen dissolution occurred at the interface, forming an oxycarbide compound in the near surface area of the sample. Because of the sub-stoichiometric nature of the as-sintered billet used in this study (detected by Raman measurements, not shown here), it is conceivable that oxygen diffused towards carbon vacancies in  $ZrC_x$  (Equation. 3)



Experimental work by Shimada and Ishii [23] showed that the  $ZrC_x$  containing dissolved oxygen becomes thermodynamically unstable after the oxygen concentration exceeds the solubility limit. As a result, the oxycarbide solution decomposes into a layer of amorphous zirconia and free carbon. Subsequently,  $ZrO_2$  crystallites nucleate and growth from this amorphous layer and forms a continuous film at longer oxidation times.

Similar results were obtained in this study for the oxidation of the unirradiated sample. Figure 4a shows that an outer thin layer of nanocrystalline  $\text{ZrO}_2$  (around 4 nm thickness) was formed on the top surface of the unirradiated sample after high vacuum thermal annealing.

Previous studies suggest that free carbon is retained in the amorphous layer below  $800^\circ\text{C}$  and evolves as  $\text{CO}$  or  $\text{CO}_2$  at higher temperatures [23]. However, in all previous studies  $\text{ZrC}$  was oxidized for longer times and with an abundance of oxygen. Those conditions favor the formation of an oxide film that results in a uniform oxygen activity macroscopically across the sample. The gradient in oxygen activity perpendicular to the surface promotes the retention of carbon under the oxide scale as observed extensively in previous work. However, in our case the oxidation has just been initiated and it is unlikely that a global change in the oxygen activity occurs at such early stages of the oxidation process.

Cross sectional TEM images of the oxide scale also revealed that the  $\text{ZrO}_2$  crystallites were partially embedded into the underlying  $\text{ZrC}$  matrix rather than lying on the top surface (Figure 5a). This embedding behavior has been previously observed in the early stage oxidation of other pure metals and alloys [53], [54], [55]. Embedding of the oxide embryos suggests that the oxide islands are formed by a 3D nucleation mechanism, which occurs when the surface mobility of oxygen is the dominant transport mechanism for the initial oxide formation [56]. Under such conditions, atomic oxygen diffuses over the surface and react with the underlying substrate atoms to form semi-buried oxide embryos. The formation of an internal oxide/substrate interface could also

provide a fast pathway for oxygen diffusion into the matrix, which might contribute to further embedding of the oxide island during the growth stage.

The formation of sub-stoichiometric zirconia seems possible considering the low oxygen partial pressure and high temperature conditions used in this study. Ma et al. [57] have previously reported the formation of sub-oxides  $\text{ZrO}_{2-x}$  during the oxidation of Zr under high vacuum conditions ( $P_{\text{O}_2} < 10^{-8}$  torr). Similarly, the occurrence of oxygen deficient m- $\text{ZrO}_2$  has been observed at the interfacial region between the carbide and oxide during oxidation of  $\text{ZrC}_x$  [26]. On the other hand, the presence of t/c- $\text{ZrO}_2$  polymorph(s) cannot be dismissed either. Prior studies on ZrC oxidation have reported the formation of metastable t/c- $\text{ZrO}_2$  phases during the oxidation of ZrC [58][26]. The stabilization of t/c- $\text{ZrO}_2$  at temperatures below the conventional polymorphic stability range of these phases could be caused by several factors including crystallite size, strain, and structural defects. According to Garvie's theory [59], the formation of t-  $\text{ZrO}_2$  is favored below a critical crystallite size of 10 nm because of the lower surface free energy of t-  $\text{ZrO}_2$  compared to m-  $\text{ZrO}_2$ . Likewise, stabilization of t-  $\text{ZrO}_2$  could be induced by strain effects [60]. Compressive stresses generated by Pilling-Bedworth ratio (PBR) effect and heteroepitaxial growth of the oxide can increase the critical size of stabilized t-  $\text{ZrO}_2$  up to 200 nm [61], [62]. The presence of structural defects has been also proposed as a mechanism for t/c  $\text{ZrO}_2$  polymorphs stabilization. According to Shukla and Seal [61], the stabilization of tetragonal and cubic  $\text{ZrO}_2$  can be attributed to the presence of oxygen ion vacancies generated either at higher temperature, or in vacuum, or by doping trivalent impurities. In our case, the oxide was formed under high temperature and vacuum conditions, which are conducive for the formation of oxygen vacancies.



## 4.2. OXIDATION UNDER IRRADIATION CONDITIONS

For the irradiated samples, some of the large  $\text{ZrO}_2$  nanoislands exhibits a series of structural defects (Figure 6); however, they remained crystalline even after irradiation at the highest dose evaluated in this work (15 dpa). This result agrees with previous experimental data [63], [64] and first principle simulations [65], [66], which indicate the high amorphization resistance for  $\text{ZrO}_2$  polymorphs under irradiation conditions. The high radiation tolerance of  $\text{ZrO}_2$  has been attributed to the large amount of native oxygen vacancies that enhances the dynamic recovery of the radiation induced defects [67].

Under irradiation conditions, the oxide islands are subject to several radiation-induced processes that determine their morphological and microstructural evolution (Figure 9b). The protruded regions of the  $\text{ZrO}_2$  nodules are sputtered by the incident ion beam. As shown in Figure 6, the protruded regions of the nanoislands tended to become more faceted at higher doses. The reshaping of islands was more noticeable on the sides parallel to ion beam direction, suggesting that preferential ion sputtering occurred along this direction. Ballistic collisions with the  $\text{Au}^{3+}$  ions could also produce ion beam mixing at the  $\text{ZrO}_2/\text{ZrC}$  interface. As indicated by the yellow boxes in Figure 6, irradiation tended to make the oxide/matrix interface more diffuse. Furthermore, Moiré fringes were observed in some of the irradiated precipitates. These observations were indicative that intermixing between the oxide particles and  $\text{ZrC}$  phases occurred during the ion irradiation of the specimens. Surface sputtering and ballistic mixing could enhance the dissolution of the oxide precipitates under radiation exposure. The atoms ejected out of the oxide particles might undergo three different processes: (i) dissolve into the  $\text{ZrC}$  matrix, (ii) diffuse back into the parent particle or being absorbed by other particles, and

(iii) re-nucleate to form new particles with other solute atoms in the ZrC matrix. The last two processes depend much on the diffusion of solute atoms, particularly oxygen atoms. Interestingly, no “halo” effect (i.e. formation of smaller oxide nanoparticles around the periphery of the islands) was observed in the oxide/matrix interface for the irradiated samples. This suggests that the local composition of oxygen ejected from the islands does not exceed the solubility limit in the irradiated ZrC matrix. Thus, the nucleation and growth of smaller oxide clusters around the island is not possible. The absence of ‘haloing’ may be also related to other radiation-induced effects. Firstly, the supersaturation of defects created under irradiation conditions can increase the oxygen solubility in the matrix [68]. Since the solubility increases during the irradiation, atoms ejected by ballistic mixing may be in solution during irradiation. Secondly, the defect supersaturation can produce enhancement of diffusion processes [69]. Radiation-enhanced diffusion of sufficiently mobile species might occur either through vacancies or interstitials and can significantly alter the size and stoichiometry of the oxide islands. Previous experimental studies on sub-stoichiometric  $\text{ZrC}_x$  indicate that the presence of vacancies in the matrix can enhance the diffusion of oxygen towards the bulk [70]. It is conceivable that the diffusion of oxygen atoms in substoichiometric  $\text{ZrC}_x$  occurs by an octahedral vacancy mechanism as observed experimentally in other group-IV carbides [71]. Additionally, other fast diffusion paths might be also operative under irradiation conditions, including dislocation loops and planar defects introduced in the irradiated microstructure as the dose increased.

As shown in Table 2, each of the irradiated areas in the ZrC foil endured different annealing times before and after ion irradiation. In general, longer pre-annealing time and

lower doses lead to bigger oxide nodules on the surface of ZrC. It is noted that Increasing the post annealing time (i.e after ion irradiation) at higher doses does not produce coarsening of the oxide nanostructure. The region irradiated at the highest dose (15 dpa) was covered by small oxide precipitates. This behavior suggested that the nucleation and growth of the nanoislands is affected by the microstructure of the underlying ZrC substrate. At higher doses, more defects are created in ZrC enhancing the dissolution of oxygen towards the bulk ceramic. Similar effects have been observed in SiC [72].

Faceted pockets were also observed in the ZrO<sub>2</sub> islands for specimens irradiated at 2.5 dpa and above doses (Figure 5d, f). These pockets were not observed in the oxide nodules for the control and 0.5dpa-irradiated samples, indicating that radiation could have played a role on their formation. Furthermore, the pockets exhibited the characteristic Fresnel contrast of cavities in under-focus and over-focus BFTEM images (Figure 8). This strongly suggested that pockets might be voids/bubbles that formed within ZrO<sub>2</sub> the islands under irradiation. Cavities were not expected from the published temperature/fluence damage mechanism maps for ZrO<sub>2</sub>. A possible mechanism for the formation and growth of cavities in the oxide nodules may be explained by oxygen diffusion and vacancy clustering processes. Due to small defect formation and migration barriers for oxygen compared to zirconium[73], the radiation response of ZrO<sub>2</sub> is mostly determined by the evolution of the surplus of oxygen point defects created during the irradiation. In the case of the oxide islands, the highly mobile oxygen atoms could migrate towards the free surface of the nodules and the ZrO<sub>2</sub>/ZrC interface. The oxygen atoms that reach the free surface are no longer tightly bonded to the island and are lost; whereas those atoms that migrate towards the interface are dissolved into ZrC<sub>x</sub>. Previous

studies on ion irradiation of nanometric  $\text{ZrO}_2$  indicate that a significant loss of oxygen occurs as the dose is increased [74]. Therefore, an accumulation of oxygen vacancy is expected in the  $\text{ZrO}_2$  nodule upon irradiation. A supersaturation of vacancies may become the driving force for the nucleation and growth of cavities in  $\text{ZrO}_2$  nodules at high doses. The process could be further assisted by the adsorption and absorption of inert gases present in the irradiation chamber, which may act to stabilize the void embryo and enhance their nucleation process. It can also be assumed that the voids are not pressurized because gas filled voids tend to have more spherical shapes rather than polyhedral ones.

The schematic model shown in Figure 9 summarizes the microstructural and morphological changes of the oxide islands observed in this work. In the absence of irradiation (Figure 9a), the oxidation of  $\text{ZrC}$  proceeds via nucleation and growth of  $\text{ZrO}_2$  islands. The oxide islands will growth and coalesce as the oxidation progresses, and finally an oxide film will form on the surface at the later stages of the oxidation process. On the other hand, the evolution of the early oxide nanostructure under irradiation conditions (Figure 9b) is determined by a combination of radiation-induced processes such as ballistic dissolution, surface sputtering and radiation-enhanced diffusion (RED). The shrinkage of the oxide nodules under irradiation can be explained by the enhancement of the oxygen solubility and diffusivity in the implantation layer during irradiation due to the creation of radiation induced defects. More research is needed to evaluate the mechanisms of oxygen diffusion in the irradiated microstructure and determine the influence of defect evolution on the oxygen uptake process. Finally, the formation of cavities at doses above 2.5 dpa could be associated with the loss of oxygen

from the irradiated oxide nodules and the concomitant vacancy supersaturation. The nucleation and growth of vacancies could also be assisted by the adsorption of inert gases present in the beamline vacuum chamber.

## 5. CONCLUSIONS

This study investigated the morphology and microstructure of the oxidation scale formed on the surface of ZrC during irradiation with  $\text{Au}^{3+}$  ions at 800 °C. GIXRD and electron microscopy (SEM/TEM) techniques were used to characterize the radiation response of the oxide at doses ranging from 0.5 to 15 dpa. Subsequent analysis was used to draw the following conclusions:

- The early stage oxidation of  $\text{ZrC}_x$  under prototypical operation conditions of high temperature gas-cooled reactors proceeds via nucleation and growth of oxide islands rather than uniform oxide film growth. Cross-sectional TEM analysis suggested that the oxide nodules were formed by a 3D nucleation mechanism.
- Radiation affected the stability of the oxide scale at the early stages of  $\text{ZrC}_x$  oxidation. Evidence of oxide dissolution was observed in samples that were irradiated up to doses of 15 dpa. Morphological changes were also observed in the irradiated oxide islands as a function of dose. At high doses (>2.5 dpa), the oxide islands became more faceted and exhibited diffuse oxide/matrix interfaces. These results indicated that radiation-induced processes could enhance the dissolution of oxide precipitates under irradiation conditions.

Additionally, radiation introduced defects in the oxide nodules. Nucleation and growth of cavities was observed within the oxide nodules irradiated to 2.5 dpa and above.

- The oxide formed in  $\text{ZrC}_x$  has a high radiation-induced amorphization resistance. Although defects were observed in the oxide nodules, no amorphization of the  $\text{ZrO}_2$  precipitates was observed under irradiation up to doses of 15 dpa. Some metastable phases of  $\text{ZrO}_2$  were observed in the irradiated specimens.

## ACKNOWLEDGEMENTS

This research was supported by Nuclear Regulatory Commission Faculty Development Grant NRC-HQ-84-15-G-0044 and by the Ceramics program of the U.S. National Science Foundation as part of project DMR 1742086. The microscopy work was conducted at the Electron Microscopy Center (EMC) of the University of Missouri Columbia with partial funding through the EMC Excellence Microscopy Award. Material synthesis and X-ray diffraction measurements were performed using facilities of the Materials Research Center (MRC) located at the Missouri University of Science and Technology. Ion irradiations were performed at the Ion Beam Materials Laboratory located at the University of Tennessee, Knoxville.

Table 1. Statistical data related to the morphology and distribution of the oxide nanoislands as a function of irradiation dose.

<b>Dose (dpa)</b>	<b>Coverage (%) <math>\pm</math> 10%</b>	<b>Circularity <math>\pm</math>10%</b>
0	32.78	0.86
2.5	29.37	0.89
10	26.75	0.93
15	24.24	0.96

Table 2. Pre-annealing, irradiation and post-annealing times for each specimen.

<b>Region</b>	<b>Dose (dpa)</b>	<b>Pre- annealing [min]</b>	<b>Irradiation [min]</b>	<b>Post- Annealing [min]</b>
1	15	~ 140	30	~ 55
2	10	~ 170	20	~ 30
3	5	~ 180	10	~ 20
4	2.5	~ 190	5	~ 15
5	0.5	~ 195	1	~ 5
6	0	~ 196	0	0

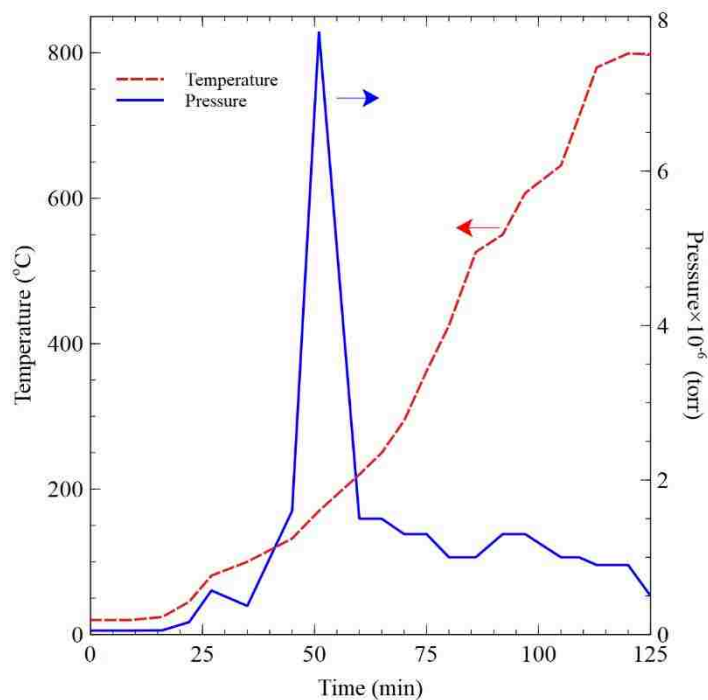


Figure 1. Pressure and temperature evolution of the ion chamber before to the onset of ion irradiation.

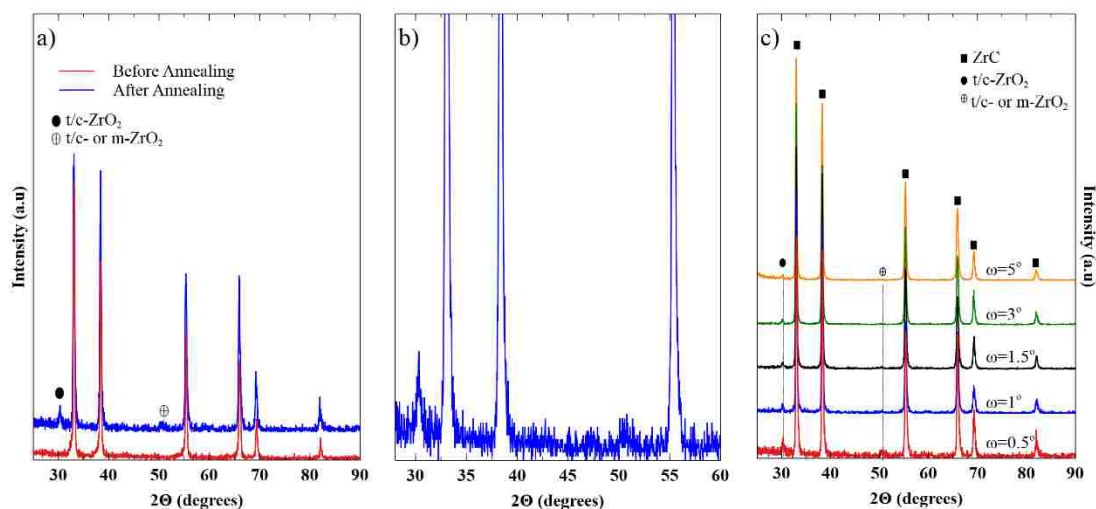


Figure 2. (a) GIXRD patterns obtained from ZrC control sample before and after thermal annealing in the ion irradiation chamber at 800 °C, (b) (a) GIXRD obtained from ZrC control sample after thermal annealing collected at various x-ray incident angles.



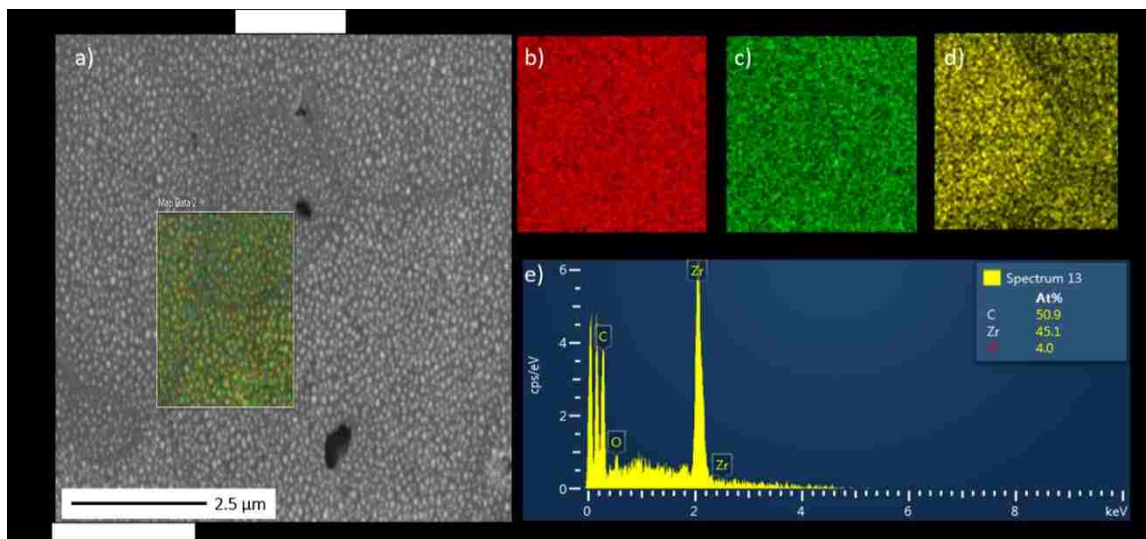


Figure 3. (a) Secondary electron SEM image of the surface topography of the control sample showing presence of oxide nodules after thermal annealing in the irradiation chamber, (b) EDX compositional maps for C, Zr and O acquired in the box area in (a), (c) EDX spectra and standardless compositional quantification for the mapping area.

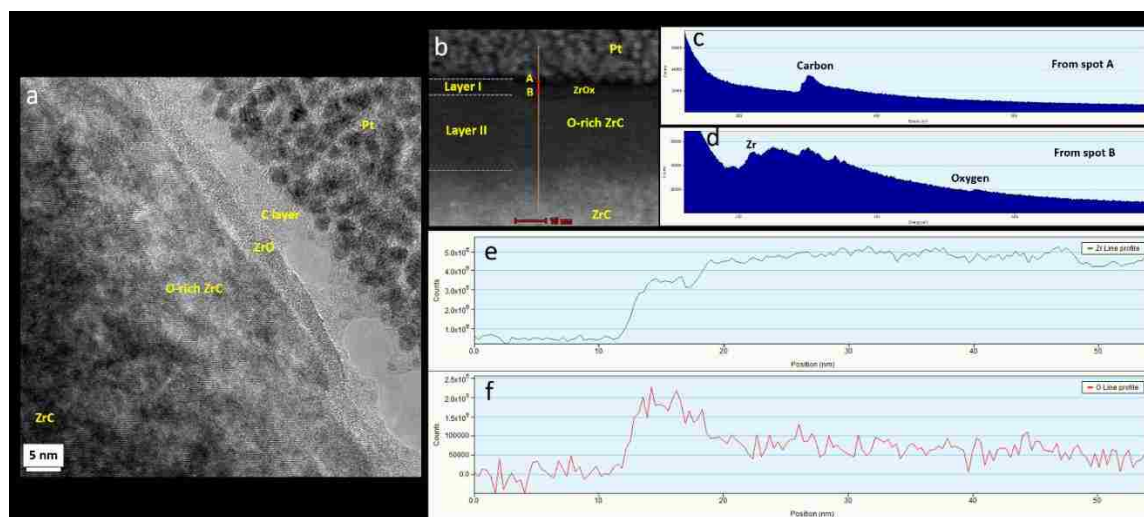


Figure 4. (a) HRTEM image of the near surface area of the control specimen after annealing in the irradiation chamber (b) STEM-HAADF image with the EELS line profile. Two EELS spectrum are extracted from the spot A and spot B from the line profile, shown in the (c) and (d) respectively, confirming the amorphous C and nanocrystalline ZrOx layer in (a). Elemental line profile of Zr I and O (f).

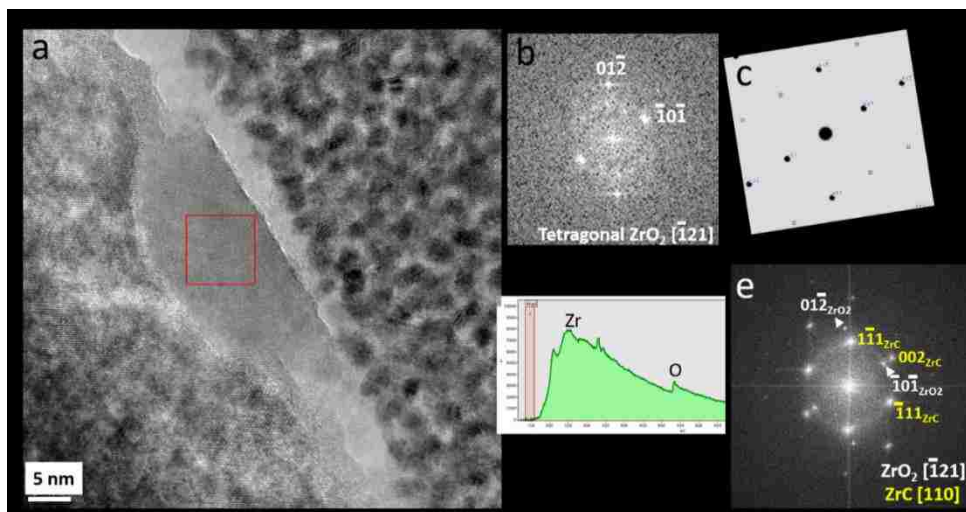


Figure 5. (a) HRTEM image of a precipitate embedded in the ZrC matrix. (b) FFT pattern from the red squared region in a can be indexed to be tetragonal ZrO<sub>2</sub> along its  $[1\bar{2}1]$  zone axis. (c) The simulated electron diffraction pattern based on the tetragonal structure match well the experimental FFT. (d) EELS spectrum from the precipitate, confirming it is ZrO<sub>2</sub>. (e) IFFT pattern from both ZrC and precipitate ZrO<sub>2</sub> showing the epitaxial relationship between them.

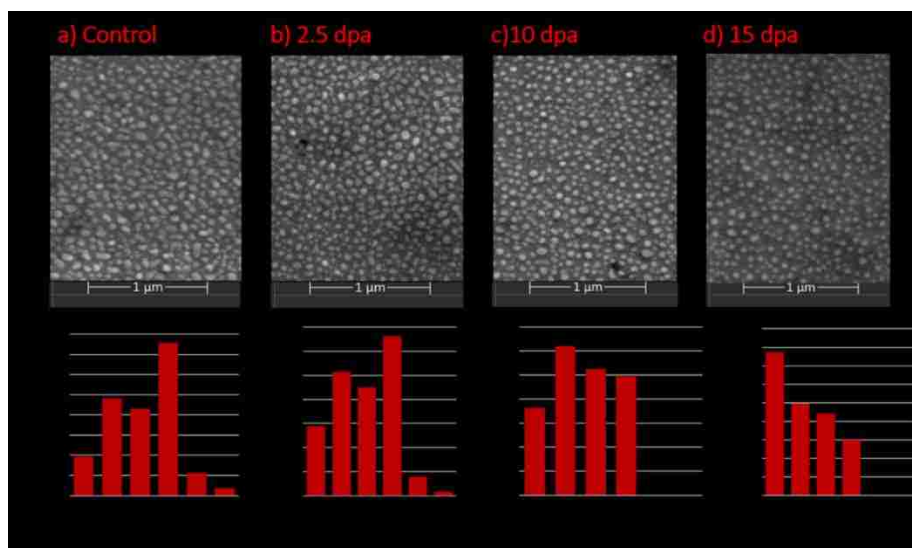


Figure 6. Morphology of the nanostructured ZrO<sub>2</sub> nanoparticles obtained by SEM as a function of irradiation dose (a) Control sample, (b) 2.5 dpa, (c) 10 dpa, (d) 15 dpa. Statistical histograms of the oxide islands for each sample are reported below the SEM micrographs.

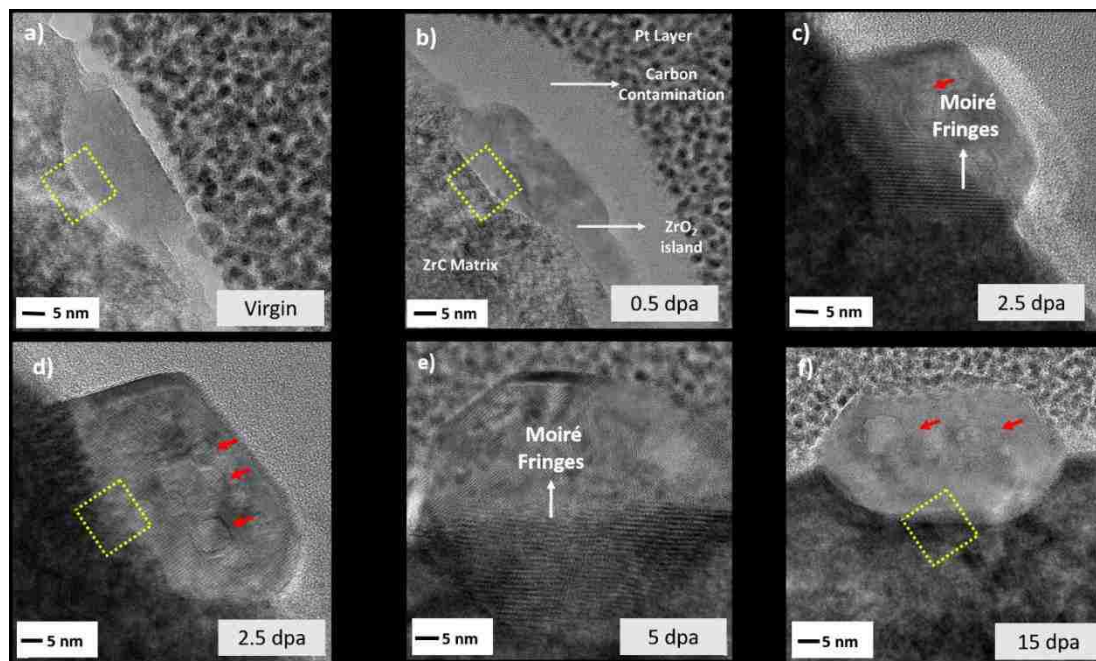


Figure 7. HRTEM images of oxide island formed (a) control sample, and samples irradiated to (b) 0.5 dpa, (c) and (d) 2.5 dpa, (e) 5 dpa, and (f) 15 dpa.

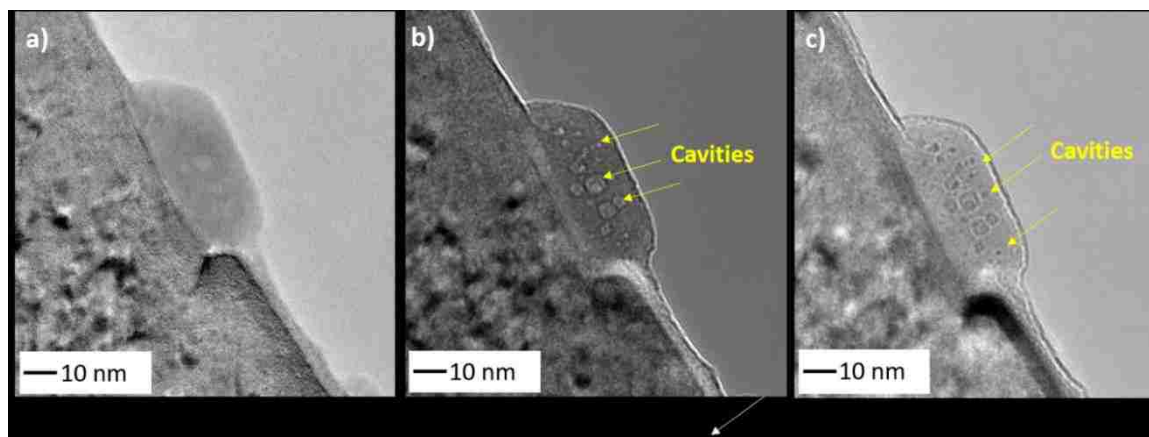


Figure 8. Cavity morphology in the ZrO<sub>2</sub> island after irradiation to 5 dpa (a) in-focus, (b) underfocused, and (c) overfocused BF-TEM images showing changes in Fresnel contrast for the cavities.

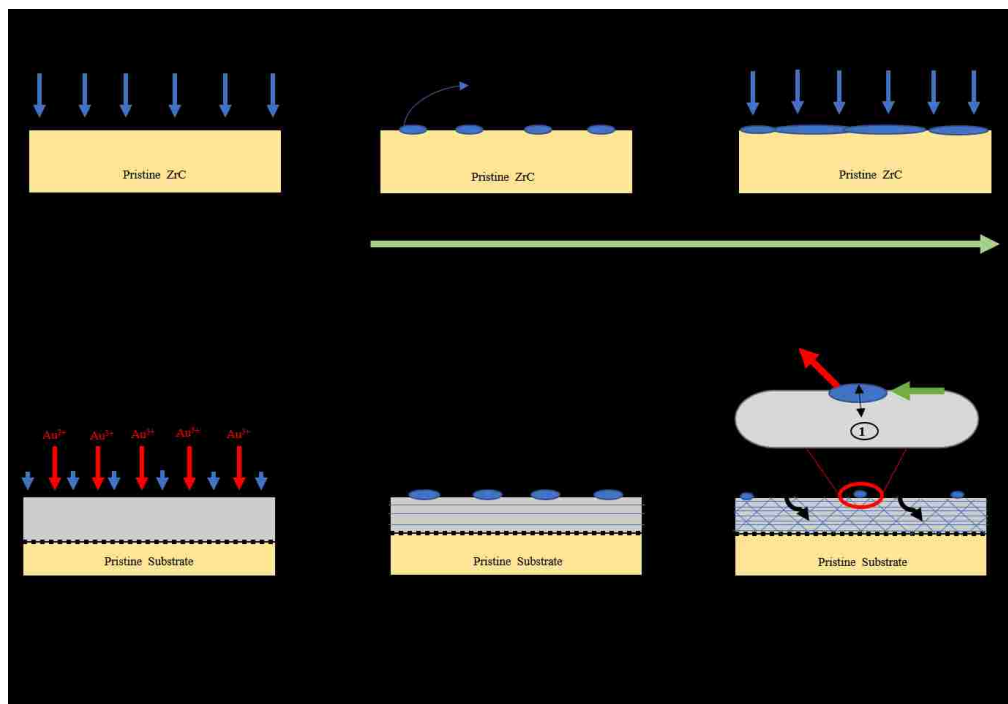


Figure 9. Schematic model of the early oxide growth a) without ion irradiation, and b) under ion-irradiation conditions.

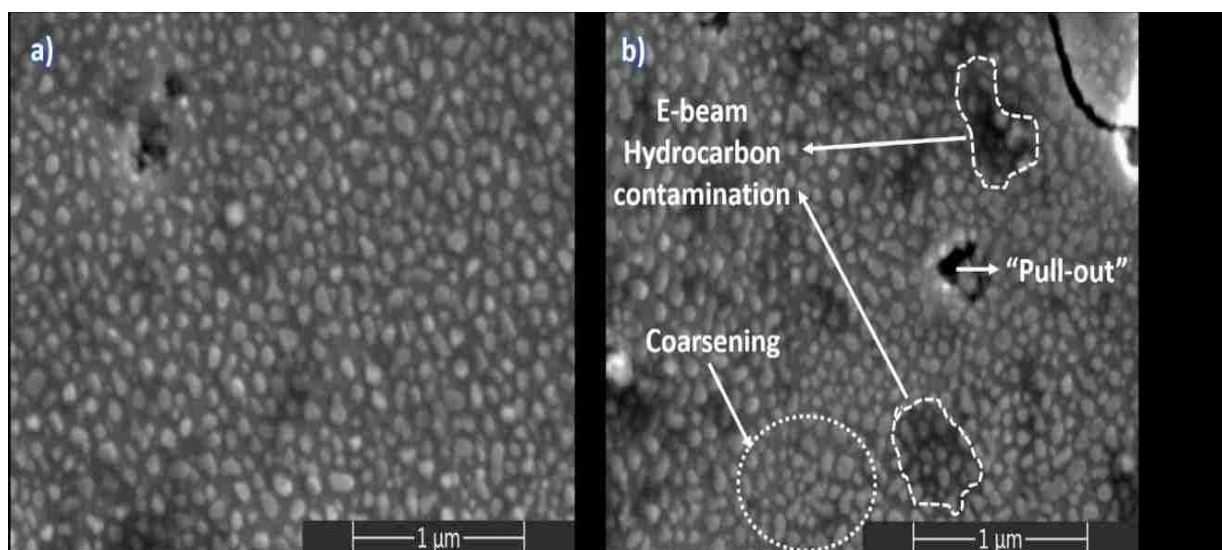


Figure S1. Secondary electron SEM images of the surface topography of the control sample showing presence of oxide nodules after thermal annealing in the irradiation chamber.



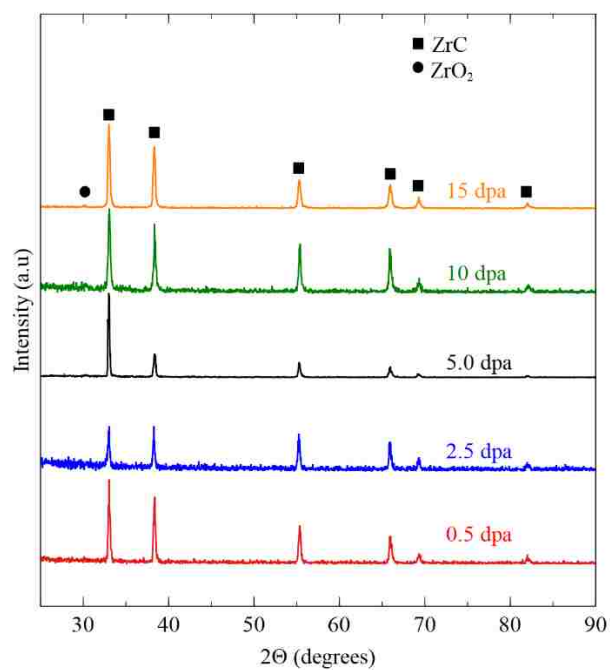


Figure S2. GIXRD patterns obtained from irradiated ZrC sample ( $\omega=0.5^\circ$ )

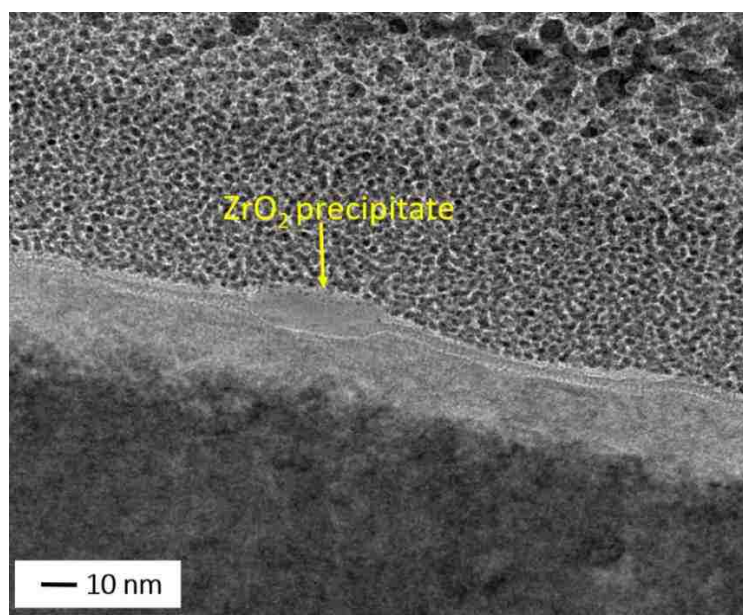


Figure S3. Conformal nanocrystalline  $\text{ZrO}_2$  layer formed on the top of the unirradiated specimen after thermal annealing.

## REFERENCES

- [1] H. F. Jackson and W. E. Lee, “Properties and characteristics of ZrC,” R.J.M. Konings (Ed.), *Compr. Nucl. Mater.*, Elsevier, Oxford (2012), pp. 339-372
- [2] Y. Katoh, G. Vasudevamurthy, T. Nozawa, and L. L. Snead, “Properties of zirconium carbide for nuclear fuel applications,” *J. Nucl. Mater.*, 441 (2013), pp. 718-742
- [3] X. T. Shen, L. Liu, W. Li, and K. Z. Li, “Ablation behaviour of C/C-ZrC composites in a solid rocket motor environment,” *Ceram. Int.*, 41 (2015), pp. 11793-11803
- [4] R. Ganter, R. J. Bakker, C. Gough, M. Paraliiev, M. Pedrozzi, F. Le Pimpec, L. Rivkin, A. Wrulich, “Nanosecond field emitted and photo-field emitted current pulses from ZrC tips,” *Nucl. Instruments Methods Phys. Res. Sect. A Accel. Spectrometers, Detect. Assoc. Equip.*, 565 (2006), pp. 423-429
- [5] B. Pierrat, M. Balat-Pichelin, L. Silvestroni, and D. Sciti, “High temperature oxidation of ZrC-20%MoSi<sub>2</sub> in air for future solar receivers,” *Sol. Energy Mater. Sol. Cells*, 95 (2011), pp. 2228-2237
- [6] G. Vasudevamurthy, T. W. Knight, E. Roberts, and T. M. Adams, “Laboratory production of zirconium carbide compacts for use in inert matrix fuels,” *J. Nucl. Mater.*, 374 (2008), pp. 241-247
- [7] R. Liu, Z. M. Xie, J. F. Yang, T. Zhang, T. Hao, X. P. Wang, Q. F. Fang, C. S. Liu, “Recent progress on the R&D of W-ZrC alloys for plasma facing components in fusion devices,” *Nucl. Mater. Energy*, 16 (2018), pp. 191–206
- [8] D. Wongsawaeng, “Performance modeling of Deep Burn TRISO fuel using ZrC as a load-bearing layer and an oxygen getter,” *J. Nucl. Mater.*, 396 (2010), pp. 149-158
- [9] K. A. Terrani, “Accident tolerant fuel cladding development: Promise, status, and challenges” *J. Nucl. Mater.*, 501 (2018), pp. 13-30
- [10] I. E. Porter, T. W. Knight, M. C. Dulude, E. Roberts, and J. Hobbs, “Design and fabrication of an advanced TRISO fuel with ZrC coating,” *Nucl. Eng. Des.*, 259 (2013), pp. 180–186

- [11] R. Wright, J. Wright, and C. Cabet, "Material performance in helium-cooled systems," R.J.M. Konings (Ed.), *Compr. Nucl. Mater.*, Elsevier, Oxford (2012), Vol. 5, pp. 251-277
- [12] J. Berka, T. Hlinčík, I. Viden, T. Hudský, and J. Vít, "The design and utilization of a high temperature helium loop and other facilities for the study of advanced gas-cooled reactors in the Czech Republic," *Prog. Nucl. Energy*, 85 (2015), pp. 156-163
- [13] N. Sakaba, T. Furusawa, T. Kawamoto, Y. Ishii, and Y. Oota, "Short design descriptions of other systems of the HTTR," *Nucl. Eng. Des.*, 233 (2004), pp. 147-154
- [14] H. Chang, Z. X. Wu, and H. J. Jia, "Experimental study on cryogenic adsorption of methane by activated carbon for helium coolant purification of High-Temperature Gas-cooled Reactor," *Ann. Nucl. Energy*, 101 (2017), pp. 367-374
- [15] S. Hamamoto, Y. Shimazaki, T. Furusawa, T. Nemoto, H. Inoi, and S. Takada, "Investigation of chemical characteristics of primary helium gas coolant of HTTR (high temperature engineering test reactor)," *Nucl. Eng. Des.*, 271 (2014), pp. 487-491
- [16] V. Pauly, C. Tesch, J. Kern, M. Clark, D. Grierson, D. Singh, O. Ajayi, K. Sridharan, "High-temperature tribological behavior of structural materials after conditioning in impure-helium environments for high-temperature gas-cooled reactor applications," *J. Nucl. Mater.*, 522 (2019), pp. 311-323
- [17] G. Gutierrez, N. Toulhoat, N. Moncoffre, Y. Pipon, A. Maître, M. Gendre, A. Perrat-Mabilon, "Thermal behaviour of xenon in zirconium carbide at high temperature: Role of residual zirconia and free carbon," *J. Nucl. Mater.*, 416 (2011), pp. 94-98
- [18] Y. Pipon, N. Toulhoat, N. Moncoffre, G. Gutierrez, A. Maître, and M. Gendre, "Influence of the Oxygen content on the thermal migration of Xenon in  $\text{ZrC}_x\text{O}_{1-x}$ ," *J. Nucl. Mater.*, 440 (2013), pp. 546-552
- [19] S. Agarwal, A. Bhattacharya, P. Trocellier, and S. J. Zinkle, "Helium induced microstructure damage, nano-scale grain formation and helium retention behaviour of ZrC," *Acta Mater.*, 163 (2019), pp. 14-27
- [20] T. Yamaguchi, "Application of  $\text{ZrO}_2$  as a catalyst and a catalyst support," *Catal. Today*, 20 (1994), pp. 199-217
- [21] M. V. Ganduglia-Pirovano, A. Hofmann, and J. Sauer, "Oxygen vacancies in transition metal and rare earth oxides: Current state of understanding and remaining challenges," *Surface Science Reports*. 62 (2007), pp. 219-227

- [22] S. Shimada and T. Ishil, "Oxidation Kinetics of Zirconium Carbide at Relatively Low Temperatures," *J. Am. Ceram. Soc.*, 73 (1990), pp. 2804-2808
- [23] S. Shimada, M. Yoshimatsu, M. Inagaki, and S. Otani, "Formation and characterization of carbon at the ZrC/ZrO<sub>2</sub> interface by oxidation of ZrC single crystals," *Carbon*, 36 (1998), pp. 1125-1131
- [24] S. Shimada, "Oxidation and Mechanism of Single Crystal Carbides with Formation of Carbon.," *J. Ceram. Soc. Japan*, 109 (2001), pp. 33-42
- [25] C. Gasparrini, R. J. Chater, D. Horlait, L. Vandeperre, and W. E. Lee, "Zirconium carbide oxidation: Kinetics and oxygen diffusion through the intermediate layer," *J. Am. Ceram. Soc.*, 101 (2018), pp. 2638-2652
- [26] C. Gasparrini, R. Podor, D. Horlait, R. Chater, and W. E. Lee, "Zirconium Carbide Oxidation: Maltese Cross Formation and Interface Characterization," *Oxid. Met.*, 88 (2017), pp. 509–519
- [27] G. A. Rama Rao and V. Venugopal, "Kinetics and mechanism of the oxidation of ZrC," *J. Alloys Compd.*, 206 (1994), pp. 237-242
- [28] D. Gozzi, M. Montozzi, and P. L. Cignini, "Oxidation kinetics of refractory carbides at low oxygen partial pressures," *Solid State Ionics*, 123 (1999), pp. 11-18
- [29] A. Bellucci, D. Gozzi, T. Kimura, T. Noda, and S. Otani, "Zirconia growth on zirconium carbide single crystals by oxidation," *Surf. Coatings Technol.*, 197 (2005), pp. 294–302
- [30] B. Wei, D. Wang, Y. Wang, H. Zhang, S. Peng, C. Xu, G. Song and Yu Zhou., "Corrosion kinetics and mechanisms of ZrC<sub>1-x</sub> ceramics in high temperature water vapor," *RSC Adv.* 8 (2018), pp. 18163-74
- [31] G. Gutierrez, N. Toulhoat, N. Moncoffre, Y. Pipon, N. Djourellov, A. Maître, M. Gendre, P. Nedelec, "High temperature annealing of Xe implanted ZrC<sub>0.95</sub>O<sub>0.05</sub> investigated by RBS, TEM and PAS-DBS," *Prog. Nucl. Energ.*, 57 (2012), pp. 57-61
- [32] X. Iltis, F. Lefebvre, and C. Lemaignan, "Microstructural study of oxide layers formed on Zircaloy-4 in autoclave and in reactor Part i: Impact of irradiation on the microstructure of the zirconia layer," *J. Nucl. Mater.*, 224 (1995), pp. 109-120
- [33] A. Garner, F. Baxter, P. Frankel, M. Topping, A. Harte, T. Slater, P. Tejlund, J. Romero, E. Darby, A. Cole-Baker, M. Gass, M. Preuss, "Investigating the Effect of Zirconium Oxide Microstructure on Corrosion Performance: A Comparison between Neutron, Proton, and Nonirradiated Oxides," in *Zirconium in the Nuclear Industry: 18<sup>th</sup> International Symposium*, ASTM STP1597, R. J. Comstock and A. T. Motta, Eds., ASTM International, West Conshohocken, PA, 2018, pp. 491–523



- [34] Y. Zhang, M. L. Crespillo, H. Xue, K. Jin, C. H. Chen, C. L. Fontana, J. T. Graham, W. J. Weber, "New ion beam materials laboratory for materials modification and irradiation effects research," *Nucl. Instruments Methods Phys. Res. Sect. B Beam Interact. with Mater. Atoms*, 338 (2014), pp. 19-30
- [35] M. L. Crespillo, J. T. Graham, Y. Zhang, and W. J. Weber, "In-situ luminescence monitoring of ion-induced damage evolution in SiO<sub>2</sub> and Al<sub>2</sub>O<sub>3</sub>," *J. Lumin.*, 172 (2016), pp. 208-218
- [36] M. L. Crespillo, J. T. Graham, Y. Zhang, and W. J. Weber, "Temperature measurements during high flux ion beam irradiations," *Rev. Sci. Instrum.*, 87 (2016), pp. 024902
- [37] J. F. Ziegler, M. D. Ziegler, and J. P. Biersack, "SRIM - The stopping and range of ions in matter (2010)," *Nucl. Instruments Methods Phys. Res. Sect. B Beam Interact. with Mater. Atoms*, 268 (2010), pp. 1818-1823
- [38] M. J. Zheng, I. Szlufarska, and D. Morgan, "Ab initio prediction of threshold displacement energies in ZrC," *J. Nucl. Mater.*, 471 (2016), pp. 214–219
- [39] R. E. Stoller, M. B. Toloczko, G. S. Was, A. G. Certain, S. Dwaraknath, and F. A. Garner, "On the use of SRIM for computing radiation damage exposure," *Nucl. Instruments Methods Phys. Res. Sect. B Beam Interact. with Mater. Atoms*, 310 (2013), pp. 75–80
- [40] Y. Zhang, M. A. Tunes, M. L. Crespillo, F. Zhang, W. L. Boldman, P. D. Rack, L. Jiang, C. Xu, G. Greaves, S. E. Donnelly, "Thermal stability and irradiation response of nanocrystalline CoCrCuFeNi high-entropy alloy," *Nanotechnology*, 30 (2019), pp. 294004
- [41] G. S. Was, *Fundamentals of radiation materials science: Metals and alloys*, second edition. 2016.
- [42] S. J. Zinkle and G. S. Was, "Materials challenges in nuclear energy," *Acta Mater.*, 61 (2013), pp. 735-758
- [43] ASTM, "ASTM C373-14 Standard Test Method for Water Absorption, Bulk Density, Apparent Porosity, and Apparent Specific Gravity of Fired Whiteware Products," *Astm C373-88*, 1999
- [44] F. Réjasse, O. Rapaud, G. Trolliard, O. Masson, and A. Maître, "Experimental investigation and thermodynamic evaluation of the C–O–Zr ternary system," *RSC Adv.*, 100 (2016) pp. 100122-35

- [45] M. L. Jenkins and M. A. Kirk, *Characterization of Radiation Damage by Transmission Electron Microscopy*, Series in Microscopy in Materials Science, Institute of Physics Publishing (2001)
- [46] H. L. Brey and H. G. Olson, "The Fort St. Vrain high temperature gas-cooled reactor. II. Helium circulators," *Nucl. Eng. Des.*, 53 (1979), pp. 125-131
- [47] R. Bès, S. Gavarini, N. Millard-Pinard, S. Cardinal, A. Perrat-Mabilon, C. Peaucelle, T. Douillard, "Influence of crystallographic orientation on the early stages of oxidation of polycrystalline titanium nitride," *J. Nucl. Mater.*, 427 (2012), pp. 415-417
- [48] S. Gavarini, R. Bes, N. Millard-Pinard, S. Cardinal, C. Peaucelle, A. Perrat-Mabilon, V. Garnier, and C. Gaillard, "A comparative study of TiN and TiC: Oxidation resistance and retention of xenon at high temperature and under degraded vacuum," *J. Appl. Phys.*, 109 (2011), pp. 014906
- [49] J. Baillet, S. Gavarini, N. Millard-Pinard, V. Garnier, C. Peaucelle, X. Jaurand, S. Cardinal, A. Duranti, C. Bernard, R. Rapegno, L. Dernoncourt, T. De Echave, "Influence of grain size and microstructure on oxidation rate and mechanism in sintered titanium carbide under high temperature and low oxygen partial pressure," *J. Eur. Ceram. Soc.*, 36 (2016), pp. 3099-3111
- [50] R. V. Zucker, G. H. Kim, W. Craig Carter, and C. V. Thompson, "A model for solid-state dewetting of a fully-faceted thin film," *Comptes Rendus Physique*.14 (2013), pp. 564-577
- [51] R. Lo Savio, L. Repetto, P. Guida, E. Angeli, G. Firpo, A. Volpe, V. Lerardi, U. Valbusa , "Control of the micrometric scale morphology of silicon nanowires through ion irradiation-induced metal dewetting," *Solid State Commun.*, 240 (2016), pp. 41-45
- [52] L. Luo, Y. Kang, J. C. Yang, and G. Zhou, "Nucleation and growth of oxide islands during the initial-stage oxidation of (100)Cu-Pt alloys," *J. Appl. Phys.*, 117 (2015), pp. 065305
- [53] G. Zhou and J. C. Yang, " Formation of Quasi-One-Dimensional Cu<sub>2</sub>O Structures by in situ Oxidation of Cu(100) ," *Phys. Rev. Lett.*, 89 (2002), pp. 106101
- [54] G. Zhou and J. C. Yang, "Initial oxidation kinetics of Cu(100), (110), and (111) thin films investigated by in situ ultra-high-vacuum transmission electron microscopy," *J. Mater. Res.*, 20 (2005), pp. 1684-1694
- [55] G. Zhou, "Nucleation thermodynamics of oxide during metal oxidation," *Appl. Phys. Lett.*, 94 (2009), pp. 201905

- [56] W. Ma, F. W. Herbert, S. D. Senanayake, and B. Yildiz, "Non-equilibrium oxidation states of zirconium during early stages of metal oxidation," *Appl. Phys. Lett.*, 106 (2005), pp. 101603
- [57] S. Shimada, "A thermoanalytical study on the oxidation of ZrC and HfC powders with formation of carbon," *Solid State Ionics*, 149 (2002), pp. 319-326
- [58] R. C. Garvie, "The occurrence of metastable tetragonal zirconia as a crystallite size effect," *J. Phys. Chem.*, 69 (1965), pp. 1238-1243
- [59] Y. Kanno, "Stability of metastable tetragonal ZrO<sub>2</sub> in compound powders and nucleation arguments," *J. Mater. Sci.*, 25 (1990), pp. 1987–1990
- [60] S. Shukla and S. Seal, "Mechanisms of room temperature metastable tetragonal phase stabilisation in zirconia," *Int. Mater. Rev.*, 50 (2005), pp. 45-64
- [61] T. Mitsuhashi, M. Ichihara, and U. Tatsuke, "Characterization and Stabilization of Metastable Tetragonal ZrO<sub>2</sub>," *J. Am. Ceram. Soc.*, 57 (1974), pp. 97-101
- [62] J. M. Costantini, F. Beuneu, and W. J. Weber, "Radiation damage in cubic-stabilized zirconia," *J. Nucl. Mater.*, 440 (2013), pp. 508-514
- [63] K. E. Sickafus, H. J. Matzke, Th. Hartmann, K. Yasuda, J. A. Valdez, P. Chodak III, R. A. Verrall, "Radiation damage effects in zirconia," *J. Nucl. Mater.*, 274 (1999), pp. 66-77
- [64] D. S. Aidhy, Y. Zhang, and W. J. Weber, "Radiation damage in cubic ZrO<sub>2</sub> and yttria-stabilized zirconia from molecular dynamics simulations," *Scr. Mater.*, 98 (2015), pp. 16-19
- [65] E. Zarkadoula, R. Devanathan, W. J. Weber, M. A. Seaton, I. T. Todorov, K. Nordlund, M. T. Dove, and K. Trachenko, "High-energy radiation damage in zirconia: Modeling results," *J. Appl. Phys.*, 115 (2014), pp. 083507
- [66] P. Krasnochtchekov, R. S. Averback, and P. Bellon, "Precipitate stability and morphology in irradiation environments," *JOM*, 59 (2007), pp 46–50
- [67] Allen T.R., Was G.S. (2007) Radiation-enhanced diffusion and radiation-induced segregation. In: Sickafus K.E., Kotomin E.A., Uberuaga B.P. (eds) *Radiation Effects in Solids*. NATO Science Series, vol 235. Springer, Dordrecht
- [68] W. Hu, J. Xiang, S. Liu, Y. Zhang, C. Chen, P. Wang, H. Wang, B. Xu, J. He, D. Yu, Y. Tian, Z. Liu "Low-temperature diffusion of oxygen through ordered carbon vacancies in Zr<sub>2</sub>C<sub>x</sub>: the formation of ordered Zr<sub>2</sub>C<sub>x</sub>O<sub>y</sub>," *Inorg. Chem.*, 51 (2012), pp. 5164-5172

- [69] M. Schuhmacher and P. Eveno, "Oxygen diffusion in titanium carbide," *Solid State Ionics*, 12 (1984), pp. 263-270
- [70] J. Baillet, S. Gavarini, N. Millard, Pinard, V. Garnier, C. Peaucelle X. Jaurand, A. Duranti, C. Bernard, R. Rapegno, S. Cardinal, L. Escobar Sawa, T. De Echave, B. Lanfant, Y. Leconte, "Surface damage on polycrystalline  $\beta$ -SiC by xenon ion irradiation at high fluence," *J. Nucl. Mater.*, 503 (2018), pp. 140-150
- [71] U. Brossmann, R. Würschum, U. Södervall, and H. E. Schaefer, "Oxygen diffusion in ultrafine grained monoclinic  $\text{ZrO}_2$ ," *J. Appl. Phys.*, 85 (1999), pp. 7646
- [72] P. D. Edmondson, Y. Zhang, F. Namavar, C. M. Wang, Z. Zhu, and W. J. Weber, "Defect- and strain-enhanced cavity formation and Au precipitation at nano-crystalline  $\text{ZrO}_2/\text{SiO}_2/\text{Si}$  interfaces," *Nucl. Instruments Methods Phys. Res. Sect. B Beam Interact. with Mater. Atoms*, 269 (2011), pp. 126-132

### III. SEQUENTIAL ION-ELECTRON IRRADIATION OF ZIRCONIUM CARBIDE CERAMICS: MICROSTRUCTURAL ANALYSIS

Raul Florez<sup>a</sup>, Xiaoqing He<sup>b,c</sup>, Tommi A. White<sup>c,d</sup>, Miguel L. Crespillo<sup>e</sup>, Gregory Hilmas<sup>f</sup>, William Fahrenholtz<sup>f</sup>, Joseph Graham<sup>a,f\*</sup>

<sup>a</sup>. Nuclear Engineering Program, Missouri University of Science and Technology, 65409 Rolla, MO, United States

<sup>b</sup>. Electron Microscopy Core, University of Missouri, 65211 Columbia, MO, United States

<sup>c</sup>. Department of Mechanical and Aerospace Engineering, University of Missouri, 65211 Columbia, MO, United States

<sup>d</sup>. Department of Biochemistry, University of Missouri, 65211, Columbia, MO, United States

<sup>e</sup>. Department of Material Science and Engineering, University of Tennessee, 37996 Knoxville, TN, United States

<sup>f</sup>. Department of Materials Science and Engineering, Missouri University of Science and Technology, 65409 Rolla, MO, United States

#### ABSTRACT

Zirconium Carbide ( $\text{ZrC}_x$ ) was irradiated with 10 MeV  $\text{Au}^{3+}$  ions to a dose of 10 displacements per atoms (dpa) and subsequently with 300 keV electrons in a transmission electron microscope (TEM). After ion irradiation, dislocation loops were observed in the microstructure and an increase in the number of carbon vacancies was revealed by Raman spectroscopy. Grazing incidence X-ray diffraction (GIXRD) analysis showed that neither amorphization nor oxidation occurred during ion irradiation of the specimen. Subsequent electron irradiation of the pre-implanted  $\text{ZrC}_x$  foil led to formation of nanosized tetragonal

ZrO<sub>2</sub> precipitates (5-10 nm diameter) on the surface of the TEM lamella. The formation of the new oxide phase was not related to the electron beam-induced heating of the specimen or ionization of residual oxygen in the TEM chamber, but to knock-on displacements that facilitated transport of oxygen atoms across the ion implanted layer. These results suggest that high-energy electron irradiation of pre-damaged ZrC<sub>x</sub> foils induced atomic mixing via radiation enhanced diffusion (RED), producing surface oxidation of the TEM foil. This research provides new knowledge of the microstructural response of ZrC<sub>x</sub> to different types of radiation and new insights into the inadvertent effects of electron beam during TEM analysis of *in-situ* and *ex-situ* ion irradiated ZrC<sub>x</sub>.

**Keywords: ZrC, Ion Irradiation, Electron Irradiation, Oxidation**

\* Corresponding Author

Email: grahamjose@mst.edu

## 1. INTRODUCTION

Zirconium Carbide (ZrC<sub>x</sub>) has gained interest as a candidate material for a variety of applications in advanced nuclear energy systems due to its excellent physical and chemical properties including high melting point [1] , high thermal and electrical conductivities [2], outstanding resistance to fission product attack [3], good mechanical strength [1], and low neutron absorption cross-section [4]. This unusual combination of properties makes ZrC<sub>x</sub> a strong contender for applications such as fission-product barrier in microencapsulated fuels , cladding in accident tolerant fuels (ATFs) [5], inert fuel

matrix in Gen-IV fast nuclear reactors [6], and plasma facing material (PFM) in fusion reactors [7]. In nuclear reactor systems,  $\text{ZrC}_x$  will be exposed to different types of radiation fields (gamma, neutron, ion and beta particles), which can change the microstructure of  $\text{ZrC}_x$  during reactor operation. The microstructural changes induced by radiation damage affect the properties of  $\text{ZrC}_x$  and its performance in the nuclear reactor. This could eventually impact the safety of the reactor under operation and accident conditions. Consequently, it is crucial to understand the behavior of  $\text{ZrC}_x$  under irradiation conditions for its successful implementation in the next generation of nuclear energy systems.

Numerous studies have been conducted to investigate the effects of irradiation on  $\text{ZrC}_x$  [8-14]. Most of the previous work has aimed to identify and quantify the microstructural defects in ion irradiated specimens as a function of the ion type, dose, temperature, and stoichiometry. The current damage mechanism map indicates that the radiation response of  $\text{ZrC}_x$  at temperatures relevant to the operation of nuclear reactors (20–1073 K) is driven by interstitial clustering [11]. This has been confirmed by transmission electron microscopy (TEM) analysis of irradiated samples, showing the progressive evolution from “black-dot” defects, to dislocation loops, to entangled dislocation networks with increasing irradiation dose [8], [9]. In addition to the microstructural defects, a secondary oxide phase is usually found during TEM analysis of irradiated  $\text{ZrC}_x$ . The oxide phase appears as nanosized precipitates, which are distributed across the surface of the TEM lamella. Gan *et al.* [15] were the first ones to report the formation of the new phase in  $\text{ZrC}$  irradiated with 1 MeV  $\text{Kr}^{2+}$  ions at the Intermediate Voltage Electron Microscope (IVEM) facility. They observed diffraction rings in the

selected area electron diffraction (SAED) patterns for samples irradiated at 300 K and 1073 K. The authors concluded that the diffraction rings were produced by nanosized precipitates having face centered cubic (FCC) symmetry with a lattice parameter of 0.506 nm (~8% larger than ZrC). Gosset *et al.* [9], [10] also reported the formation of a secondary phase after irradiation of ZrC with 4 MeV Au<sup>3+</sup> ions at room temperature (RT). Based on the indexing of the diffraction rings, the secondary phase was identified as tetragonal ZrO<sub>2</sub> (a=3.61 Å and c=5.19 Å). Additionally, dark field images acquired with part of the most intense diffraction ring revealed a high density of nanometric precipitates located at the surface of the specimen. Recently, Ulmer *et al.* [16] also found that oxide nanoprecipitates were formed during *in-situ* irradiation of ZrC with 1 MeV Kr<sup>2+</sup> ions at temperatures within 20-1073 K. The indexing of the rings was consistent with a 0.506 nm lattice parameter FCC structure, which is close to that of cubic ZrO<sub>2</sub>. Interestingly, Ulmer also noted that the diffraction rings appeared in samples irradiated at all temperatures, except 300 K and 473 K. This result contradicts Gan's work that found oxide precipitates in samples irradiated at 300 K. The discrepancy is surprising considering that both authors conducted the irradiations experiments under similar conditions (1 MeV Kr<sup>2+</sup> at 300 K at the IVEM facility).

Although the formation of oxide precipitates seems to be one of the most prominent radiation effects in ion irradiated ZrC<sub>x</sub>, the mechanism underlying their formation is not fully understood. Given the high thermodynamic driving force for oxidation of ZrC<sub>x</sub> [17], Gosset *et al.* [9] suggested that the precipitates were formed by radiation-enhanced oxidation during ion implantation of ZrC foils. However, the experimental evidence supporting this hypothesis is still inconclusive. For example, if



radiation-enhanced oxidation was the prevalent mechanism of oxide formation, a systematic variation in the intensity of the diffraction rings would occur as the irradiation dose increased. Yet, no systematic changes in the selected area electron diffraction (SAED) patterns were observed for ZrC specimens irradiated with Kr-ions at different doses [15], [16]. Furthermore, the hypothesis of radiation-enhanced oxidation also fails to explain why oxide precipitates were formed in samples irradiated at cryogenic temperatures, but not in those irradiated at RT [16]. This result is unexpected considering that the diffusion of atoms and defects is significantly lower at cryogenic temperatures than at RT. Another aspect of the oxidation process that needs further explanation is that crystalline oxide nanoprecipitates formed only during in-situ for ion irradiated ZrC specimens. For bulk sample irradiation, the studies showed that thin oxide layers formed in ZrC after irradiation. The oxide layer was amorphous in specimens irradiated at RT [18] and crystalline in those irradiated at a high temperature (1073 K) [19]. These observations lead to the question: Why does the oxidation behavior differ between samples irradiated *ex-situ* and *in-situ*, if the mechanism driving the transformation is the same?. The absence of systematic changes of the SAED patterns in stand-alone studies and the inconsistencies that arise when comparing the results from different research groups, suggest that extrinsic factors might play a role in the formation of the oxide precipitates during in-situ ion-irradiation of ZrC.

A major difference between *in-situ* and *ex-situ* ion irradiations is that energetic electrons are simultaneously used during *in-situ* ion irradiations. The concurrent use of electrons during ion irradiation can produce unintended effects, which could potentially modify the microstructure of the material being investigated [21]. Previous work on

transition metal carbides indicated that prolonged exposure to energetic electrons in the TEM can produce elemental segregation through the foil. Thus, it is possible that the electrons used for imaging during *in-situ* ion irradiations can also be involved in the formation of  $\text{ZrO}_2$  nanoprecipitates on ion implanted ZrC specimens. Therefore, the goal of this study was to investigate the effects of electron irradiation during TEM examination of an ion- irradiated ZrC foil to study possible segregation effects. Direct evidence is provided that e-beam exposure produces surface oxidation of ion irradiated ZrC foil leading to possible reaction schemes.

## 2. MATERIALS AND METHODS

### 2.1. SAMPLE PREPARATION

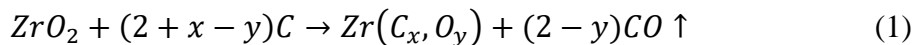
The following section describe the methodology used for the preparation of the specimens used in this work.

**2.1.1. Synthesis of  $\text{ZrO}_2$  precursor.** High purity  $\text{ZrO}_2$  powders with low Hf content were synthesized by a precipitation method using  $\text{ZrCl}_4$  powder (Reactor grade, >99.5% metal basis, Alfa Aesar) and  $\text{NH}_4\text{OH}$  (28 wt%, Alfa Aesar) as starting materials. Precipitation was induced by dropwise addition of 28 wt%  $\text{NH}_4\text{OH}$  to 0.4 M  $\text{ZrCl}_4$  solution until the pH reached 10. After aging for 30 minutes under strong stirring with a magnetic stir bar, the precipitate was filtered and washed with an excess of deionized water to remove chloride ions. The hydrous cake was then dried at 120 °C overnight. Afterwards, the powder was calcined in a convection oven at 700 °C for 4 hours to

produce ZrO<sub>2</sub>. The obtained powder was lightly ground with a mortar and pestle and passed through a 60 mesh sieve.

**2.1.2. Synthesis of ZrC powder.** The synthesized ZrO<sub>2</sub> and carbon black (BP-1100, Cabot Corporation, Alpharetta, GA, USA) were batched with a molar ratio of ZrO<sub>2</sub>:C=1:3 based on the stoichiometry of Reaction 1 and then ball-milled using zirconia milling media and acetone for 24 hours. Afterwards, the slurry was dried by rotary evaporation (Rotavapor R-124; Buchi, Flawil, Germany) at a temperature of 80° C, under low vacuum (~27 kPa), and a rotation speed of 120 rpm. The dried powder was passed through a 50-mesh sieve and pelletized by uniaxial pressing before carbothermal reduction.

Solid state carbothermal reduction was conducted in a graphite element furnace (3060-FP20, Thermal Technology, Santa Rosa, CA, USA) under vacuum conditions. The mixed powder was heated from room temperature to 1800° C at a heating rate of 10°C/min, and dwell time of 6 hours.



**2.1.3. Densification.** A billet of ZrC was prepared by hot-pressing the synthesized ZrC powder in a 25.4 mm cylindrical graphite die lined with BN-coated (SP-180 Cerac, Milwaukee, WI) graphite foil (2010-A; Mineral Seal Corp, Tucson, Arizona). The powder was loaded into the die and cold compacted in a uniaxial press at ~2MPa. The powder was then heated under vacuum to 1600 °C with an average heating rate of 20 °C/min. At that time, the furnace was backfilled with helium and a uniaxial pressure of 32 MPa was applied. The furnace was then heated at 50 °C/min to 2200 °C. After 90 min at 2200°C,

the furnace was cooled at  $\sim 50$  °C/min. The load was removed when the die temperature dropped below 1600 °C.

Following densification, the specimens for microscopy and ion irradiations were cut parallel to the hot pressing direction with a slow-speed diamond saw. The surface of the ZrC foils were then polished to a 0.25  $\mu\text{m}$  mirror-finish using successively finer diamond abrasives. After polishing, the specimens were ultrasonically cleaned with ethanol for 15 min at room temperature.

## 2.2. ION IMPLANTATION

A rectangular ZrC foil (12 x 4 mm) was irradiated in the Ion Beam Materials Laboratory (IBML UT-ORNL) at the University of Tennessee, Knoxville [20] with 10 MeV  $\text{Au}^{3+}$  ions at room temperature using a 3.0 MV tandem accelerator. The central region of the ZrC foil (7x4 mm) was irradiated to a dose of 10 dpa. The ion beam was defocused and rastered in the horizontal and vertical directions with the aim of producing a region that was homogeneously irradiated. Beam homogeneity was verified by ion-induced luminescence from quartz targets and was found to be within 10% throughout the irradiated area [21]. The ion flux was set at  $7 \times 10^{11} \text{ cm}^{-2} \text{ s}^{-1}$ . Low beam current densities in the range of 5 nA  $\text{mm}^{-2}$  were used to reduce any undesired effects or charge accumulation on the samples [22]. The vacuum chamber pressure was below  $10^{-7}$  torr during ion irradiation. The Stopping and Range of Ions in Matter binary collision approximation (BCA) code 2013 version (SRIM-2013) [23] was used to estimate the displacement damage depth profile. Cascades were performed in quick-cascade mode (simple Kinchin and Pease model) assuming a density of 6.71  $\text{g/cm}^3$  for ZrC and

threshold displacement energies of 37 eV for Zr and 16 eV for C [24]. To compare ion and neutron irradiation results, the use of the quick Kinchin–Pease option in SRIM to compute radiation damage exposure has been recommended within the nuclear community [25]. The damage profile estimated from SRIM is determined by the sum of the predicted vacancy concentrations (using 'Knock-Ons' from Au ions and 'Vacancies' from target elements of Zr and C, together with the replacement collisions [26].

Assuming a bulk ZrC sample, the predicted damage profile in displacements per atom (dpa) and the implanted Au ion profile are shown in Figure 1. The peak dose under 10 MeV Au irradiation is located around 1000 nm. The conversion factor from ion fluence ( $10^{14} \text{ cm}^{-2}$ ) to local dose in the ZrC foil under quick simulation was 0.8343 dpa.

Irradiations were performed with Au ions because of their relatively inert nature and large nuclear stopping cross section, which enables a high damage rate per incident ion while minimizing artifacts induced by the injected ions. The beam energy of 10 MeV was chosen to obtain a relatively flat profile to a depth of 1  $\mu\text{m}$  without appreciable effects of implanted Au ions (Figure 1). Moreover, intermediate energy heavy ion irradiations produce a displacement cascade density and morphology more similar to fission neutrons than irradiation using light ions, which produces a more sparse sub-cascade morphology [27].

### **2.3. MATERIAL CHARACTERIZATION**

The following subsections presents detailed information about the experimental techniques that were used to investigate the specimens.

**2.3.1. Density and Chemical Analysis.** The bulk density of the hot-pressed billet was measured by the Archimedes' method performed according to ASTM C73 using distilled water as the immersing medium, [28]. The relative density was calculated by dividing the Archimedes' density by the estimated theoretical density of ZrC ( $\rho=6.71 \text{ g/cm}^3$ ). Chemical analyses for carbon, oxygen and nitrogen content were conducted by the direct combustion method using infrared absorption detection. Carbon (CS600; Leco, St. Joseph, MI), oxygen and nitrogen (TC500; Leco, St. Joseph, MI) contents were measured by grinding part of the dense specimen to ~200 mesh. Three measurements were conducted for each element to establish repeatability.

**2.3.2. Grazing Incidence X-Ray Diffraction (GIXRD).** Grazing incidence X-ray diffraction measurements were performed to evaluate structural modifications in the near surface region following ion irradiation. GIXRD profiles were collected on a PANalytical X'Pert Pro Multipurpose Diffractometer (MPD) fitted with a Cu X-ray tube and an X'Celerator detector. Diffraction patterns were acquired in grazing incidence geometry over the  $2\theta$  range  $25\text{-}90^\circ$  with a step size of  $0.03^\circ$  and counting time of 0.5 s at each step. The scans were recorded at several incident angles between  $0.5^\circ$  and  $5^\circ$  in order to probe microstructural changes at different mean penetration depths from 0.6 to  $1.5 \mu\text{m}$ . X-ray tube operation conditions were 40 kV and 40 mA.

**2.3.3. Raman Spectroscopy.** Raman measurements were collected using a HORIBA Jobin Yvon LabRAM ARAMIS microRaman spectrometer (Horiba, Edison, NJ). The specimens were excited by a 632 nm He/Ne laser focused to a spot 2-3  $\mu\text{m}$  in size on the sample using a 50x microscope objective lens. Raman spectra were acquired in the backscattering geometry. The laser power was below 2 mW to prevent local

heating of the sample. Five spectra were taken from each specimen, with all measurements conducted at room temperature.

**2.3.4. Electron Microscopy.** A TEM lamella specimen was lifted out from the center of the ion irradiated ZrC sample and mounted onto a copper Omniprobe TEM grid. The TEM sample was prepared in a dual Focused Ion Beam-Scanning Electron Microscope (FIB-SEM Scios<sup>TM</sup> DualBeam<sup>TM</sup>, FEI, Hillsboro, Oregon). A 15  $\mu\text{m}$  (width)  $\times$  10  $\mu\text{m}$  (depth) rectangular lamella was then further thinned to electron transparency by the FIB ( $\sim 50$  nm). The TEM lamella was investigated using a FEI Tecnai TF30-FEG STwin STEM working at 300 kV. Bright field (BF) micrographs were acquired to characterize the microstructure of the pristine and ion irradiated areas of the specimen. In addition, energy dispersive X-ray spectroscopy (EDX) and electron energy loss spectroscopy (EELS) were used to characterize the element composition of the ion implanted layer. For the electron irradiation experiments, the beam was stabilized at 9.5 A/cm<sup>2</sup> and the column pressure remained at  $1.18 \times 10^{-5}$  Pa ( $8.9 \times 10^{-8}$  torr). A beam illumination area of 1.25  $\mu\text{m}$  in diameter was used for e-beam irradiations. SAED patterns were collected at various times to investigate the microstructural evolution during electron irradiations. Centered dark field images were also captured using a portion of the ring structure visible in the SAED patterns for the diffracted beam.

### 3. RESULTS

#### 3.1. DENSITY AND CHEMICAL ANALYSIS

The as-sintered ZrC pellet had a relative density of 95%. The carbon, oxygen and nitrogen contents were 11.53, 0.821, and 0.0251 wt %, respectively.

#### 3.2. GRAZING INCIDENCE X-RAY DIFFRACTION

Figure 2a) shows survey GIXRD patterns obtained from the as-sintered ZrC specimen. The patterns were acquired at  $\omega$  values of 0.5, 1, 1.5, 3 and 5° to probe microstructural changes from a layer on the surface of the specimen that was  $\sim 2.0 \mu\text{m}$  thick. This thickness was selected because it corresponded to the range of the 10 MeV  $\text{Au}^{3+}$  ions used in this work (see Figure 1). At all  $\omega$  values,  $\text{ZrC}_x$  with  $Fm\bar{3}m$  crystal structure (JCPDF card 35-0784) was the only phase detected and no extra peaks were apparent.

GIXRD patterns were also acquired from the irradiated specimens as shown in Figure 2b. No new peaks were observed in any of the diffraction patterns. The irradiated specimen only exhibited the expected peaks for ZrC at all  $\omega$  values. Consequently, extensive formation of  $\text{ZrO}_2$  did not occur during heavy ion irradiation of ZrC. Peak broadening and a decrease in the peak intensity were observed upon ion irradiation. These concurrent changes were indicative of structural distortion and heterogeneous microstrain produced by the radiation induced defects. No significant peak shifts were observed before and after irradiation, indicating low volumetric swelling of the ion irradiated ZrC.



### 3.3. RAMAN SPECTROSCOPY

To further investigate any structural inhomogeneities in the pristine and irradiated ZrC specimens, Raman spectra were collected (Figure 3). The spectrum of the unirradiated specimen (Figure 3a) indicated the presence of four faint peaks in the 100-1000  $\text{cm}^{-1}$  range, denoted by A1 (204  $\text{cm}^{-1}$ ), A2 (275  $\text{cm}^{-1}$ ), O1 (515  $\text{cm}^{-1}$ ), and O2 (600  $\text{cm}^{-1}$ ). Those peaks were attributed to the acoustic and optical phonon lines of  $\text{ZrC}_{1-x}$  [29], indicating symmetry breakdown. These phonon modes are forbidden in stoichiometric ZrC and only appear when carbon vacancies are present. The low intensity Raman peaks suggested that the as-sintered ZrC billet was slightly sub-stoichiometric before ion irradiation. Additionally, no Raman peaks attributed to  $\text{ZrO}_2$  polymorphs were observed for the unirradiated specimen.

Upon heavy-ion irradiation, the four main peaks due to acoustical and optical phonons were observed in the Raman spectrum. Compared to the virgin specimen, the intensity and width of the defect-induced bands increased significantly in the ion-irradiated specimen implying an increase in the number of carbon vacancies after irradiation [30]. No clear peak shifting was observed in the  $\text{ZrC}_{1-x}$  Raman bands upon irradiation. The absence of  $\text{ZrO}_2$  Raman peaks in the ion-irradiated spectrum suggested that the oxidation of ZrC did not occur during heavy ion irradiation.

### 3.4. TEM ANALYSIS

TEM analysis was conducted on the ion irradiated specimen to determine the microstructural changes induced by irradiation. Figure 4a shows a bright field image for the specimen irradiated to a dose of 10 dpa at RT. Dislocation loops smaller than  $<8$  nm were visible in the irradiated microstructure. Similar defects had also been found in gold-irradiated

ZrC<sub>x</sub> to fluences above  $10^{15} \text{ cm}^{-2}$  [9],[16]. After irradiation to 10 dpa at RT, SAED showed that the  $Fm\bar{3}m$  crystal structure of ZrC<sub>x</sub> remained unchanged (Figure 5a), corroborating the high radiation-induced- amorphization (RIA) resistance of this material. Aside from ZrC, no distinguishable diffraction signals of nanocrystalline ZrO<sub>2</sub> or other secondary phases were apparent in the SAED pattern acquired immediately after focusing the electron beam in the ion-irradiated area. However, diffuse rings started to appear in SAED patterns when the analyzed area was continuously exposed to the electron beam. This indicated that microstructural modifications occurred in the analyzed specimen during TEM examination.

**3.4.1. Electron Beam Irradiations.** The effect of the electron irradiation beam in irradiated and unirradiated ZrC grains is discussed next.

**3.4.1.1. Ion irradiated ZrC grain.** To further evaluate the effects of the e-beam on the TEM specimen, *in situ* electron irradiation experiments were conducted over different areas of the irradiated sample. Figure 5 shows a sequence of SAED patterns acquired at selected times during the electron irradiation of a ZrC grain implanted with 10 MeV Au<sup>3+</sup> ions. The area selected for this experiment was located about 1  $\mu\text{m}$  from the top surface and far away from grain boundaries where defect-denuded zones are usually observed. The first diffraction pattern (Figure 5a) was obtained immediately after focusing the electron beam in the ion-irradiated area and was comprised only of ZrC diffraction spots. No extra diffraction rings or spots were apparent in the SAED pattern at the beginning of the e-beam irradiation. After 30 minutes of exposure to the electron beam, weak diffraction rings were observed in the SAED pattern as illustrated in Figure 5b. Increased beam time resulted in a sharpening of the diffraction rings (Figure 5c). From their relative radii, the diffraction rings did not correspond to interplanar distances of the initial ZrC

cubic phase. Examination of the powder diffraction file database showed that the interplanar distances matched well with tetragonal zirconia ( $t\text{-ZrO}_2$ , space group  $P4_2/nmc$ , tetragonal crystal system with lattice parameters  $a=3.6 \text{ \AA}$  and  $b=5.19 \text{ \AA}$ ) according to the card PDF 050 1089. HRTEM and the corresponding Fast Fourier Transform (FFT) images acquired from the electron irradiated area (Figure 6), further confirmed the existence of  $t\text{-ZrO}_2$ . The FFT pattern corresponding to the electron irradiated area (Figure 6b) showed incomplete rings of dots that were indicative of nanocrystalline  $t\text{-ZrO}_2$ . The discretization of the diffraction rings suggested that the nanoprecipitates were formed by homogeneous nucleation and were randomly oriented with respect to the  $\text{ZrC}$  matrix. The oxide crystallite analyzed is indicated by the red box in Figure 6a. The acquired FFT pattern (Figure 6c) matched well with the simulated diffraction pattern of  $t\text{-ZrO}_2$ .

In order to investigate the distribution of the  $t\text{-ZrO}_2$  precipitates in the specimen, dark field (DF) images were acquired on the e-beam irradiated area. Figure 5d shows a DF micrograph taken from a selected part of the diffraction ring as indicated by the circled zone in the inset diffraction pattern. A high density of bright precipitates distributed throughout the  $\text{ZrC}$  matrix could be observed upon e-beam irradiation. The  $t\text{-ZrO}_2$  precipitates had equiaxial shapes with equivalent diameters between 5 and 10 nm. Unfortunately, detailed compositional mapping of the nanoprecipitates could not be conducted via STEM/EDX due to the small size of the precipitates ( $< 10 \text{ nm}$ ). However, EDX analysis on the irradiated area revealed the presence of Zr, C and O in the specimen (Figure S1). Evidence of oxygen content was also obtained by EELS analysis (Figure S2), which has a higher sensitivity for light elements.

Further changes were observed in the diffraction pattern after electron-irradiation times of more than 1 hour. Figure 7a shows the SAED pattern obtained after about 100 min of electron irradiation. In addition to the oxide rings detected before, a new intense ring was observed in the DP. The corresponding interplanar distance associated with this new ring was 1.80 Å, which could be indexed to either t-ZrO<sub>2</sub> (001) or graphite (102) planes. The formation of graphite cannot be ruled out considering that e-beam induced decarburization of transition metal carbides (TMCs) had been reported previously. [31]. A dark field image taken using a portion of the most intense diffraction ring, revealed a high density of nanometric precipitates distributed across the e-beam irradiated area (Figure 7b). Finally, to verify the extension of the microstructural changes induced by the electron irradiation, diffraction analysis was conducted in the area immediately adjacent to the e-beam irradiated region. The lack of diffraction rings in the SAED pattern acquired in this area confirmed that the microstructural changes occurred only in the electron irradiated area and did not extend beyond it (Figure 7c).

**3.4.1.2. Unirradiated ZrC grain.** The effects of e-beam irradiation were also investigated in areas of the TEM foil that did not undergo ion-irradiation. In this case, the region selected for e-beam exposure was a ZrC grain located about 5 µm below the ion implantation range of the 10 MeV Au<sup>3+</sup> ions (see SRIM profile in Figure 1). Figure 8a shows a bright field image taken at the [110] zone axis of the unirradiated ZrC grain. Although minor FIB damage was observed in some regions, most of the area looked pristine without any type of dislocation loops. The FIB damage observed in the selected grain appeared as small black dots (<4 nm) and had a low surface density (<10<sup>15</sup> m<sup>-2</sup>). This defect density was considered negligible compared to the defect density observed in

the ion-irradiated region. Figure 8 b), c), and d) show a sequence of SAED patterns acquired at selected times during electron irradiation of the pristine grain. Aside from ZrC, no distinguishable diffraction rings or extra diffraction spots were observed in the SAED patterns as the e-beam irradiation progressed. This result suggested that no secondary phases were formed in pristine grain after the e-beam exposure. Moreover, the lattice parameter of ZrC did not measurably change during e-beam exposure, indicating that minimum radiation damage was introduced in the pristine ZrC grain. Additionally, EELS spectrum acquired on the grain after e-beam exposure showed characteristic peaks for C and Zr; however, no discernible oxygen peak was observed in the spectrum (Figure 8b).

**3.4.2. EELS Analysis.** Possible changes in the local chemical environments of C and Zr atoms induced by irradiation were investigated by EELS spectra obtained in the energy range  $E=270\text{-}370$  eV for three different areas of the FIB cut: 1) virgin ZrC grain, 2) an ion-irradiated ZrC grain, and 3) an ion and electron-irradiated grain (Figure 9). For comparison purposes, each spectrum was normalized by dividing the whole spectrum by the edge intensity at 294 eV as proposed by Jeanne-Rose *et al.* [32]. The carbon K-edge presented a similar fine structure in the different areas. No changes in the onset of the carbon K-edge position, nor in the post-edge shape were seen in the spectra. This observation indicated that the binding energy of C atoms did not vary regardless of irradiation. Previous work by Craven *et al.* [33] reported modifications in the C K-edge shape for electron-irradiated transition metal carbides. These changes in peak shape were attributed to variations in the relative hybridization (i.e., the  $\left(\frac{sp^2}{sp^3}\right)$  ratio) of the C atoms. In the present work, minimal changes were observed in the C K-edge shape for the

examined areas. However, a monochromated EELS (ELNES) analysis with optimized energy resolution could be used to investigate changes in the of C K-edge shape with higher accuracy. As for Zr atoms, the Zr M23-edges position remained unchanged for all analyzed regions. This indicated that the electronic structure of Zr atoms was the same in all areas regardless of irradiation. A closer comparison of the Zr M23-edges for the different spectra showed that the intensity of the M2 peak was increased slightly after e-beam irradiation (Figure 9c). The intensity of the core-level EELS is proportional to the number of the corresponding atoms in the exposed area [34]. Therefore, the increment in the intensity of the M2 peak suggested that Zr enrichment occurred in the ion irradiated area that was continuously exposed to the electron beam. This could be attributed to removal of carbon atoms from the sample leaving behind an increasingly sub-stoichiometric composition in the electron irradiated area. Similar decarburization effects had been previously observed in other transition metal carbides after prolong e-beam exposure in a TEM instrument such as TiC and VC [31], [35].

## 4. DISCUSSION

### 4.1. ION IRRADIATION

The microstructural evolution of ion irradiated  $\text{ZrC}_x$  observed in this work is in good agreement with previous reports. At 10 dpa, dislocation loops were the only type of microstructural defect observed in bright field micrographs (Figure 4), indicating that interstitial clustering drives the radiation response of  $\text{ZrC}_x$  at room temperature. Compositional TEM analysis of the ion irradiated specimen showed that oxygen enrichment occurred in the

ion implanted layer. This is consistent with previous studies that have found evidence of oxygen enrichment in the near surface of ion implanted  $\text{ZrC}_x$  [36]. Despite the local increase in oxygen content, no new oxide phases were formed during ion implantation. At room temperature, the oxygen activity in the vacuum environment in which irradiation was conducted is likely too low for oxidation, but high enough to allow dissolution of oxygen atoms into the defective microstructure. The dissolved oxygen atoms presumably occupy to carbon vacancies that were either generated during ion irradiation or present in the as-prepared ceramic.

#### **4.2. ELECTRON IRRADIATION**

The results presented in Figure 5 indicated that t- $\text{ZrO}_2$  nanocrystals formed during electron beam exposure of the ion-irradiated  $\text{ZrC}$  foil. Interestingly, the oxide nanoprecipitates only formed in pre-damaged areas of the TEM lamella that were continuously exposed to the electron beam. This behavior suggests that both the electron beam and the microstructure of the  $\text{ZrC}_x$  matrix play a role in the formation of the oxide precipitates. To explain the microstructural changes observed in this work, it is necessary to consider the effects of electron-specimen interactions that may drive the oxidation process during electron irradiation. These effects include radiolysis (ionization damage), electron beam heating, and knock-on displacements. Due to the high electrical conductivity of  $\text{ZrC}_x$  ceramics, radiolysis damage is expected to be negligible during electron irradiation. Thus, only electron beam heating and knock-on displacements effects are discussed below.

The inelastic scattering of electrons produces a local temperature increase in the specimen during TEM observations [37]. This temperature rise can facilitate thermally-

activated processes such as diffusion and oxidation reactions. Given its high chemical reactivity with oxygen, thermal oxidation of  $\text{ZrC}_x$  can occur inside the TEM chamber, if the temperature necessary for this process is reached in the microscope. Previous work on thermal oxidation studies of  $\text{ZrC}_x$  in low  $\text{Po}_2$  atmospheres has shown that oxidation begins at  $\sim 300^\circ\text{C}$  [17]. According to Fisher and Jencic's model [38], the maximum temperature rise  $\Delta T$  associated with electron irradiation is given by:

$$\Delta T = \frac{I}{\pi \kappa e} \left( \frac{\Delta E}{d} \right) \ln \left( \frac{b}{r_o} \right) \quad (2)$$

where  $I$  is the beam current,  $\kappa$  is the thermal conductivity of the sample,  $e$  is the electron charge,  $r_o$  is the effective radius of the heat sink,  $b$  is the radius of the TEM sample,  $\Delta E$  is the total energy loss by the electron in a sample of thickness  $d$ . Electron energy loss of  $\text{ZrC}$  is 1.5 eV/nm at 300 keV, which is negligible compared to the initial energy of the incident electrons. As a result,  $\frac{\Delta E}{d}$  is assumed to be constant and given by the stopping power of the incident electrons  $\frac{dE}{dx}$ . In this study, electron irradiations were conducted in both ion-irradiated and pristine  $\text{ZrC}_x$  grains that had very different microstructures (Figure 4 and 8). Since the thermal properties depend on microstructure, different values of thermal conductivity are expected for the ion-irradiated and pristine areas of the  $\text{ZrC}_x$  foil. To calculate the e-beam heating effect for the pristine region, a thermal conductivity value of  $\kappa_{av} = 26 \frac{\text{W}}{\text{mK}}$  was used. This value corresponded to average of the thermal conductivity values reported in the literature for near stoichiometric  $\text{ZrC}$  [39] [40]. Based on this assumption, the maximum temperature increase in the pristine area was estimated to be less than 1 K under the e-beam irradiation conditions used in this work ( $I = 6 \text{ nA}$ ,  $b = 1.5 \text{ mm}$ ,  $r_o = 100 \text{ nm}$ , and  $\frac{dE}{dx} = 1.055 \frac{\text{eV}}{\text{nm}}$ ). On the other hand, a significant



reduction in the thermal conductivity of  $\text{ZrC}_x$  is expected for the ion-implanted area because of the high density of dislocation loops and carbon vacancies present in this region (Figure 3 and 4). Previous studies have reported a reduction of more than 60% in the thermal conductivity for ion irradiated  $\text{ZrC}_x$  [41],[42]. If a similar level of thermal degradation were assumed in this work, then the maximum temperature rise in the ion implanted regions would be  $\sim 3 \text{ K}$ . Consequently, it was concluded that the temperature increment induced by e-beam irradiation is insufficient to produce thermal oxidation of  $\text{ZrC}_x$  under irradiation with 300 keV electrons.

Alternatively, knock-on atomic displacements can also occur during TEM examination with energetic electrons [37]. In this case, atoms might be permanently displaced from their normal lattice positions, if the energy that they receive through elastic collisions surpasses their threshold displacement energy  $E_d$ . According to the elastic collision model, the maximum energy transferred from the electron beam to the target atoms by elastic collisions is given by:

$$E_{max} = \frac{2E(E+2mc^2)}{Mc^2} \quad (3)$$

where  $E$  is the energy of the incident electron,  $m$  is the mass of the electron,  $M$  is the mass of the atom, and  $c$  is the speed of light. Figure 10a) shows the calculated  $E_{max}$  for Zr, C and O atoms over a range of incident electron energies up to 400 keV. Oxygen atoms were included in the displacement calculations because EDX and EELS analyses indicated the presence of oxygen in the ion implanted layer (Figure S1). The horizontal lines 1 and 2 in Figure 10a correspond to the average displacement energy  $E_d$  for the C and Zr sublattice in ZrC determined by *ab-initio* methods [24]. The incident electron beam used in this work had an energy of 300 keV, which could transfer a maximum

energy of 9 eV to Zr atoms and 71 eV to C atoms. Since the threshold displacement energy for Zr atoms is much higher than that received under irradiation with 300 keV electrons, the direct displacement of Zr atoms should not occur in ZrC during TEM examination. On the other hand, the threshold displacement energy for carbon atoms is lower than that transferred by elastic collision with 300 keV electrons. Hence, direct knock-on displacement of carbon atoms is likely to happen when a ZrC foil is analyzed with a 300 keV e-beam.

Concerning the oxygen atoms, no experimental or theoretical values of  $E_d$  for oxygen in zirconium oxycarbides ( $\text{ZrC}_x\text{O}_y$ ) were found in the literature. However, as a reference value, the threshold displacement energy for oxygen in most oxides falls at values around 40 eV [43]. In contrast to most oxides, vacancy-enhanced displacement occurs in transition metal carbides due to the presence of carbon vacancies. This mechanism significantly reduces the threshold displacement energy of carbon atoms because they can be transferred directly into neighboring vacant sites. Since oxygen atoms also occupy carbon vacancy sites, it is reasonable to assume that  $E_d$  for oxygen in zirconium oxycarbides is lower than in oxides ( $< 40$  eV). Thus, oxygen atoms can be also displaced by elastic collision with 300 keV electrons.

The most energetic displaced carbon and oxygen atoms can, in turn, transfer energy to zirconium atoms through cascade collisions. In this case, the maximum energy transfer to zirconium atoms by primary carbon and oxygen recoils is given by:

$$E_{max}^{Zr} = \frac{4M_{Zr}M_x}{(M_{Zr}+M_x)^2} E_{max}^x \quad (4)$$

where  $M_{Zr}$  is the mass of the zirconium atom,  $M_x$  is the mass of carbon or oxygen atoms, and  $E_{max}^x$  is the maximum energy of carbon and oxygen atoms as calculated from Eqn.

(3). Figure 10b presents the maximum recoil energies for Zr atoms after secondary collisions with primary displaced carbon and oxygen atoms. Based on these results, 300 keV electrons cannot displace Zr atoms through secondary collisions with primary carbon and oxygen recoils. Thus, the energy received by zirconium atoms from the incident electron beam will increase the temperature of the specimen, leaving the Zr sublattice undisturbed.

The carbon and oxygen atoms that are displaced by the energetic electrons can diffuse throughout the TEM specimen due to radiation-enhanced diffusion (RED) effects. According to the RED theory, the diffusion of atoms is directly related to the concentration of microstructural defects [44]. Therefore, it can be expected that the RED effects will be enhanced in the ion implanted region of the ZrC foil, where a higher concentration of vacancies and dislocations exists (Figure 3 and 4). This difference in diffusion properties could explain why microstructural changes were observed only in the ion implanted region of the TEM lamella during electron irradiation (Figure 5), and not in the pristine areas (Figure 8). Because the TEM foil is essentially two-dimensional, the displaced atoms can only diffuse and accumulate on the surface of the specimen. As a result, oxygen and carbon enrichment might occur in regions near the foil's surface as the electron irradiation proceeds. Eventually, if the local oxygen concentration exceeds the solubility limit in the matrix, radiation-induced precipitation occurs.

The e-beam induced precipitation of  $\text{ZrO}_2$  nanocrystals could also be influenced by the level of oxygen in the electron irradiated area. In this study, a higher oxygen content was detected in the ion implanted regions of the TEM foil compared to the pristine areas (Figure S2). This implies that more oxygen atoms could be displaced and

diffuse towards the foil surface during e-beam irradiation of the ion-implanted areas. With more oxygen atoms reaching the foil surface, it is more likely that the oxygen solubility limit will be surpassed, and oxide will form after e-beam illumination for a certain period of time.

During electron irradiation of the ion-implanted areas in the TEM foil, it was noted that the oxide diffraction rings appeared diffuse at the beginning and became sharper as the electron irradiation continued (Figure 5). This behavior suggests that the nucleation of the oxide precipitates is probably assisted by electron induced crystallization. Radiation-induced-crystallization (RIC) has been previously observed in amorphous  $\text{ZrO}_2$  [45], [46]. The transition from amorphous domains to crystalline  $\text{ZrO}_2$  is likely promoted by the atomic rearrangements induced by knock-on collisions and other electronic excitations during e-beam irradiation. However, the details of this transition will be studied in future work. The indexing of the diffraction rings also indicated that the oxide precipitates were t- $\text{ZrO}_2$ . Previous work has shown that tetragonal zirconia is energetically favorable as the grain size decreases below a critical value of 15 nm [47].

Interestingly, evidence of decarburization in the electron irradiated area was also observed after prolonged exposure to the e- beam (> 60 min). A similar phenomenon was reported in electron irradiated TiC by Das *et al.* [31]. Decarburization of transition metal carbides can lead to the formation of ordered superstructures, which produce extra diffraction spots in the SAED patterns. In this study, no extra diffraction spots were observed during electron irradiation of the ion-implanted areas. This indicates that carbon ordering did not take place during electron irradiation at room temperature, likely due to the high density of microstructural defects present in ion-implanted areas. Lastly,

it is also worth noting that the formation of oxide precipitates occurred before the decarburization of the foil. This suggests that the oxygen atoms diffuse faster towards the surface of the foil than the carbon atoms. A possible explanation for this behavior can be attributed to the presence of dislocations in the ion implanted area, which can provide fast pathways for the diffusion of oxygen atoms. Furthermore, the dislocation loops and carbon vacancies can also serve as a sink for the displaced carbon atoms and prevent their transport towards the surface. This process might be assisted by electron Ionizing effects that promote redistribution of atoms in different types of traps (defects, grain boundaries, etc.) in ceramics materials.

## 5. CONCLUSIONS

Sequential ion-electron irradiations of  $\text{ZrC}_x$  were conducted with 10 MeV  $\text{Au}^{3+}$  ions and 300 keV electrons to investigate the effects of defects produced during ion irradiation on the response of  $\text{ZrC}_x$  to successive electron irradiation. After ion irradiation of bulk  $\text{ZrC}_x$ , TEM observations revealed that dislocations loops were formed in the ion implanted layer. Additionally, Raman analysis showed an increase in the number of carbon vacancies following ion irradiation. Subsequent electron irradiation of the pre-implanted  $\text{ZrC}_x$  foil resulted in the formation of nanosized tetragonal  $\text{ZrO}_2$  precipitates (5-10 nm) on the surface of the TEM lamella. The discretization of the oxide diffraction rings suggested that the nanoprecipitates were formed by homogeneous nucleation and were randomly oriented with respect to the  $\text{ZrC}$  matrix. The mechanism leading to the formation of  $\text{ZrO}_2$  precipitates was elucidated based on analysis of the electron-specimen

interactions. It is proposed that  $\text{ZrO}_2$  precipitates formed through a knock-on displacement of the oxygen atoms present in the ion implanted layer. The displaced atoms were subsequently transported towards the surface of the TEM foil, likely assisted by radiation-enhanced diffusion effects and momentum transfer during e-beam irradiation, where oxide precipitation occurs. The results highlight the electron beam sensitivity of ion implanted  $\text{ZrC}_x$  and indicate that high-energy electron irradiation of pre-damaged  $\text{ZrC}_x$  foils can induce further modification in the microstructure and chemical composition of the specimen. The outcomes of this work increase the understanding of the microstructural response of  $\text{ZrC}_x$  ceramics to different types of radiation provide new insight into the inadvertent effects of the electron beam during TEM analysis of *in-situ* and *ex-situ* ion irradiated  $\text{ZrC}_x$ .

## ACKNOWLEDGEMENTS

This research was supported by Nuclear Regulatory Commission Faculty Development Grant NRC-HQ-84-15-G-0044 and by the Ceramics program of the U.S. National Science Foundation as part of project DMR 1742086. The microscopy work was conducted at the Electron Microscopy Center (EMC) of the University of Missouri Columbia with partial funding through the EMC Excellence Microscopy Award. Material synthesis and X-ray diffraction measurements were performed using facilities of the Materials Research Center (MRC) located at the Missouri University of Science and Technology. Ion irradiations were performed at the Ion Beam Materials Laboratory located at the University of Tennessee, Knoxville.

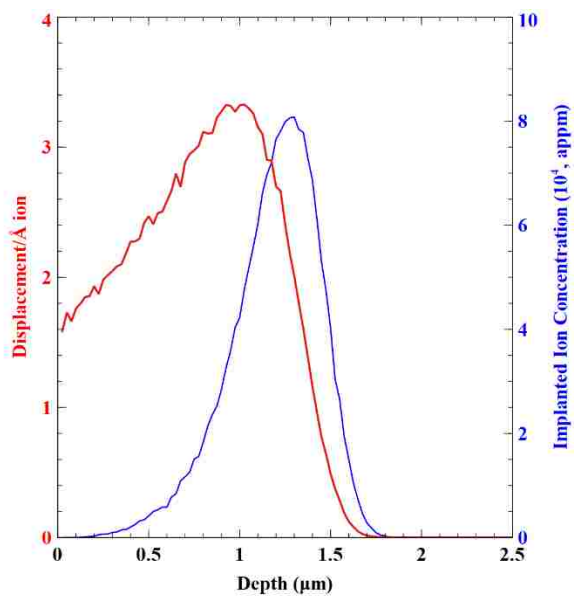


Figure 1. Depth profile of damage level using SRIM Kinchin and Pease calculations, and Au concentration as a function of depth for a fluence of  $3.59 \times 10^{15} \text{ cm}^{-2}$

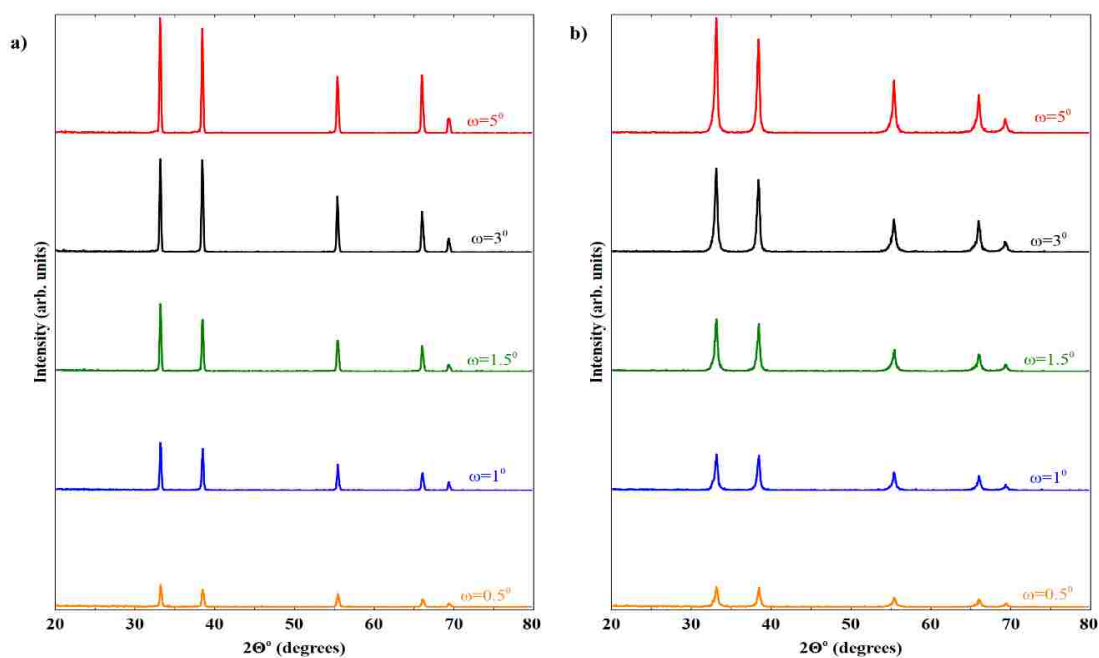


Figure 2. GIXRD diffraction patterns obtained from ZrC a) before, and b) after ion irradiation at room temperature.

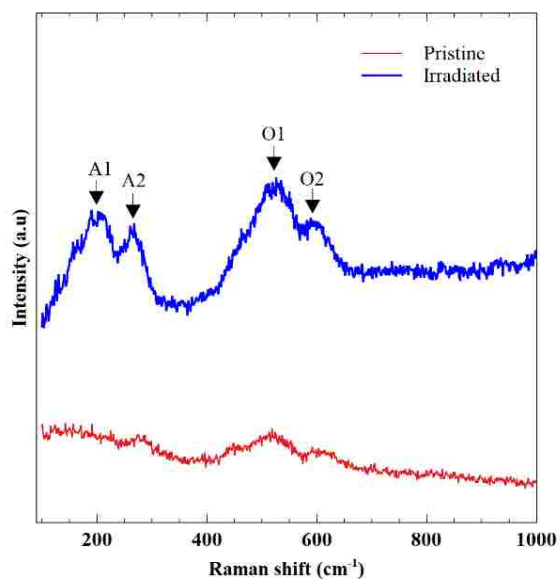


Figure 3. Raman spectra for the pristine and ion irradiated specimens.

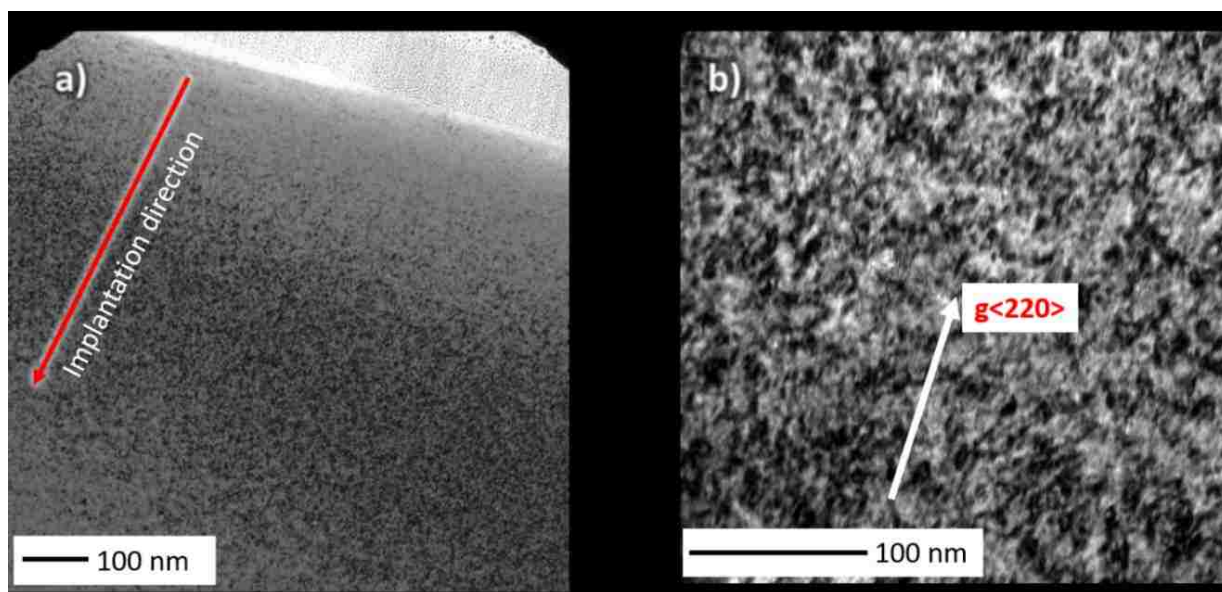


Figure 4. (a) Bright field overview of the ion irradiated ZrC along [110] zone axis, and (b) magnified bright field image showing dislocation loops in the ion implanted layer.



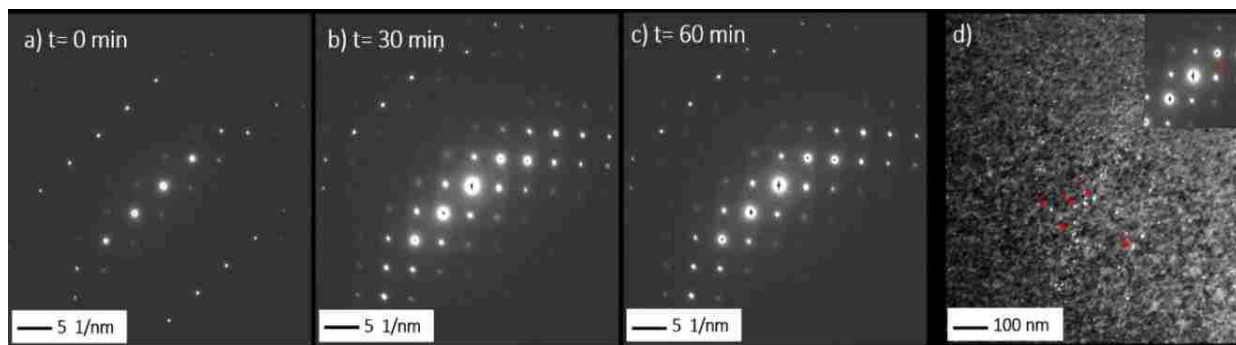


Figure 5. SAD pattern from ion irradiated ZrC (a) initially, (b) after 30 min, and (c) after 60 min of electron irradiation; (d) dark field image after 60 min of electron beam exposure showing some bright  $\text{ZrO}_2$  precipitates (indicated by arrows).

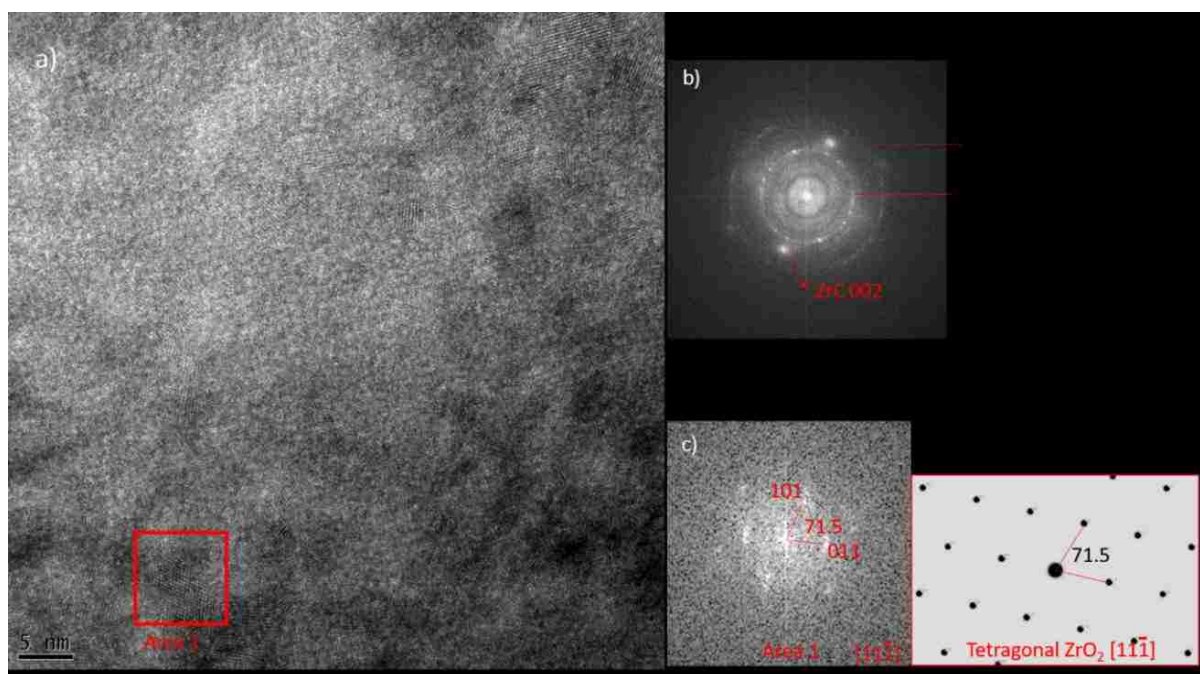


Figure 6. (a) HR-TEM image and (b) FFT pattern of the ion irradiated area after 60 min of electron beam exposure; (c) Experimental FFT of precipitate (red box) and simulated electron diffraction pattern based on the tetragonal structure of  $\text{ZrO}_2$ .

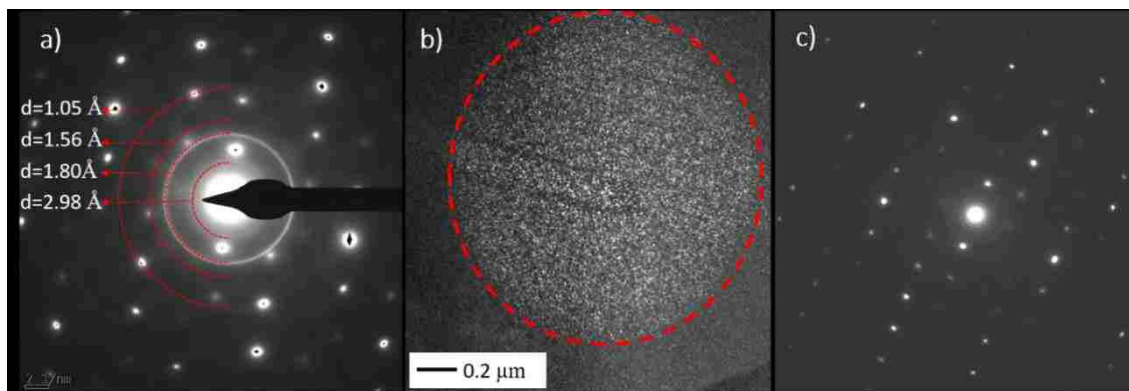


Figure 7. (a) SAD pattern from the ion irradiated ZrC area after 100 min of electron beam exposure, (b) overview dark field image showing the precipitates formed after electron irradiation; (c) SAD pattern acquired in the ion irradiated area adjacent to the e-beam irradiated region.

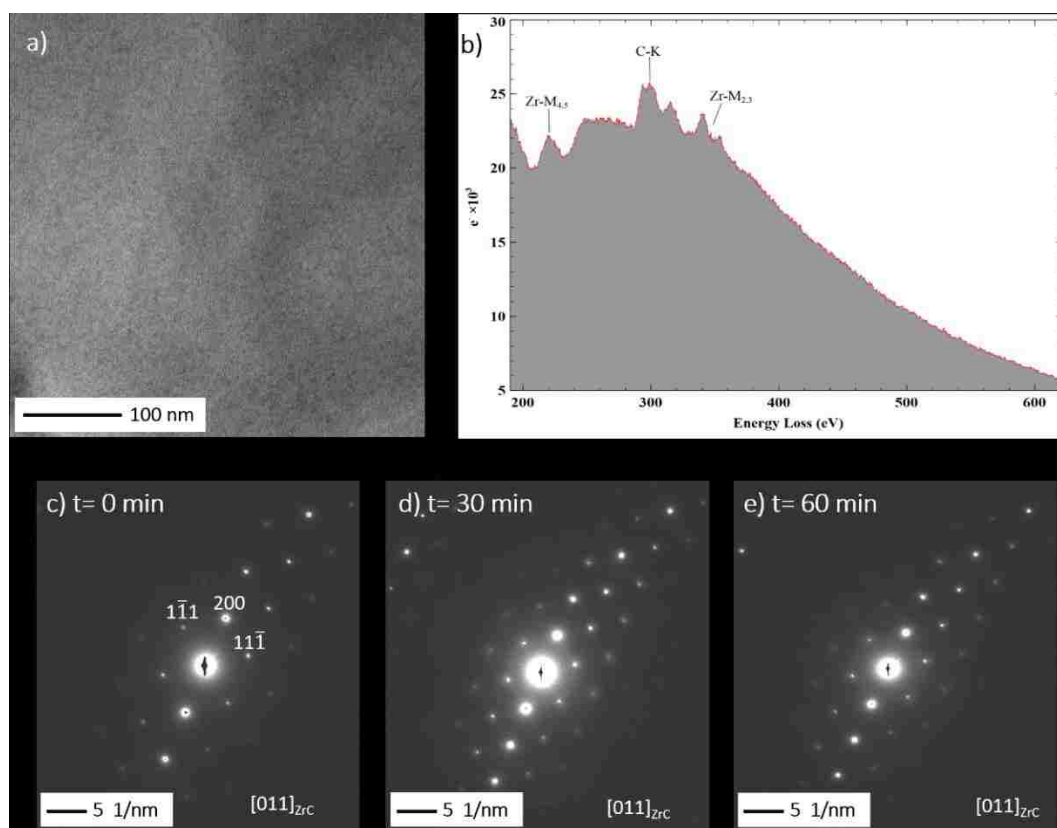


Figure 8. (a) Bright field micrograph of the pristine ZrC grain showing minor FIB damage; (b) EELS spectra of pristine ZrC grain after e-beam exposure; SAD pattern from pristine (c) initially, (d) after 30 min, and (e) after 60 min of electron irradiation.

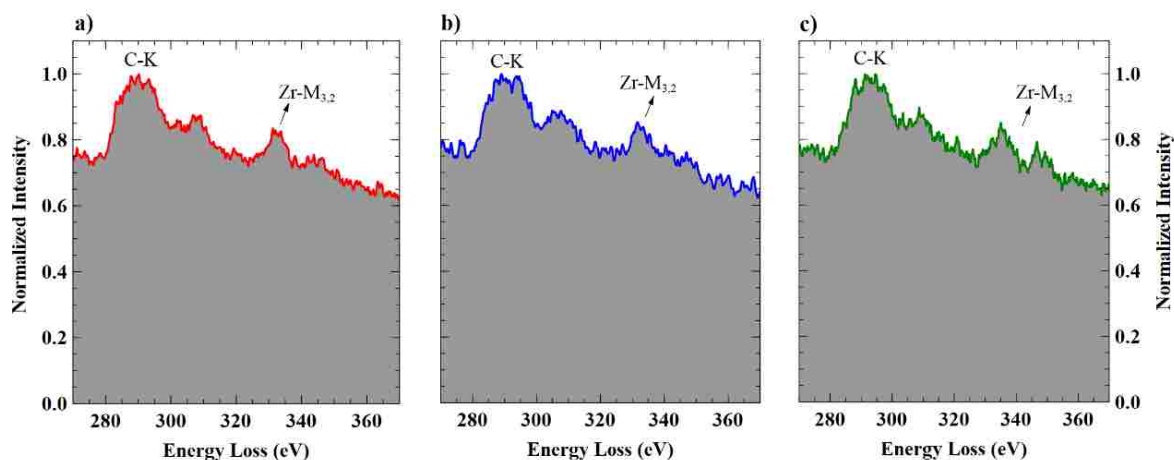


Figure 9. EELS spectrum from ZrC grains obtained (a) from the pristine area, (b) ion-irradiated area, and (c) ion-implanted area after 100 min of electron beam exposure.

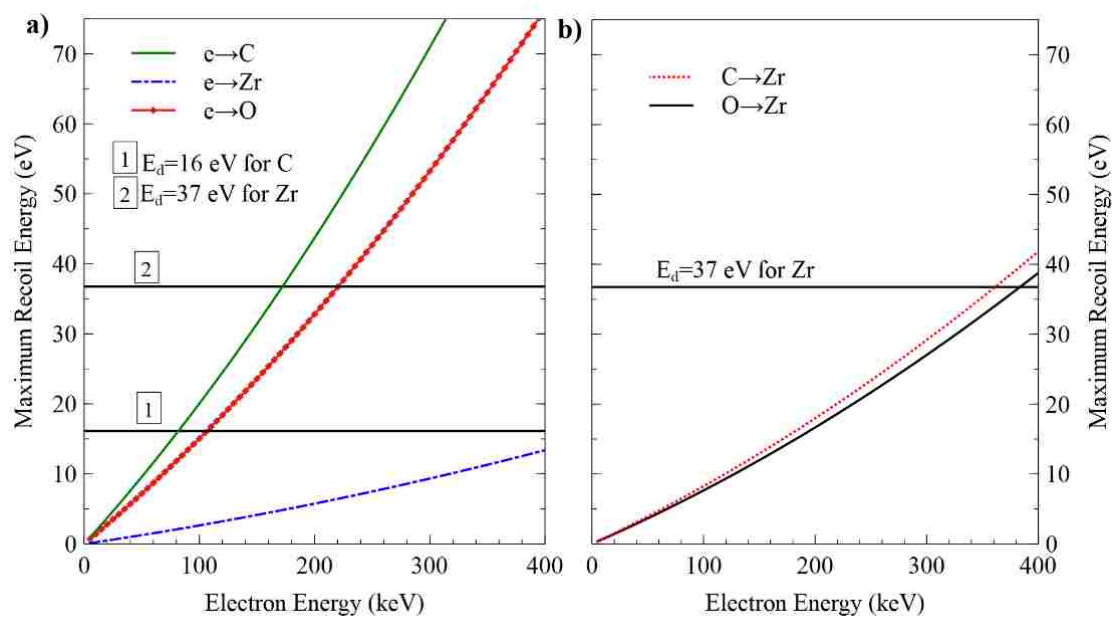


Figure 10. (a) Maximum energy transfer to atoms by electrons, (b) maximum energy transfer to Zr atoms by primary carbon and oxygen recoils.

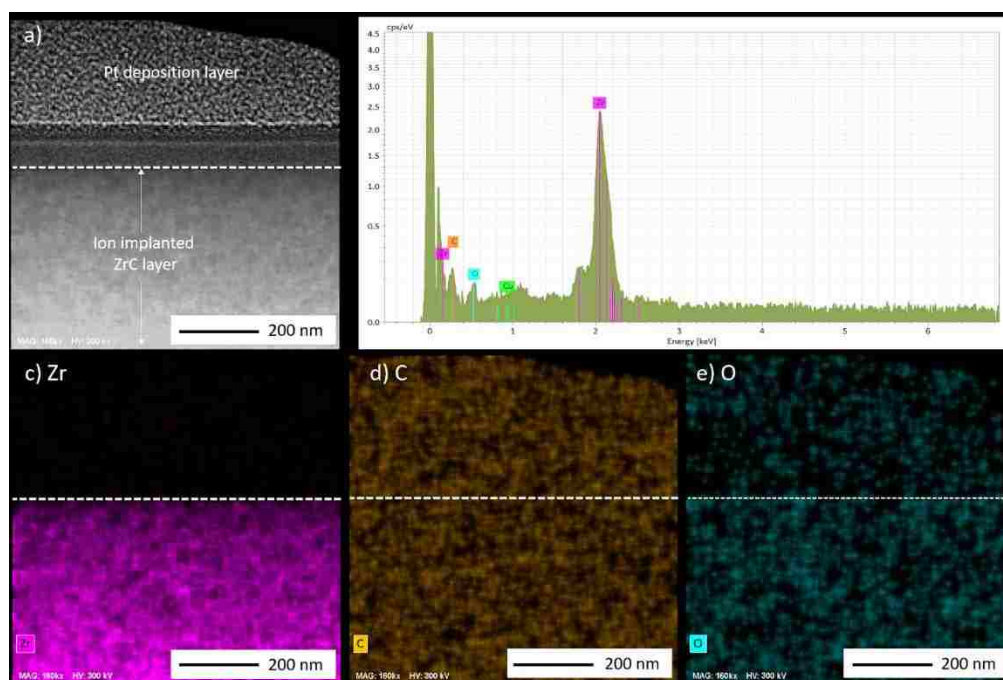


Figure S1. Elemental mapping of the ion implanted area obtained by STEM-EDX after ion irradiation with 10 MeV  $\text{Au}^{3+}$  to 10 dpa.

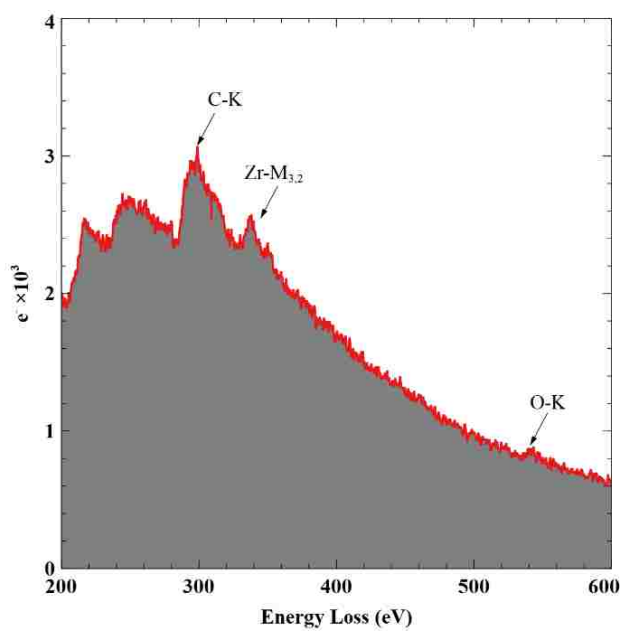


Figure S2. EELS spectrum from ion irradiated ZrC grain after electron beam exposure.

## REFERENCES

- [1] R. W. Harrison and W. E. Lee, "Processing and properties of ZrC, ZrN and ZrCN ceramics: a review," *Adv. Appl. Ceram.*, vol. 115, no. 5, pp. 294–307, 2016.
- [2] L. N. Grossman, "High-Temperature Thermophysical Properties of Zirconium Carbide," *J. Am. Ceram. Soc.*, vol. 48, no. 5, pp. 236–242, 1965.
- [3] K. Fukuda, K. Ikawa, and K. Iwamoto, "Fission product diffusion in ZrC coated fuel particles," *J. Nucl. Mater.*, vol. 87, no. 2-3, pp. 367–374, 1979.
- [4] Y. Katoh, G. Vasudevamurthy, T. Nozawa, and L. L. Snead, "Properties of zirconium carbide for nuclear fuel applications," *J. Nucl. Mater.*, vol. 441, no. 1–3, pp. 718–742, 2013.
- [5] R. Ding, H. Wang, Y. Jiang, R. Liu, K. Jing, M. Sun, R. Zhang, S. Qiu, Z. Xie, H. Deng, X. Wang, M. Kong, W. Jiang, W. Fang, and C. Liu, "Effects of ZrC addition on the microstructure and mechanical properties of Fe-Cr-Al alloys fabricated by spark plasma sintering," *J. Alloys Compd.*, vol. 805, pp. 1025–1033, 2019.
- [6] G. Vasudevamurthy, T. W. Knight, E. Roberts, and T. M. Adams, "Laboratory production of zirconium carbide compacts for use in inert matrix fuels," *J. Nucl. Mater.*, vol. 374, no. 1-2, pp. 241–247, 2008.
- [7] R. Liu, Z. M. Xie, J. F. Yang, T. Zhang, T. Hao, X. P. Wang, Q. F. Fang, and C. S. Liu, "Recent progress on the R&D of W-ZrC alloys for plasma facing components in fusion devices," *Nucl. Mater. Energy*, vol. 16, no. May, pp. 191–206, 2018.
- [8] C. J. Ulmer, A. T. Motta, and M. A. Kirk, "In situ ion irradiation of zirconium carbide," *J. Nucl. Mater.*, vol. 466, pp. 606–614, 2015.
- [9] D. Gosset, M. Dollé, D. Simeone, G. Baldinozzi, and L. Thomé, "Structural evolution of zirconium carbide under ion irradiation," *J. Nucl. Mater.*, vol. 373, no. 1–3, pp. 123–129, 2008.
- [10] D. Gosset, M. Dollé, D. Simeone, G. Baldinozzi, and L. Thomé, "Structural behaviour of nearly stoichiometric ZrC under ion irradiation," *Nucl. Instruments Methods Phys. Res. Sect. B Beam Interact. with Mater. Atoms*, vol. 266, no. 12–13, pp. 2801–2805, 2008.
- [11] S. Pellegrino, J. P. Crocombette, A. Debelle, T. Jourdan, P. Trocellier, and L. Thomé, "Multi-scale simulation of the experimental response of ion-irradiated zirconium carbide: Role of interstitial clustering," *Acta Mater.*, vol. 102, pp. 79–87, 2016.

- [12] S. Agarwal, A. Bhattacharya, P. Trocellier, and S. J. Zinkle, "Helium induced microstructure damage, nano-scale grain formation and helium retention behaviour of ZrC," *Acta Mater.*, vol. 163, pp. 14–27, Jan. 2019.
- [13] Y. Yang, W.-Y. Lo, C. Dickerson, and T. R. Allen, "Stoichiometry effect on the irradiation response in the microstructure of zirconium carbides," *J. Nucl. Mater.*, vol. 454, no. 1–3, pp. 130–135, 2014.
- [14] L. L. Snead, Y. Katoh, and S. Kondo, "Effects of fast neutron irradiation on zirconium carbide," *J. Nucl. Mater.*, vol. 399, no. 2–3, pp. 200–207, 2010.
- [15] J. Gan, M. Meyer, R. Birtcher, and T. Allen, "Microstructure Evolution in ZrC Irradiated with Kr ions," *J. ASTM Int.*, vol. 3, no. 4, p. 12376, 2006.
- [16] C. J. Ulmer, A. T. Motta, and M. A. Kirk, "In situ ion irradiation of zirconium carbide," *J. Nucl. Mater.*, vol. 466, pp. 606–614, 2015.
- [17] S. Shimada and T. Ishil, "Oxidation Kinetics of Zirconium Carbide at Relatively Low Temperatures," *J. Am. Ceram. Soc.*, vol. 73, no. 10, pp. 2804–2808, 1990.
- [18] B. S. Vasile, D. Craciun, P. Ionescu, D. Pantelica, G. Dorcioman, and V. Craciun, "Microstructure of 800 keV Ar ion irradiated thin ZrC films," *Appl. Surf. Sci.*, vol. 442, pp. 773–777, 2018.
- [19] J. Gan, Y. Yang, C. Dickson, and T. Allen, "Proton irradiation study of GFR candidate ceramics," *J. Nucl. Mater.*, vol. 389, no. 2, pp. 371–325, 2009.
- [20] Y. Zhang, M.L. Crespillo, H. Xue, K. Jin, C.H. Chen, C.L. Fontana, J.T. Graham, and W.J. Weber, "New ion beam materials laboratory for materials modification and irradiation effects research," *Nucl. Instruments Methods Phys. Res. Sect. B Beam Interact. with Mater. Atoms*, vol. 338, pp. 19–30, 2014.
- [21] M. L. Crespillo, J. T. Graham, Y. Zhang, and W. J. Weber, "In-situ luminescence monitoring of ion-induced damage evolution in SiO<sub>2</sub> and Al<sub>2</sub>O<sub>3</sub>," *J. Lumin.*, vol. 172, pp. 208–218, 2016.
- [22] M. L. Crespillo, J. T. Graham, Y. Zhang, and W. J. Weber, "Temperature measurements during high flux ion beam irradiations," *Rev. Sci. Instrum.*, vol. 87, no. 2, p. 024902, 2016.
- [23] J. F. Ziegler, M. D. Ziegler, and J. P. Biersack, "SRIM - The stopping and range of ions in matter (2010)," *Nucl. Instruments Methods Phys. Res. Sect. B Beam Interact. with Mater. Atoms*, vol. 268, no. 11–12, pp. 1818–1823, 2010.
- [24] M. J. Zheng, I. Szlufarska, and D. Morgan, "Ab initio prediction of threshold displacement energies in ZrC," *J. Nucl. Mater.*, vol. 471, pp. 214–219, 2016.

- [25] R. E. Stoller, M. B. Toloczko, G. S. Was, A. G. Certain, S. Dwaraknath, and F. A. Garner, "On the use of SRIM for computing radiation damage exposure," *Nucl. Instruments Methods Phys. Res. Sect. B Beam Interact. with Mater. Atoms*, vol. 310, pp. 75–80, 2013.
- [26] Y. Zhang, M. A. Tunes, Matheus, M.L. Crespillo, F. Zhang, W. L. Boldman, P. D. Rack, L. Jiang, C. Xu, G. Greaves, S. E. Donnelly, L. Wang, and W. J. Weber, "Thermal stability and irradiation response of nanocrystalline CoCrCuFeNi high-entropy alloy," *Nanotechnology*, vol. 30, no. 29, p. 294004, 2019.
- [27] G. S. Was, *Fundamentals of radiation materials science: Metals and alloys, second edition*. 2016.
- [28] ASTM, "ASTM C373-14 Standard Test Method for Water Absorption, Bulk Density, Apparent Porosity, and Apparent Specific Gravity of Fired Whiteware Products," *Astm C373-88*, 1999.
- [29] H. Wipf, M. V. Klein, and W. S. Williams, "Vacancy-Induced and Two-Phonon Raman Scattering in ZrCx, NbCx, HfCx, and TaCx," *Phys. status solidi*, vol. 108, no. 2, pp. 489–500, 1981.
- [30] S. Pellegrino, P. Trocellier, L. Thom  , S. Miro, J. M. Costantini, and E. Jouanny, "Raman investigation of ion irradiated TiC and ZrC," *Nucl. Instruments Methods Phys. Res. Sect. B Beam Interact. with Mater. Atoms*, vol. 454, no. 1, pp. 61-67, 2019.
- [31] G. Das, D. K. Chatterjee, and H. A. Lipsitt, "Electron irradiation damage in TiC," *J. Mater. Sci.*, vol. 16, no. 12, pp. 3283–3291, 1981.
- [32] V. Jeanne-Rose, V. Golabkan, J. L. Mansot, L. Largitte, T. Cesaire, and A. Ouensanga, "An EELS-based study of the effects of pyrolysis on natural carbonaceous materials used for activated charcoal preparation," *J. Microsc.*, vol. 210, no. 1, pp. 53–59, 2003.
- [33] A. J. Craven and L. A. J. Garvie, "Electron Energy Loss Near Edge Structure (ELNES) on the Carbon K-Edge in Transition Metal Carbides with the Rock Salt Structure," *Microsc. Microanal. Microstruct.*, vol. 6, no. 1, pp. 89–98, 1995.
- [34] K. A. Mkhoyan and J. Silcox, "Electron-beam-induced damage in wurtzite InN," *Appl. Phys. Lett.*, vol. 82, no. 6, pp. 859-861, 2003.
- [35] A. J. Craven, M. M. Cluckie, S. P. Duckworth, and T. N. Baker, "Analysis of small vanadium carbide precipitates using Electron Energy Loss Spectroscopy," *Ultramicroscopy*, vol. 28, no. 1-4, pp. 330-334, 1989.

- [36] Y. Pipon, N. Toulhoat, N. Moncoffre, G. Gutierrez, A. Maître, and M. Gendre, "Influence of the Oxygen content on the thermal migration of Xenon in  $\text{ZrC}_x\text{O}_{1-x}$ ," *J. Nucl. Mater.*, vol. 440, no. 1–3, pp. 546–552, 2013.
- [37] D. B. Williams and C. B. Carter, *Transmission Electron Microscopy*. Boston, MA: Springer US, 2009.
- [38] I. Jenčič, M. W. Bench, I. M. Robertson, and M. A. Kirk, "Electron-beam-induced crystallization of isolated amorphous regions in Si, Ge, GaP, and GaAs," *J. Appl. Phys.*, vol. 78, no. 2, pp. 974–982, 1995.
- [39] W. Lengauer, S. Binder, K. Aigner, P. Ettmayer, A. Guillou, G. Debuigne, and G. Groboth, "Solid state properties of group IVb carbonitrides," *J. Alloys Compd.*, vol. 217, no. 1, pp. 137–147, 1995.
- [40] R. E. Taylor and E. K. Storms, "Thermal Transport in Refractory Carbides," 1976.
- [41] C. Jensen, M. Chirtoc, N. Horny, J. S. Antoniow, H. Pron, and H. Ban, "Thermal conductivity profile determination in proton-irradiated ZrC by spatial and frequency scanning thermal wave methods," *J. Appl. Phys.*, vol. 114, no. 13, p. 133509, 2013.
- [42] C. Jensen, M. Chirtoc, J. S. Antoniow, and H. Ban, "In-depth thermal-conductivity profile of ion-irradiated zirconium carbide using scanning thermal microscopy," *Int. J. Thermophys.*, vol. 34, no. 4, pp. 597–608, 2013.
- [43] S. J. Zinkle and C. Kinoshita, "Defect production in ceramics," *J. Nucl. Mater.*, vol. 251, no. 11, pp. 200–217, 1997.
- [44] G. J. Dienes and A. C. Damask, "Radiation Enhanced Diffusion in Solids," *J. Appl. Phys.*, vol. 29, no. 12, pp. 1713–1721, 1958.
- [45] A. G. Bagmut and V. M. Beresnev, "Kinetics of the electron beam induced crystallization of amorphous  $\text{ZrO}_2$  films obtained via ion-plasma and laser sputtering," *Phys. Solid State*, vol. 59, no. 1, pp. 151–155, 2017.
- [46] H. M. Naguib and R. Kelly, "The crystallization of amorphous  $\text{ZrO}_2$  by thermal heating and by ion bombardment," *J. Nucl. Mater.*, vol. 35, no. 3, pp. 293–305, 1970.
- [47] R. C. Garvie, "Stabilization of the tetragonal structure in zirconia microcrystals," *J. Phys. Chem.*, vol. 82, no. 2, pp. 218–224, 1978.



## SECTION

### 3. SUMMARY AND CONCLUSIONS

The purpose of this dissertation was to investigate the microstructural evolution of  $\text{ZrC}_x$  ceramics under ion and electron irradiation conditions. In the first part of the thesis, efforts were made to characterize the microstructure of  $\text{ZrC}_x$  irradiated with 10 MeV  $\text{Au}^{3+}$  ions up to doses of 30 displacement per atoms (dpa) at 800 °C. To date, most of the studies on irradiated  $\text{ZrC}_x$  have only focused on the low dose (< 5 dpa), low temperature (25 °C) irradiation regime. Thus, the results of the first part of the dissertation contribute to extend the current state of knowledge of the irradiation response of  $\text{ZrC}_x$  at conditions that are relevant to the operation of advanced Gen-IV gas-cooled nuclear reactors.

Post-irradiation examination (PIE) of the ion-irradiated specimens was conducted using a complementary set of techniques (transmission electron microscopy, X-ray diffraction, and Raman spectroscopy) to provide a more comprehensive view of the irradiation response of  $\text{ZrC}_x$  ceramics. The results indicated that  $\text{ZrC}_x$  did not amorphize at doses up to 30 dpa, confirming its superior radiation stability. Coarsening of the defective microstructure, as a function of dose, was revealed by transmission electron microscopy analysis. Black dot defects were observed at low doses (0.5 dpa), and tangled dislocation networks were formed at 5 dpa. Beyond this dose, little change was observed in the irradiated microstructure, which suggested that a balance had been reached between irradiation damage buildup and dynamic annealing of defects. Diffraction analysis showed a change in the defect structure occurred at doses close to ~2.5 dpa. This

change was attributed to coalescence of dislocation loops and formation of dislocation networks. The evolution of lattice parameter with dose indicated that uptake of adventitious oxygen could occur in specimens irradiated at high doses. Oxygen uptake might be assisted by radiation-enhanced diffusion processes by the changing microstructure (i.e. pipe diffusion at high doses). Raman spectroscopy analysis indicated an increase in non-stoichiometry after irradiation, due to an increase in carbon vacancies produced by the irradiation.

Additionally, concurrent oxidation of  $\text{ZrC}_x$  occurred during ion irradiation at 800 °C. Nanosized, discrete  $\text{ZrO}_2$  nodules were observed to grow over the surface of  $\text{ZrC}_x$ . No amorphization of the  $\text{ZrO}_2$  precipitates was observed at doses up to 15 dpa, confirming the high radiation resistance of  $\text{ZrO}_2$  phase. Concomitant reduction in size and surface coverage of the oxide nodules was observed at high doses, indicating that radiation-induced processes could enhance the dissolution of oxide precipitates under irradiation conditions. Morphological changes were also observed in the irradiated oxide nodules as a function dose. At doses above 2.5 dpa, the oxide islands became more faceted and exhibited diffuse oxide/matrix interfaces. Furthermore, nucleation and growth of cavities was observed within the oxide nodules irradiated to 2.5 dpa and above. These results shed light on the complex in-service oxidation of  $\text{ZrC}_x$  in high temperature nuclear reactors and provide information that will enable better design and safe operation of the next generation of nuclear power systems.

In the second part of the dissertation, the microstructural evolution of  $\text{ZrC}_x$  under sequential ion-electron irradiation conditions was investigated. First, bulk ion irradiation of  $\text{ZrC}_x$  was conducted with 10 MeV  $\text{Au}^{3+}$  ions at room temperature. TEM analysis of the

ion-irradiated specimen revealed that dislocations loops were formed in the ion implanted layer. Additionally, Raman analysis showed an increase in the number of carbon vacancies following ion irradiation. Subsequent electron irradiation of the pre-implanted  $\text{ZrC}_x$  foil in the TEM instrument resulted in the formation of nanosized tetragonal  $\text{ZrO}_2$  precipitates (5-10 nm diameter) on the surface of the lamella. The discretization of the oxide diffraction rings in the SAED patterns suggested that the nanoprecipitates were formed by homogeneous nucleation and were randomly oriented with respect to the  $\text{ZrC}_x$  matrix. The mechanism leading to the formation of  $\text{ZrO}_2$  precipitates was elucidated based on analysis of the electron-specimen interactions. It is proposed that  $\text{ZrO}_2$  precipitates formed through a knock-on displacement of the oxygen atoms present in the ion implanted layer. The displaced atoms are subsequently transported towards the surface of the TEM foil, likely assisted by radiation-enhanced diffusion effects and momentum transfer during e-beam irradiation, where oxide precipitation occurs.

Overall, the work presented in this dissertation led the authors to the following conclusions:

1. Even though  $\text{ZrC}_x$  ceramics exhibit high radiation resistance up to doses of 30 dpa at 800 °C, precautions must be taken to prevent its oxidation during reactor operation. Given the high thermodynamic driving force for oxidation of  $\text{ZrC}_x$ , reactors components based on  $\text{ZrC}_x$  will be oxidize when expose to impure helium coolant. Thus, it would be necessary to develop composites with improved oxidation resistance or suitable environmental barrier coatings that will be capable of protecting the structural integrity of  $\text{ZrC}_x$  under normal operation conditions of Gen-IV gas-cooled reactors.

2. The results of the second part of the dissertation highlight the electron beam sensitivity of ion implanted  $\text{ZrC}_x$ . High-energy electron irradiation of pre-damaged  $\text{ZrC}_x$  foils can induce further modification in the microstructure and chemical composition of the specimen. Therefore, precautions must be taken to prevent the incorporation of inadvertent effects during TEM analysis of *in-situ* and *ex-situ* ion irradiated  $\text{ZrC}_x$ .

#### 4. FUTURE WORK

Several suggestions are presented in this section for advancing understanding of the radiation response of  $\text{ZrC}_x$  ceramics:

1. It was discovered that oxygen uptake occurs during high temperature ion irradiation of  $\text{ZrC}_x$ . More research is needed to understand the mechanisms driving the oxygen incorporation into the substrate. This effort will likely require the combination of experiments and simulations. Understanding the mechanisms of oxygen-uptake will be valuable for engineering optimal ion irradiation techniques that prevent and/or alleviate oxygen uptake in sensitive materials such as  $\text{ZrC}_x$ . Developing high fidelity ion irradiations is essential to evaluate the response to irradiation of core materials.
2. It has been shown that concurrent oxidation occurs during ion irradiation of  $\text{ZrC}_x$  at 800 °C. It is recommended to conducting additional irradiation experiments at various temperatures and doses to provide a better understanding of the oxidation mechanism of  $\text{ZrC}_x$  under irradiation conditions. Additionally, future analysis of the oxidation islands should perform atomic force microscopy (AFM) measurements to obtain a 3D reconstruction of the oxide islands. This will enable evaluate the dimensions and faceting of the oxide nodules accurately. Such parameters can be used as input/validation parameters in future simulations models of  $\text{ZrC}_x$  oxidation.
3. Raman analysis in transverse TEM lift-out specimens. In the current work, Raman measurements were conducted on the surface of the ion-irradiated specimens. Since

the Raman penetration depth is strongly dependent on laser power and the material's optical density, it is difficult to know accurately if the Raman signal originated from the near surface area, peak damage area, or non-irradiated area of the ion-irradiated specimen. Therefore, to overcome this issue and obtain a more accurate knowledge of the distribution of carbon vacancies along the implantation profile, it is recommended to perform Raman analysis on transverse cross section obtained by FIB lift-out.

4. The structure of the ion irradiated  $\text{ZrC}_x$  was characterized by TEM analysis to a limited extent. It is recommended to perform a detailed TEM analysis of the defect population (e.g. dislocation type and nature) and change in chemical properties (such as radiation induced segregation) as a function of dose. The knowledge of the defect characteristics including loop nature, Burgers vectors, and habit or slip planes, will constitute a significant step to better understand and predict the behavior of  $\text{ZrC}$  under irradiation conditions.
5. It is also recommended to perform *in-situ* ion irradiation in thin foil  $\text{ZrC}_x$  specimens to investigate the mechanism of radiation-induced oxygen segregation.

## APPENDIX

### FABRICATION AND MICROSTRUCTURAL ANALYSIS OF HOT-PRESSED $\text{ZrC}_x$ WITH LOW Hf-CONTENT

Raul Florez<sup>a</sup> Xiaoqing He<sup>b,c</sup>, Tommi A. White<sup>c,d</sup>, Gregory Hilmas<sup>e</sup>, William Fahrenholtz<sup>e</sup>, Joseph Graham<sup>a,e\*</sup>

<sup>a</sup>. Nuclear Engineering Program, Missouri University of Science and Technology, 65409 Rolla, MO, United States

<sup>b</sup>. Electron Microscopy Core, University of Missouri, 65211 Columbia, MO, United States

<sup>c</sup>. Department of Mechanical and Aerospace Engineering, University of Missouri, 65211 Columbia, MO, United States

<sup>d</sup>. Department of Biochemistry, University of Missouri, Columbia, MO, 65211, United States

<sup>e</sup>. Department of Materials Science and Engineering, Missouri University of Science and Technology, 65409 Rolla, MO, United States

## ABSTRACT

Zirconium Carbide ( $\text{ZrC}_x$ ) powder with low Hf content (~400 ppm) was synthesized by carbothermal reduction of  $\text{ZrO}_2$  with carbon black. The synthesized powder was hot-pressed without any sintering additives at 2200 °C to produce  $\text{ZrC}_x$  ceramics with relative density >95%. Microstructural analysis revealed  $\text{ZrC}_x$  monoliths with a mean grain size of 4.2  $\mu\text{m}$  and residual carbon and oxycarbide inclusions. The formation of carbon and oxygen-rich inclusions was attributed to the presence residual free carbon and oxide contaminants in the starting  $\text{ZrC}_x$  powder. Raman analysis evidenced structural

reorganization of free carbon into the disordered graphite inclusions during hot pressing. Additionally, transmission electron microscopy analysis of the oxycarbide inclusions showed a complex core-shell structure, which exhibited compositional differences between the core and shell regions. The results of this work provide new insights into role of the main impurities on the microstructural evolution of  $\text{ZrC}_x$  ceramics during densification.

**Keywords:  $\text{ZrC}_x$ , Hot Pressing, Microstructure, XRD, Raman, EBSD, TEM**

---

\* Corresponding author:

Email: grahamjose@mst.edu

## 1. INTRODUCTION

Zirconium Carbide ( $\text{ZrC}_x$ ) is a promising inert matrix fuel (IMF) matrix material for advanced gas-cooled fast reactors (GFR) [1]. This type of Gen-IV nuclear reactor is designed to operate at a nominal temperature of 1400 °C and has the unique ability to burn long-lived transuranic elements and fission products [2]. As a potential inert matrix fuel for GFR,  $\text{ZrC}_x$  exhibits several advantages over both oxide and metal matrix alternatives. Foremost of these advantages include: high melting point ( $T_m=3420^\circ\text{C}$ ) [3], outstanding mechanical properties [4], higher thermal and electrical conductivities than SiC [5], resistance to fission product attack [6], low neutron absorption cross section [7], and microstructural stability under irradiation conditions [8], [9], [10].

$\text{ZrC}_x$  is known for its poor sinterability due to its highly covalent bonding character and low self-diffusion coefficients [11], [12], [13]. Consequently, high temperatures (e.g.,  $>2000^\circ\text{C}$ ) and pressure assisted methods are usually needed to



produce dense monolithic  $\text{ZrC}_x$  ceramics with the required structural properties for nuclear applications. Different sintering methods have been used to fabricate dense  $\text{ZrC}_x$  bodies including reactive and non-reactive hot-pressing [14], spark plasma sintering (SPS) [15], pressureless sintering (PLS) [16], and arc melting [17]. Among these methods, SPS and hot-pressing of  $\text{ZrC}_x$  powders produced by the carbothermal reduction are the most suitable routes for large scale production. Examination of the microstructure morphology, equilibrium phase behavior [18], thermomechanical properties [19], [20], [21], fission product release [22], [23], and oxidation behavior [24], [25] of  $\text{ZrC}_x$  ceramics has been previously reported. Furthermore, several studies have been conducted to understand the microstructural evolution of  $\text{ZrC}_x$  ceramics under different types of irradiation such as neutron [10], heavy ions [9], [26], [27] and protons [8], [28]. Certainly, the historic data on  $\text{ZrC}_x$  have provided insight into the behavior of  $\text{ZrC}_x$  that is pertinent to its use as inert matrix fuel in GFRs. However, a careful examination of the literature shows that it lacked detailed structural and chemical compositional assessment of the pre-irradiated  $\text{ZrC}_x$  specimens, preventing a complete understanding of irradiation behavior of  $\text{ZrC}_x$ . Most of the previous work has been conducted on  $\text{ZrC}$  ceramics produced from commercially available powders with quantitative analysis rarely reported.

One of the main limitations of the previous work on  $\text{ZrC}_x$  is the lack of detailed chemical analysis for Hafnium (Hf) content. Hafnium is a ubiquitous substitutional impurity in zirconium precursors that is difficult to separate because of its chemical similarity to zirconium [29]. Application in GFRs have a stringent specification limit for Hf content in inert fuel matrices due to its deleterious effects in the neutronic and thermal

properties of  $\text{ZrC}_x$  ceramics. Hf has a high thermal neutron absorption cross-section and resonance integral that affect the neutron economy in a nuclear reactor [30]. Moreover, the presence of substitutional Hf impurities ( $\text{Hf}_{\text{Zr}}$ ) in  $\text{ZrC}_x$  will degrade the phonon contribution to the thermal conductivity due to the large mass difference between Hf and Zr and resulting enhancement in phonon scattering [31], [32]. Microstructural changes might also be induced by the presence of Hf impurities in  $\text{ZrC}_x$ . In this regard, the combination of Hf impurities in  $\text{ZrC}_x$  and the temperatures typically used for synthesis may either inhibit formation of other phases in the Zr-C system or result in relaxation to disordered states that remain metastable when the system is cooled to room temperature. Therefore, to provide a more fundamental understanding of the thermal and structural properties of  $\text{ZrC}_x$  before and after irradiation, it is essential to fabricate high purity  $\text{ZrC}_x$  ceramics with low Hf content and perform a comprehensive characterization of the resulting microstructure.

The purpose of this study was to characterize the microstructure of hot-pressed  $\text{ZrC}_x$  ceramics with low Hf-content.

## 2. MATERIALS AND METHODS

### 2.1. SAMPLE PREPARATION

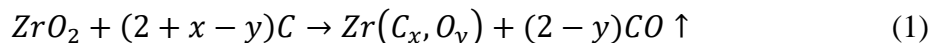
This section describes the preparation route of the powder and the densification conditions used to fabricate the ZrC billets.

**2.1.1 Synthesis of  $\text{ZrO}_2$  precursor.** High purity  $\text{ZrO}_2$  powders with low Hf content were synthesized by precipitation using  $\text{ZrCl}_4$  (Reactor grade, >99.5% metal

basis, Alfa Aesar) and  $\text{NH}_4\text{OH}$  (28 %, Alfa Aesar) as starting materials. Precipitation was induced by dropwise addition of 28%  $\text{NH}_4\text{OH}$  to 0.4 M aqueous  $\text{ZrCl}_4$  solution until the pH reached 10. After aging for 30 minutes under strong magnetic stirring, the precipitate was filtered and washed with deionized water to remove chloride ions. The hydrous cake was then dried at 120 °C overnight. Afterwards, the powder was calcined in a convection oven at 700 °C for 4 hours to produce  $\text{ZrO}_2$ . The obtained powder was lightly ground with a mortar and pestle and passed through a 60 mesh sieve.

**2.1.2. Synthesis of ZrC powder.** The synthesized  $\text{ZrO}_2$  and carbon black (BP-1100, Cabot Corporation, Alpharetta, GA, USA) powders were used as starting materials for ZrC synthesis. The starting powders were batched with a molar ratio of  $\text{ZrO}_2\text{:C}=1\text{:}3$ . This composition was selected to produce a ZrC ceramics with a  $\text{C/Zr}=1$  stoichiometry, which is the target stoichiometry of the ZrC fuel development program in the United States [10]. The powder mixture was ball-milled using zirconia milling media and acetone for 24 hours. Afterwards, the slurry was dried by rotary evaporation (Rotavapor R-124; Buchi, Flawil, Germany) at a temperature of 80 °C, under low vacuum (~27 kPa), and at a rotation speed of 120 rpm. The dried powder was passed through a 50-mesh sieve and pelletized by uniaxial pressing before carbothermal reduction.

Solid state carbothermal reduction was conducted in a graphite element furnace (3060-FP20, Thermal Technology, Santa Rosa, CA, USA) under mild vacuum conditions (~20 Pa). The mixed powder was heated from room temperature to 1800 °C at a heating rate of 10 °C/min, and dwell time of 6 hours to promote the reaction:



**2.1.3. Densification.** A pellet was prepared by hot-pressing the synthesized ZrC powder. The powder was hot pressed in a 25.4 mm cylindrical graphite die lined with BN-coated (SP-180 Cerac, Milwaukee, WI) graphite foil (2010-A; Mineral Seal Corp, Tucson, Arizona). Before hot pressing, the powder was loaded into the die and cold compacted in a uniaxial press at ~2MPa. The powder was then heated under vacuum (~20 Pa) to 1600 °C with an average heating rate of 20 °C/min. Upon reaching 1600 °C, the furnace was backfilled with helium and a uniaxial pressure of 32 MPa was applied to the powder compact. The furnace was then heated at 50 °C/min to 2200 °C. After 90 min, the furnace was cooled at ~50 °C/min. The load was removed when the die temperature dropped below 1600 °C.

Following densification, the specimens for microscopy analysis from the billet parallel to the hot pressing with a slow-speed diamond saw. The surface of the ZrC foil was then polished to a 0.25 µm mirror-finish using successively finer diamond abrasives. After polishing, the specimens were ultrasonically cleaned in ethanol for 15 min at room temperature.

## 2.2. MATERIAL CHARACTERIZATION

This section describes the experimental techniques that were used to examine the microstructure of the as-fabricated specimens.

**2.2.1. Density and Chemical Analysis.** The bulk density of the hot-pressed billet was measured by the Archimedes' method performed in accordance with ASTM C73 using distilled water as the immersing medium [33]. The relative density was calculated by dividing the Archimedes' density by the estimated theoretical density of ZrC ( $\rho=6.71$

g/cm<sup>3</sup>). The Hf content in the as-fabricated billet was determined by instrumental neutron activation analysis (NAA) performed at the Missouri University of Science and Technology Reactor (MSTR). The details of the NAA experiment will be published in a companion paper. Chemical analyses for carbon, oxygen and nitrogen content were conducted by the direct combustion method using infrared absorption detection. Carbon (CS600; Leco, St. Joseph, MI), oxygen and nitrogen (TC500; Leco, St. Joseph, MI) contents were measured by grinding part of the dense specimen to ~200 mesh. Three measurements were conducted for each element to establish repeatability.

**2.2.2. X-Ray Diffraction.** Phases analysis for the ZrO<sub>2</sub> and ZrC powders was performed using X-ray diffraction (XRD). The patterns were collected on a PANalytical X'Pert3 Powder diffractometer (Malvern Panalytical Inc., Westborough, MA, USA) fitted with Cu K $\alpha$  radiation source ( $\lambda=1.5418\text{\AA}$ ). The powder pattern were acquired at room temperature using a step size of 0.02626° with a counting time of 1 s over the 2 $\theta$  range 5-90°. Diffraction patterns were acquired over the 2 $\theta$  range 25-90°. X-ray tube operation conditions were 45 kV and 40 mA.

XRD analysis was also performed on polished cross section of the hot pressed billet using a PANalytical X'Pert Pro Multipurpose Diffractometer (MPD) fitted with a Cu X-ray tube and an X'Celerator area detector. Diffraction patterns were acquired over the 2 $\theta$  range 5-90° with a step size of 0.03° and 0.5 s of exposure at each step. X-ray tube operation conditions were 40 kV and 40 mA. XRD patterns were analyzed by the Rietveld method (RIQAS, Materials Data, Inc., Livermore, CA, USA).

**2.2.3. Raman Spectroscopy.** Raman measurements were collected using a HORIBA Jobin Yvon LabRAM ARAMIS microRaman spectrometer (Horiba, Edison,

NJ). The specimens were excited by a 632 nm He/Ne laser focused to a 2-3  $\mu\text{m}$  spot using a 50 $\times$  microscope objective lens. Raman spectra were acquired in the backscattering geometry. The laser power was below 2 mW to prevent local heating of the sample. All measurements were conducted at room temperature.

**2.2.4. Electron Microscopy.** Microstructure of the as-fabricated pellet was analyzed on polished cross sections by field emission scanning electron microscopy (FIB-SEM Scios<sup>TM</sup> DualBeam<sup>TM</sup>, FEI, Hillsboro, Oregon). Key microstructural features like content of secondary phases and residual porosity were evaluated from FESEM micrographs acquired using an accelerating voltage of 5 keV. Electron backscattered diffraction (EBSD), coupled with energy dispersive X-ray spectroscopy (EDS), was performed using an Oxford HKL system and energy dispersive spectrometer in the FEI Scios DualBeam scanning electron microscope. EBSD conditions utilized for the analysis were a 20 kV accelerating voltage, 15 mm working distance and a 70° tilt. A 0.15  $\mu\text{m}$  step size was selected for the analysis. The specimen was analyzed using a single scan; with an average area large enough to include more than 50 unique grains and thereby achieve a larger statistical sample for determining grain size and grain boundary character [17].

The specimen for TEM analyses was prepared by the focused ion beam (FIB) lift-out technique. A 15  $\mu\text{m}$  (width)  $\times$  10  $\mu\text{m}$  (depth) rectangular lamella was thinned to electron transparency by the FIB ( $\sim$ 50 nm). The TEM lamella was imaged using a FEI Tecnai TF30-FEG Twin STEM (FEI, Hillsboro, OR, USA) working at 300 kV. Electron energy loss spectroscopy (EELS) was used to characterize the local elemental composition. High resolution transmission electron microscopy (HRTEM) was used to reveal microstructural details of the inclusions.

### 3. RESULTS

From the XRD analysis of the synthesized  $\text{ZrO}_2$  powder (Fig. 1a), peaks for monoclinic phase (JCPDS card 81-1314) and tetragonal phase (JPSD card 50-8019) were identified. The peaks were broad, presumably due to the small crystallite size. Rietveld analysis of the XRD data yielded tetragonal phase fractions of approximately 5 wt%. The crystallite sizes estimated by Rietveld method were  $\sim 30$  nm for both tetragonal and monoclinic  $\text{ZrO}_2$  phases. Fig. 1b shows the XRD pattern for the  $\text{ZrC}_x$  powder synthesized using a starting  $\text{ZrO}_2\text{:C}$  molar ratio of 1:3 and heated to  $1800^\circ\text{C}$ .  $\text{ZrC}_x$ , with  $Fm\bar{3}m$  crystal space group (JCPDF card 35-0784), was the only phase detected.

The as-sintered  $\text{ZrC}_x$  pellet had a relative density of 95%. Gas fusion analysis indicated that the as-fabricated  $\text{ZrC}$  pellet contained 11.53 wt% carbon, 1.01 wt% oxygen and 0.204 wt % nitrogen. The oxygen and nitrogen impurities could come from the starting powder used for carbothermal reduction or introduced during processing of the billet. The hafnium content measured by NAA was about 400 parts per million (wppm). Fig. 1c shows the XRD pattern obtained from the cross sectioned  $\text{ZrC}_x$  pellet. The only phase detected was  $\text{ZrC}_x$  and no extra peaks were apparent. The empirical correlation between lattice parameter and carbon content determined by Jackson and Lee [34] was used to estimate the carbon content from the lattice parameter determined by Rietveld refinement of the XRD pattern. The lattice parameter of the pellet determined by Rietveld refinement was  $4.689064 \text{ \AA}$ , corresponding to a carbon stoichiometry of  $\text{ZrC}_{0.92}$ .

The microstructure of the as-sintered  $\text{ZrC}$  billet is depicted in Fig. 2. Individual equiaxed  $\text{ZrC}$  grains were apparent in the micrograph due to channeling contrast. The

densified microstructure contained discrete porosity and secondary phases. These features were discriminated based on their grey level intensity and morphological variances with respect to each other and the ZrC matrix. The porosity appeared as round black inclusions with charging around the edges. Small pores with diameters  $<1.5\ \mu\text{m}$  were observed at the grain boundaries and entrapped within the ZrC grains. No clustering of pores was observed in the microstructure. The fraction of porosity calculated using computerized image analysis was estimated to be less than 7 vol%; It should be mentioned, however, that charging effects around the pores made accurate estimation of pore diameters difficult. The measured fraction of porosity was in good agreement with the relative densities determined by Archimedes' method. In addition to porosity, traces of a secondary phase were also identified in the as-sintered billet. This phase appeared black in contrast with respect to ZrC grains and without charging, indicating that it is likely to be carbon.

EBSD analysis was also conducted for phase identification and to determine grain size distribution and grain boundary character. An inverse pole figure map from EBSD measurements is shown in Fig. 4a. The collected Kikuchi maps were fit with crystallographic information for ZrC, m-ZrO<sub>2</sub>, t-ZrO<sub>2</sub>, c-ZrO<sub>2</sub>, and C-graphite, which could occur within the composition of interest. The EBSD analysis did not detect any precipitates in the matrix, probably because of the large spot size used during the scan. The white regions in the inverse pole figure map were points where the Kikuchi patterns could not be indexed. They were most probably defects in the surface layer such as residual porosity or precipitates that were extracted during ceramographic preparation. According to the EBSD orientational map, the microstructure of the as-prepared ZrC



pellet was inhomogeneous and exhibited a multimodal grain size distribution (Fig 4b). The average grain diameter was around 4.2  $\mu\text{m}$  and an aspect ratio was 0.5. The microstructure revealed large grains (10  $\mu\text{m}$ ) with porosity that was entrapped within the grains. This is typical for ZrC sintered with no additives, which typically reach only 96–98% of theoretical density due to rapid grain growth prior to complete densification [35],[36].

Pole figure analysis (Fig. 4c) indicated that the microstructure of the as-sintered pellet was not textured, in agreement with the XRD results. Additionally, the grain boundary misorientation histogram (Fig 2d) showed that the pellet contained a large fraction (>90%) of high angle grain boundaries (> 15° misorientation), which is characteristic of polycrystalline materials. Analysis of the misorientation maps of the grain boundaries also showed that the larger grains had relatively few boundaries with low angle misorientation (Fig 5a). This suggested that the absorption of low angles grain boundaries was the predominant mechanism activated during grain growth [37].

To gain further information about the spatial distribution and chemical composition of the secondary phase, backscattered electron images and elemental chemical maps were acquired (Fig. 3). The backscattered electron micrograph (Fig 2a) showed dark inclusions randomly distributed within the lighter contrast ZrC matrix. These dark inclusions appeared approximately uniform in size and shape. SEM/EDS maps (Fig 3b-d) indicated the presence of carbon-enriched and oxygen-enriched precipitates in the ZrC matrix.

Further analysis was done in the TEM to confirm EBSD findings and determine if any additional phases were present in as-sintered pellet that were below the resolution of

the EBSD. An overview of the microstructure in the TEM lift-out is given in Fig. 6a. The High Angle Annular Dark Field (HAADF) image of the specimen showed that local heterogeneities existed at the nanoscale level within the ZrC matrix. Although most of the grains appeared to be uniform in composition, some grains contained a few dark and medium contrast inclusions with sizes ranging between 50 and 300 nm. These inclusions were mainly inside the  $\text{ZrC}_x$  grains, although some of them were also observed along the grain boundaries. EELS point spectra were acquired at the inner and outer regions of one of the inclusions (Fig. 6b, c, and d) to confirm its chemical composition. The results indicated that the inner region was oxygen-rich compared to the outer region. Moreover, detailed analysis of the EELS spectra revealed differences in the carbon K-edge between inner and outer regions of the inclusion. The fine structure of carbon K-edge EELS spectra acquired from the periphery of the inclusion (Figure 6b and c) was identical to literature references for the C K-edge in  $\text{ZrC}_x$  [38]. On the other hand, the carbon K-edge obtained from the core of the inclusion (Fig. 6d) differed significantly from the C fine structure of  $\text{ZrC}_x$ . This suggested that either a partial zirconium oxycarbide phase formed within the core area or, more likely, the core of the inclusion contained a mixture zirconia and amorphous carbon.

To determine the phase of the inclusions, selected area electron diffraction (SAED) analysis was performed. Fig. 7c shows a representative SAED pattern acquired from one of the dark inclusions located inside a  $\text{ZrC}_x$  grain (Fig 7a). Only one set of diffraction spots was observed in the electron diffraction pattern from the area that contained both matrix and inclusion. Indexing of the SAED pattern showed that the spots were consistent with the ZrC phase along the [211] zone axis. This result suggested that

the inclusions had a very similar structure to the ZrC matrix. One possibility is that these inclusions are simply ZrC with a higher dissolved oxygen content that is giving the elemental contrast observed in the HAADF micrograph. Previous studies have indicated that oxygen dissolution affects the lattice parameter of  $\text{ZrC}_x$  [39]. However, the difference in lattice parameter between the matrix and the inclusion might be so small that it cannot be detected by SAED analysis.

The microstructure of the inclusions was also investigated in the HRTEM mode. Fig. 8c shows a HRTEM image of the inclusion indicated in Fig. 8a. The micrograph revealed that the inclusion had a complex core-shell structure. The core of the inclusion contained a mixture of amorphous phase and nanosized crystals ( $<10$  nm) as shown in Fig. 8d. The fast Fourier transformation (FFT) pattern from the nanosized precipitates present at the core of the inclusion was the same as the simulated pattern of tetragonal  $\text{ZrO}_2$  phase in the 111 zone axis (Fig 8e and 8f). Therefore, there is conclusive evidence that the core region of the inclusions contained oxide phase. The amorphous phase was most likely carbon, which was detected by EELS analysis conducted at the core region (Fig 8b). On the other hand, the shell region of the inclusion consisted of a crystalline ZrC phase with a higher dissolved oxygen content than the ZrC matrix.

Raman spectroscopy was used to investigate the structure of the ZrC matrix and the microscopic carbon inclusions that were visible in the fabricated pellet through optical microscopy. The spectra acquired in ZrC grains (Fig 5a) showed Raman bands at approximately 200, 275, 515 and  $600\text{ cm}^{-1}$ . These bands were assigned to defect related modes induced by carbon vacancies in the ideal NaCl crystal structure of ZrC. The spectrum obtained in this work was similar to those previously reported for

substoichiometric  $\text{ZrC}_x$  [40], [41], suggesting that carbon vacancies were present in the as-sintered  $\text{ZrC}$  matrix. On the other hand, the Raman spectra for the carbon inclusions (Fig. 5b) were characterized by two first order prominent peaks: a Raman active  $E_{2g}$  mode line around  $1590\text{ cm}^{-1}$  (known as G band), and the disorder induced peak at  $1333\text{ cm}^{-1}$  (D band). These peaks were due to  $sp^2$  and  $sp^3$  carbon bonding respectively. The presence of both  $sp^3$  and  $sp^2$  hybridization is common for micron sized grains of graphite [42]. According to previous studies [42], [43], the Raman intensity ratio ( $I_D/I_G$ ) is related to the amount of disorder in graphitic carbon. Peak fitting of the Raman spectra for 10 carbon inclusions revealed an average D/G peak intensity ratio of 1.32. This ratio was above the standard value for polycrystalline graphite ( $D/G=0.75$ ) [43], indicating that the carbon inclusions around the  $\text{ZrC}$  grains are disordered graphitic domains. The nature of the carbon inclusions in the as-sintered ceramic differs from the commercial carbon black used for carbothermal reduction. According to Raman analysis, the D/G ratio for carbon black powder was 1.82, suggesting relatively more disordered structure characteristic of carbon allotropes with amorphous structure.

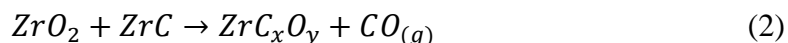
#### 4. DISCUSSION

The multimodal approach used in this work revealed heterogeneities at the micro and nanoscale level in the densified  $\text{ZrC}_x$  specimen. The simplified sketch in Fig. 10 summarizes the most important features and phases formed in the fabricated pellet. Cross-sectional SEM analysis indicated that the specimen contained remnant oxycarbide and carbon inclusions that were randomly distributed within the  $\text{ZrC}_x$  grains

and along the grain boundaries. These secondary phases were not detected by XRD analysis, likely due to being below the detection limit of this method. Some of the residual carbon observed in the densified microstructure could be attributed to the free carbon present in ZrC raw powder. Rejasse *et al.* [14] showed that samples corresponding to the theoretical stoichiometric ZrC composition have some free carbon, regardless of the carbothermal reduction synthesis temperature. According to previous work, the presence of residual free carbon in the starting zirconium oxycarbide powders leads to the appearance of graphitized intergranular inclusion after hot-pressing. Raman analysis of the carbon inclusions supports the hypothesis that partial conversion of amorphous carbon black into crystalline graphite occurred during the hot pressing. The presence of carbon inclusions in the ZrC matrix is detrimental for applications in nuclear systems because they reduce the mechanical performance by favoring microcrack displacements and decrease the swelling resistance under irradiation conditions [7].

Besides carbon, isolated oxygen rich  $\text{ZrC}_x$  inclusions were homogeneously dispersed throughout the specimen as revealed by BSE contrast imaging and TEM analysis. These inclusions were assumed to have originated from surface oxide impurities in the ZrC powders. It is known that native oxide layers usually form on the outside of fine ZrC particles when they are exposed to air. TEM analysis showed that the inclusions had a characteristic core-shell structure. The core region was filled with tetragonal  $\text{ZrO}_2$  nanocrystals embedded within an amorphous phase containing oxygen, carbon, and zirconium. The shell was made of crystalline zirconium carbide with higher oxygen content compared to the matrix. The composite structure of the inclusions suggested that they might be  $\text{ZrO}_2$  contaminants that were being slowly reduced during hot-pressing.

Previous studies have shown that ZrC reacts with ZrO<sub>2</sub> at temperatures above 1600 °C to form oxycarbide solutions [44], [45],[46]. Since the sintering temperature used in the present work was T=2200 °C, it is conceivable that the residual oxygen impurities could dissolve into the lattice during densification. A possible route for the reduction of zirconia inclusions is given by:



As shown in Rxn. (2), the stabilization of ZrC<sub>x</sub>O<sub>y</sub> solutions will lead to evolution of CO and the concomitant creation of porosity around ZrO<sub>2</sub> inclusions [45]. However, the existence of carbon vacancies in ZrC<sub>x</sub>, would reduce the CO yield because oxygen atoms can directly occupy carbon vacancies instead of bonding with carbon atoms to form CO and carbon vacancies [44]. In the present work, the fabricated ZrC matrix was substoichiometric as indicated by Raman and XRD analysis. This could help to explain why no porosity was observed around the oxycarbide inclusions. The addition of ZrO<sub>2</sub> could slightly enhance the densification process. The added ZrO<sub>2</sub> could also accelerate grain boundary migration in ZrC grains.

Both XRD and Raman analysis showed that the ZrC<sub>x</sub> matrix was carbon deficient after hot-pressing, even when enough carbon black was used to produce a fully stoichiometric ZrC. This result was supported by the observation of carbon inclusions as a secondary phase, as observed by microscopic and Raman analysis. The reason for this limited carbon incorporation into the zirconium carbide phase is not obvious from the results of the present study. However, similar lower carbon incorporation has been previously reported in near stoichiometric ZrC<sub>x</sub> (x>0.9) compositions [47]. A possible

explanation for this behavior could be associated to the presence of residual oxygen and nitrogen atoms in the carbide lattice. The incorporation of these impurities during processing and sintering could produce a combination of carbon deficient  $\text{ZrC}_x$  and excess carbon that goes undetected by XRD and other typical characterization methods. Moreover, the substitution of carbon atoms by oxygen and nitrogen in the zirconium carbide lattice could lead to the stabilization of a higher density of carbon vacancies [48]. In this study, chemical analysis of the hot-pressed specimen indicated the presence of residual oxygen and nitrogen. Thus, it is plausible these impurities could have played a role in the stabilization of vacancies in the  $\text{ZrC}$  matrix, which would result in excess carbon in the ceramic. To validate this hypothesis, a more accurate chemical analysis will be needed to discriminate the occupancy in the carbon sublattice in  $\text{ZrC}_x$ .

Although the processing and sintering conditions used in this work resulted in  $\text{ZrC}$  specimens with potentially undesirable microstructural characteristics for nuclear applications, the results presented here are still important because they provide insights into what needs to be done to manufacture suitable  $\text{ZrC}_x$  fuel matrices. For example, refinement of the processing parameters is required to synthesize and hot-pressed  $\text{ZrC}$  under conditions that prevent the solution of nitrogen and oxygen impurities, and the precipitation of carbon. Additionally, it is recommended to implement a multimodal methodology to evaluate the compositional homogeneity of monolithic  $\text{ZrC}_x$ , since residual amounts of secondary phases cannot be detected by XRD and other typical characterization methods.

## 5. CONCLUSIONS

ZrC<sub>x</sub> powder with low Hf content was successfully synthesized by carbothermal reduction of ZrO<sub>2</sub> and carbon black powders at 1800 °C. The synthesized ZrC<sub>x</sub> powder was hot-pressed without any sintering additives at 2200 °C and 32 MPa for 90 min. The sintering conditions resulted in the formation of a pellet with a relative density of 95%, providing enough porosity to accommodate fuel burnup. Besides ZrC<sub>x</sub>, no other phases were identified by XRD analysis of the as-sintered specimen. EBSD revealed that average grain sizes ranged from 2 to 10 μm. SEM/EDS analysis revealed that the hot-pressed ZrC<sub>x</sub> billet contained detectable amounts of carbon and oxygen-rich secondary phases. The formation of carbon and oxygen-rich inclusions was attributed to the presence of residual free carbon and oxide contaminants in the starting ZrC<sub>x</sub> powder. Raman examination of the carbon inclusions indicated that structural reorganization of free carbon into the disordered graphite domains occurred during the sintering treatment. Additionally, TEM examination of the hot-pressed pellet showed the presence of nanometric core-shell oxycarbide inclusions in the ZrC matrix. Application of EELS and HRTEM analysis indicated that the core regions of the inclusions were filled with tetragonal ZrO<sub>2</sub> nanocrystals embedded within an amorphous phase containing oxygen, carbon, and zirconium; whereas the shell regions were made of crystalline zirconium oxycarbide. The composite structure of the inclusions suggested that they were more likely ZrO<sub>2</sub> impurities that were being slowly reduced during hot-pressing. The study demonstrated the influence that impurities introduced during powder processing have on the densification of ZrC and the resulting microstructure.



## **ACKNOWLEDGEMENTS**

This research was supported by Nuclear Regulatory Commission Faculty Development Grant NRC-HQ-84-15-G-0044 and by the Ceramics program of the U.S. National Science Foundation as part of project DMR 1742086. The microscopy work was conducted at the Electron Microscopy Center (EMC) of the University of Missouri Columbia with partial funding through the EMC Excellence Microscopy Award. Material synthesis and X-ray diffraction measurements were performed using facilities of the Materials Research Center (MRC) located at the Missouri University of Science and Technology. The authors would also like to thank Craig Reisner at the Missouri University of Science and Technology Reactor (MSTR) for his help during neutron activation experiments.

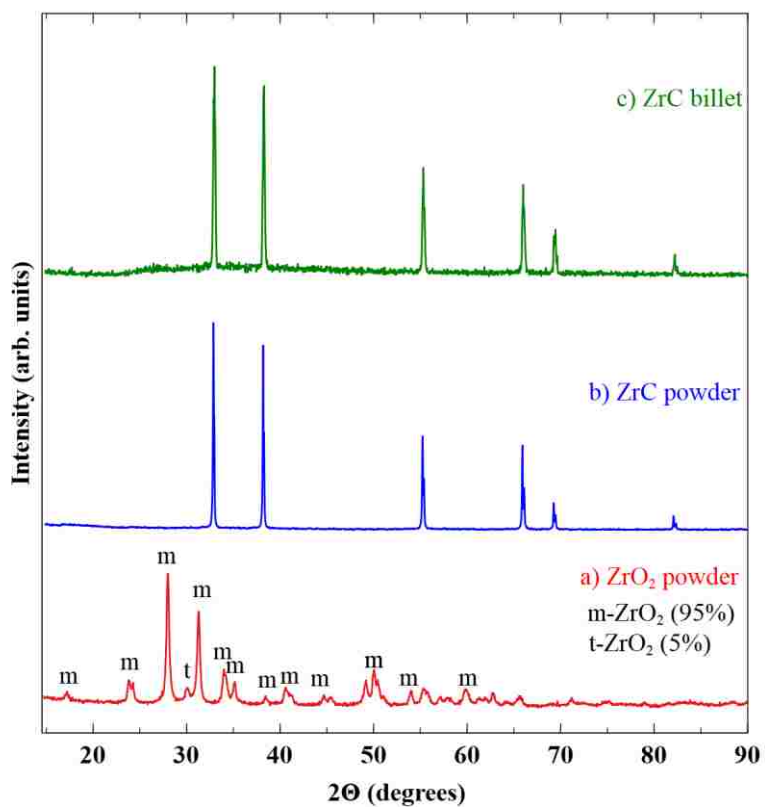


Figure 1. X-ray diffraction patterns of (a) synthesized  $\text{ZrO}_2$  powder, (b)  $\text{ZrC}_x$  powder prepared by carbothermal reduction at 1800 °C, and (c)  $\text{ZrC}_x$  pellet after sintering at 2200 °C.

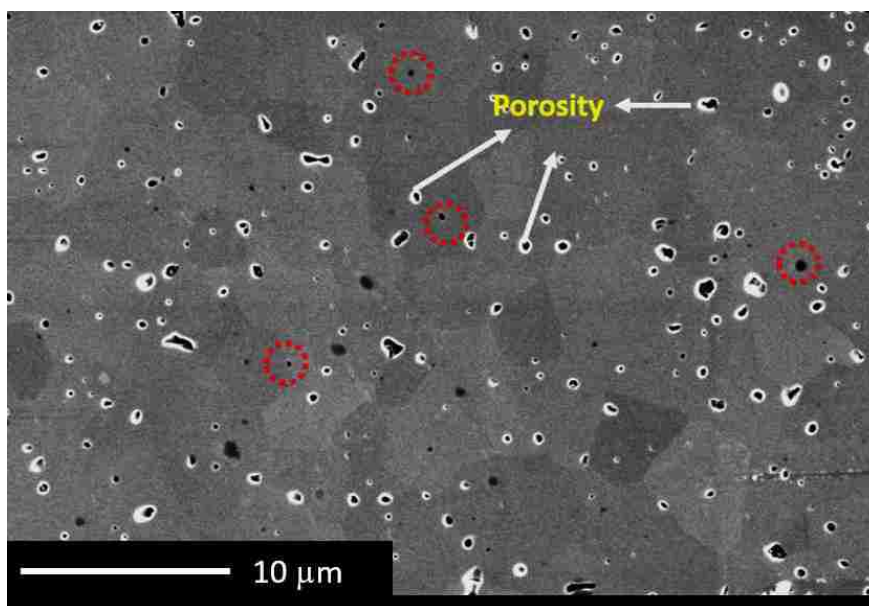


Figure 2. SEM micrograph showing representative microstructure of HP  $\text{ZrC}_x$  pellet.

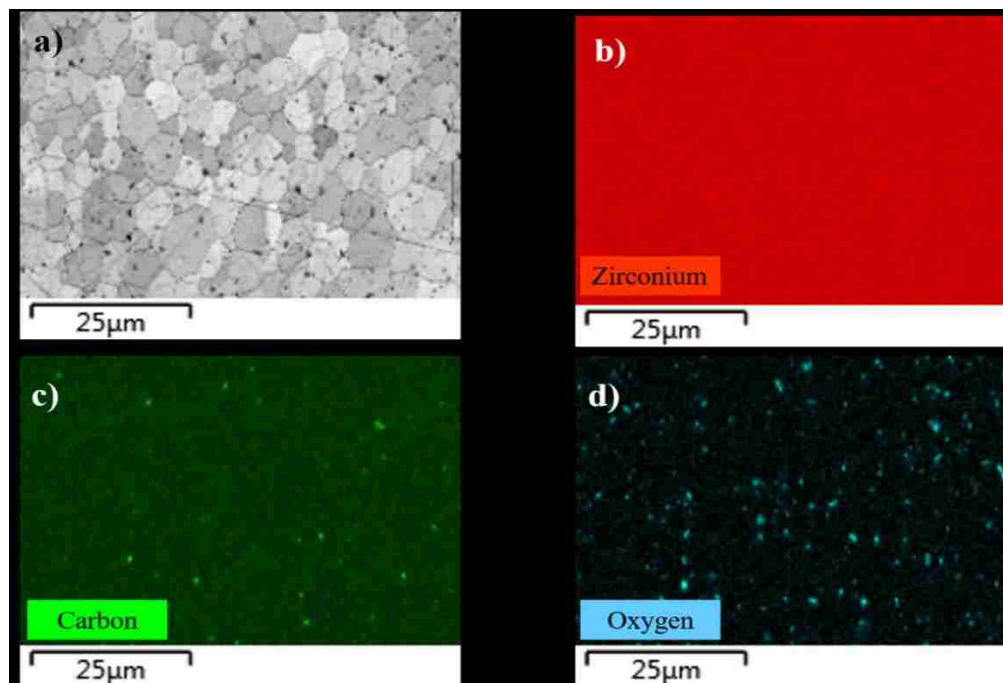


Figure 3. (a) BSE SEM micrograph of HP  $\text{ZrC}_x$  pellet showing inclusions with dark contrast. EDS elemental maps of (b) Zirconium, (c) Carbon, and (d) Oxygen collected to investigate the compositions of the inclusions.

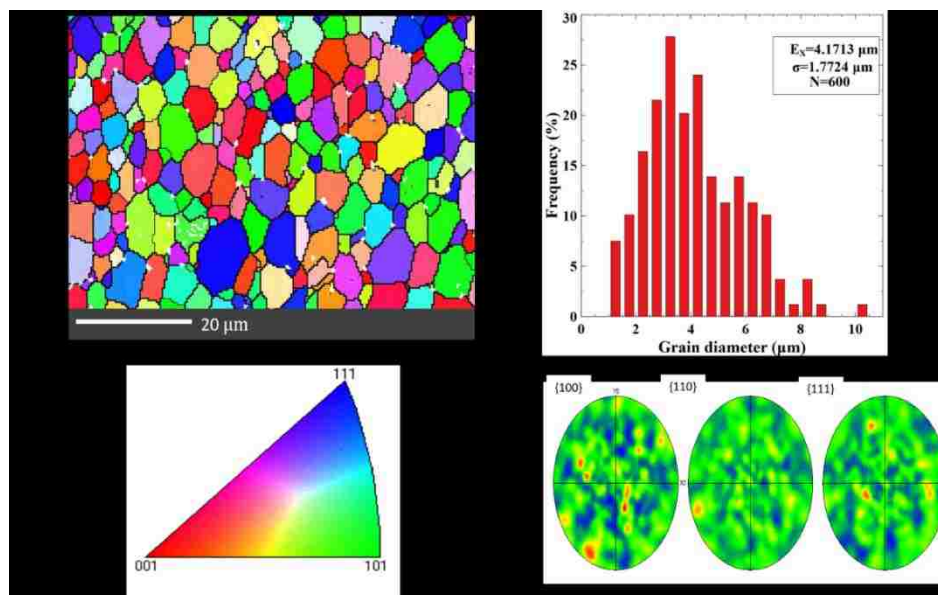


Figure 4. (a) Representative EBSD inverse pole figure map of the HP  $\text{ZrC}_x$  pellet, (b) histogram of grain size distribution, (c) EBSD texture plots. (A color version of this figure can be viewed on the web version of this article).

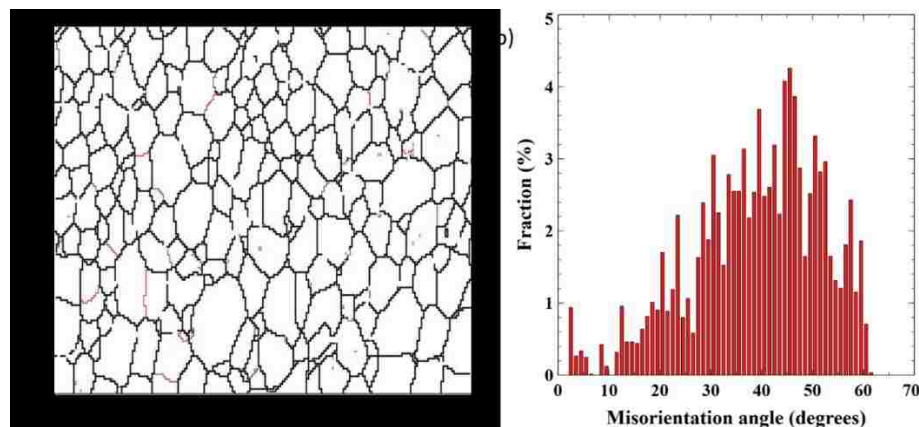


Figure 5. Grain boundary analysis of the HP  $\text{ZrC}_x$  pellet. (a) distribution map of low-angle (red color) and high-angle (black color) grain boundaries. (b) Histogram of the measured misorientation angle distribution for the HP  $\text{ZrC}_x$  pellet. (A color version of this figure can be viewed on the web version of this article).

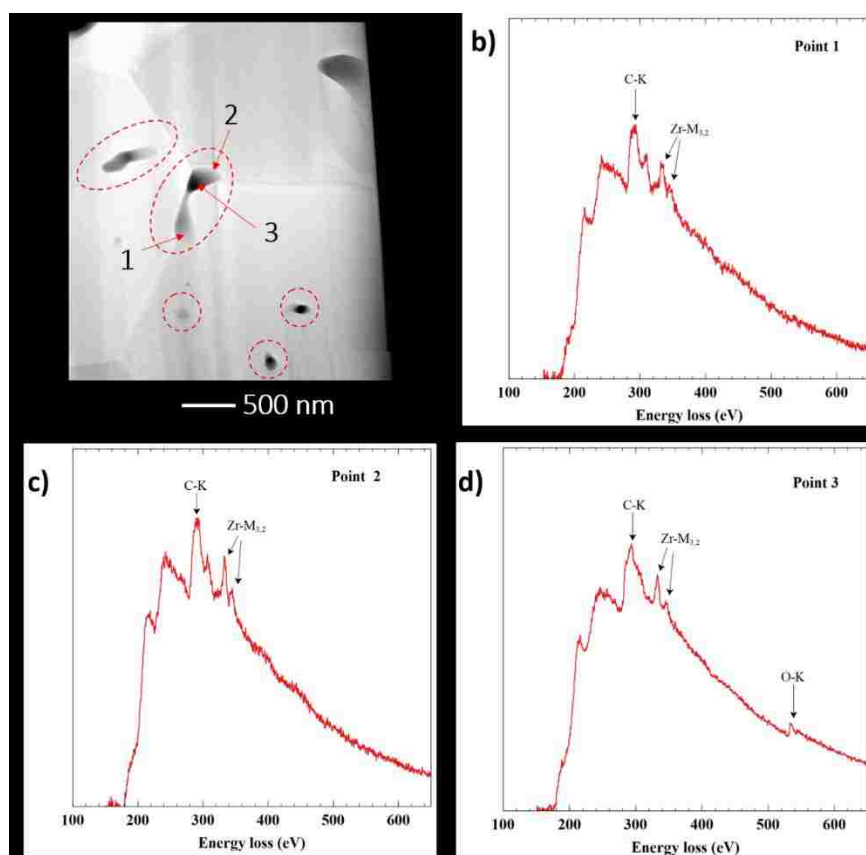


Figure 6. (a) HAADF-STEM micrograph showing the presence of inclusion pockets within grains and along the grain boundaries. Background-subtracted EELS spectrum from (b) point 1, (c) point 2, and (d) point 3 respectively.

Figure 1 consists of six panels (a-f) showing the structure and composition of a ZrC shell and an oxygen-rich core. Panel (a) is a TEM image of a ZrC shell with a red box highlighting a region. Panel (b) is an EELS spectrum of the region in (a) showing peaks for C-K, Zr-M<sub>23</sub>, and O-K. Panel (c) is a HRTEM image of the ZrC shell and oxygen-rich core with a red box highlighting a region. Panel (d) is a HRTEM image of the oxygen-rich core with a red box highlighting a region. Panel (e) is a HRTEM image of the oxygen-rich core with a red box highlighting a region. Panel (f) is a HRTEM image of the oxygen-rich core with a red box highlighting a region.

Figure 8. (a) HAADF-STEM micrograph showing the presence of inclusion pockets within  $\text{ZrC}_x$  grains, (b) Background-subtracted EELS spectrum from red squared inclusion in (a), (c) low magnification HRTEM image of inclusion, (d) HRTEM image from the core region of the inclusion, (e) FFT pattern of the red squared region in the core area of the inclusion, (f) simulated electron diffraction pattern based on the tetragonal structure of  $\text{ZrO}_2$ .

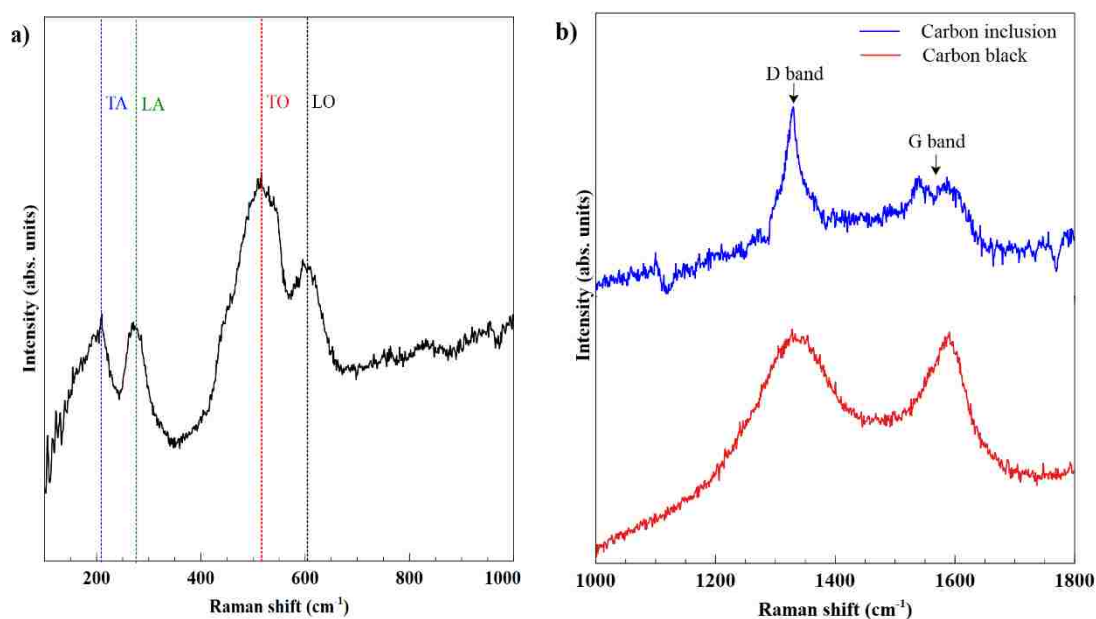


Figure 9. Representative Raman spectra from (a) individual  $\text{ZrC}_x$  grains, (b) carbon inclusions (blue) observed in the hot-pressed  $\text{ZrC}_x$  specimen, and carbon black powder (red) used for carbothermal reduction. ((A color version of this figure can be viewed on the web version of this article).

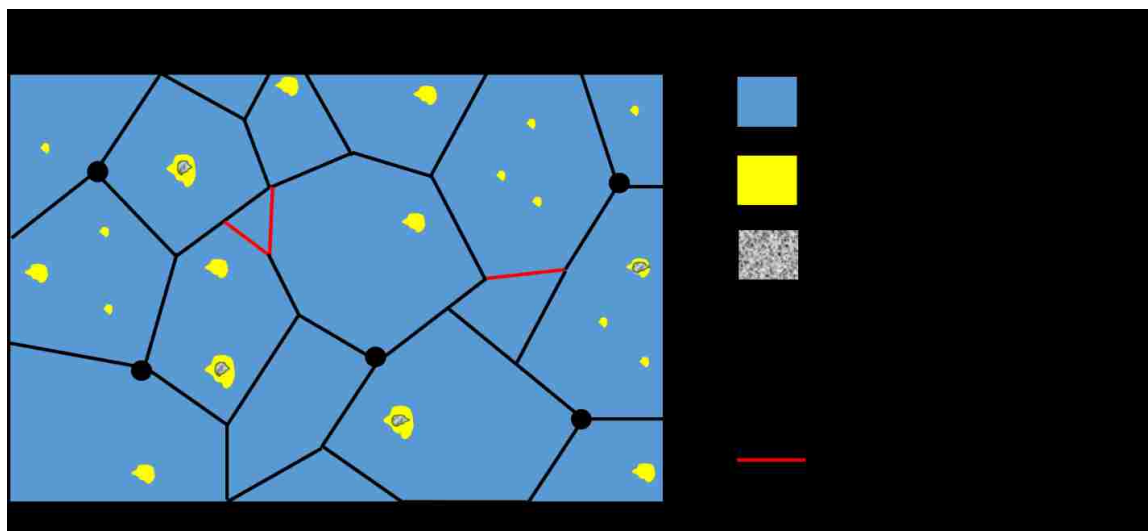


Figure 10. Schematic showing the main microstructural features of the as-sintered  $\text{ZrC}_x$  specimen.

## REFERENCES

- [1] M. Dorneval *et al.*, “Sintering and characterization of ceramics for GFR applications,” in *Proceedings of the American Nuclear Society - International Congress on Advances in Nuclear Power Plants 2005, ICAPP’05*, vol. 4, pp. 2458-2466, 2005.
- [2] M. K. Meyer, R. Fielding, and J. Gan, “Fuel development for gas-cooled fast reactors,” *J. Nucl. Mater.*, vol. 371, no. 1–3, pp. 281–287, 2007.
- [3] R. V. Sara, “The System Zirconium-Carbon,” *J. Am. Ceram. Soc.*, vol. 48, no. 5, pp. 243–247, May 1965.
- [4] H. O. Pierson, “Carbides of Group IV,” in *Handbook of Refractory Carbides and Nitrides*, Elsevier, 1996, pp. 55–80.
- [5] L. N. Grossman, “High-Temperature Thermophysical Properties of Zirconium Carbide,” *J. Am. Ceram. Soc.*, vol. 48, no. 5, pp. 236–242, 1965.
- [6] K. Minato *et al.*, “Fission product release from ZrC-coated fuel particles during postirradiation heating at 1600°C,” *J. Nucl. Mater.*, vol. 224, no. 1, pp. 85-92, 1995.
- [7] Y. Katoh, G. Vasudevamurthy, T. Nozawa, and L. L. Snead, “Properties of zirconium carbide for nuclear fuel applications,” *J. Nucl. Mater.*, vol. 441, no. 1–3, pp. 718–742, 2013.
- [8] J. Gan, Y. Yang, C. Dickson, and T. Allen, “Proton irradiation study of GFR candidate ceramics,” *J. Nucl. Mater.*, vol. 389, no. 2, pp. 317-325, 2009.
- [9] C. J. Ulmer, A. T. Motta, and M. A. Kirk, “In situ ion irradiation of zirconium carbide,” *J. Nucl. Mater.*, vol. 466, pp. 606–614, 2015.
- [10] L. L. Snead, Y. Katoh, and S. Kondo, “Effects of fast neutron irradiation on zirconium carbide,” *J. Nucl. Mater.*, vol. 399, no. 2–3, pp. 200–207, 2010.
- [11] H. J. Ryu, Y. W. Lee, S. Il Cha, and S. H. Hong, “Sintering behaviour and microstructures of carbides and nitrides for the inert matrix fuel by spark plasma sintering,” *J. Nucl. Mater.*, vol. 352, no. 1–3, pp. 341–348, 2006.
- [12] D. Sciti, S. Guicciardi, and M. Nygren, “Spark plasma sintering and mechanical behaviour of ZrC-based composites,” *Scr. Mater.*, vol. 59, no. 6, pp. 638–641, 2008.



- [13] L. Feng, W. G. Fahrenholtz, G. E. Hilmas, J. Watts, and Y. Zhou, "Densification, microstructure, and mechanical properties of ZrC–SiC ceramics," *J. Am. Ceram. Soc.*, vol. 102, no. 10, pp. 5786–5795, 2019.
- [14] C. Nachiappan, L. Rangaraj, C. Divakar, and V. Jayaram, "Synthesis and densification of monolithic zirconium carbide by reactive hot pressing," *J. Am. Ceram. Soc.*, vol. 93, no. 5, pp. 1341–1346, 2010.
- [15] S.-K. Sun, G.-J. Zhang, W.-W. Wu, J.-X. Liu, T. Suzuki, and Y. Sakka, "Reactive spark plasma sintering of ZrC and HfC ceramics with fine microstructures," *Scr. Mater.*, vol. 69, no. 2, pp. 139–142, 2013.
- [16] L. B. Nezhevenko, I. I. Spivak, P. V. Gerasimov, B. D. Gurevich, and V. N. Rystsov, "Sintering of zirconium and niobium carbides with carbon additions," *Sov. Powder Metall. Met. Ceram.*, vol. 19, no. 8, pp. 535–539, 1980.
- [17] R. D. Carnahan, K. R. Janowski, and R. C. Rossi, "Elastic Behavior of Arc-Cast Zirconium Carbide-Graphite Alloys," *J. Am. Ceram. Soc.*, vol. 52, no. 9, pp. 475–477, 1969.
- [18] F. Réjasse, O. Rapaud, G. Trolliard, O. Masson, and A. Maître, "Experimental investigation and thermodynamic evaluation of the C–Zr–O ternary system," *RSC Adv.*, no. 6, pp. 100122–100135, 2016.
- [19] V. M. Baranov, V. I. Knyazev, and O. S. Korostin, "The temperature dependence of the elastic constants of nonstoichiometric zirconium carbides," *Strength Mater.*, vol. 5, no. 9, pp. 1074–1077, 1973.
- [20] B. Wei, C. Lei, W. Yujin, Z. Haibin, P. Shuming, O. Jiahu, W. Dong, and Z. Yu., "Densification, mechanical and thermal properties of ZrC<sub>1-x</sub> ceramics fabricated by two-step reactive hot pressing of ZrC and ZrH<sub>2</sub> powders," *J. Eur. Ceram. Soc.*, vol. 38, no. 2, pp. 411–419, 2018.
- [21] D. L. Kohlstedt, "The temperature dependence of microhardness of the transition-metal carbides," *J. Mater. Sci.*, vol. 8, no. 6, pp. 777–786, 1973.
- [22] B. Maier, Y.-K. Yang, and T. R. Allen, "Silver diffusivity measurement in ZrC with SIMS to study the release behavior of 110mAg for nuclear fuel applications," *J. Nucl. Mater.*, vol. 478, pp. 135–143, 2016.
- [23] K. Minato, T. Ogawa, T. Koya, H. Sekino, and T. Tomita, "Retention of fission product caesium in ZrC-coated fuel particles for high-temperature gas-cooled reactors," *J. Nucl. Mater.*, vol. 279, no. 2-3, pp. 181–188, 2000.
- [24] C. Gasparri, R. J. Chater, D. Horlait, L. Vandeperre, and W. E. Lee, "Zirconium carbide oxidation: Kinetics and oxygen diffusion through the intermediate layer," *J. Am. Ceram. Soc.*, vol. 101, no. 6, pp. 2638–2652, 2018.



- [25] B. Wei, D. Wang, Y. Wang, H. Zhang, S. Peng, C. Xu, G. Song, and Y. Zhou., "Corrosion kinetics and mechanisms of ZrC 1-x ceramics in high temperature water vapor," *RSC Adv.*, vol. 8, no. 32, pp. 18163–18174, 2018.
- [26] D. Gosset, M. Dollé, D. Simeone, G. Baldinozzi, and L. Thomé, "Structural evolution of zirconium carbide under ion irradiation," *J. Nucl. Mater.*, vol. 373, no. 1–3, pp. 123–129, 2008.
- [27] D. Gosset, M. Dollé, D. Simeone, G. Baldinozzi, and L. Thomé, "Structural behaviour of nearly stoichiometric ZrC under ion irradiation," *Nucl. Instruments Methods Phys. Res. Sect. B Beam Interact. with Mater. Atoms*, vol. 266, no. 12–13, pp. 2801–2805, 2008.
- [28] Y. Yang, C. A. Dickerson, H. Swoboda, B. Miller, and T. R. Allen, "Microstructure and mechanical properties of proton irradiated zirconium carbide," *J. Nucl. Mater.*, vol. 378, no. 3, pp. 341–348, 2008.
- [29] D. Simon and B. Taylor, "Overcoming the deleterious effect of hafnium in tungsten–zirconia catalysts: The use of doping and thermal treatments," *J. Catal.*, vol. 262, no. 1, pp. 127–133, 2009.
- [30] R. Krishnan and M. K. Asundi, "Zirconium alloys in nuclear technology," *Proc. Indian Acad. Sci. Sect. C Eng. Sci.*, vol. 4, no. 1, pp. 41–56, 1981.
- [31] J. M. Lonergan, D. L. McClane, W. G. Fahrenholtz, and G. E. Hilmas, "Thermal Properties of Hf-Doped ZrB<sub>2</sub> Ceramics," *J. Am. Ceram. Soc.*, vol. 98, no. 9, pp. 2689–2691, 2015.
- [32] J. M. Lonergan, W. G. Fahrenholtz, and G. E. Hilmas, "Zirconium diboride with high thermal conductivity," *J. Am. Ceram. Soc.*, vol. 97, no. 6, pp. 1689–1691, 2014.
- [33] ASTM, "ASTM C373-14 Standard Test Method for Water Absorption, Bulk Density, Apparent Porosity, and Apparent Specific Gravity of Fired Whiteware Products," *Astm C373-88*, 1999.
- [34] H. F. Jackson and W. E. Lee, "Properties and characteristics of ZrC," R.J.M. Konings (Ed.), *Compr. Nucl. Mater.*, Elsevier, Oxford (2012), pp. 339–372.
- [35] P. Barnier, C. Brodhag, and F. Thevenot, "Hot-pressing kinetics of zirconium carbide," *J. Mater. Sci.*, vol. 21, no. 7, pp. 2547–2552, 1986.
- [36] A. G. Lanin, E. V. Marchev, and S. A. Pritchin, "Non-isothermal sintering parameters and their influence on the structure and properties of zirconium carbide," *Ceram. Int.*, vol. 17, no. 5, pp. 301–307, 1991.

- [37] K. D. Johnson and D. A. Lopes, "Grain growth in uranium nitride prepared by spark plasma sintering," *J. Nucl. Mater.*, vol. 503, pp. 75-80, 2018.
- [38] A. J. Craven and L. A. J. Garvie, "Electron Energy Loss Near Edge Structure (ELNES) on the Carbon K-Edge in Transition Metal Carbides with the Rock Salt Structure," *Microsc. Microanal. Microstruct.*, vol. 6, no. 1, pp. 89-98, 1995.
- [39] F. Réjasse, O. Rapaud, G. Trolliard, O. Masson, and A. Maître, "Experimental investigation and thermodynamic evaluation of the C–O–Zr ternary system," *RSC Adv.*, vol. 100, no. 6, pp. 100122–100135, 2016.
- [40] H. Wipf, M. V. Klein, and W. S. Williams, "Vacancy-Induced and Two-Phonon Raman Scattering in  $\text{ZrC}_x$ ,  $\text{NbC}_x$ ,  $\text{HfC}_x$ , and  $\text{TaC}_x$ ," *Phys. status solidi*, vol. 108, no. 2, pp. 489–500, 1981.
- [41] S. Pellegrino, L. Thomé, A. Debelles, S. Miro, and P. Trocellier, "Radiation effects in carbides: TiC and ZrC versus SiC," *Nucl. Instruments Methods Phys. Res. Sect. B Beam Interact. with Mater. Atoms*, vol. 327, no. 1, pp. 103–107, 2014.
- [42] A. C. Ferrari and J. Robertson, "Interpretation of Raman spectra of disordered and amorphous carbon," *Phys. Rev. B*, vol. 61, no. 20, pp. 14095–14107, 2000.
- [43] E. F. Antunes, A. O. Lobo, E. J. Corat, V. J. Trava-Airoldi, A. A. Martin, and C. Veríssimo, "Comparative study of first- and second-order Raman spectra of MWCNT at visible and infrared laser excitation," *Carbon N. Y.*, vol. 44, no. 11, pp. 2202–2211, 2006.
- [44] H.-L. Liu, Z.-Y. Man, J.-X. Liu, X.-G. Wang, and G.-J. Zhang, "Solid solution and densification behavior of zirconium oxycarbide ( $\text{ZrC}_x\text{O}_y$ ) ceramics via doping  $\text{ZrO}_2$  and Zr in ZrC," *J. Alloys Compd.*, vol. 729, pp. 492–497, 2017.
- [45] E. Min-Haga and W. D. Scott, "Sintering and mechanical properties of  $\text{ZrC-ZrO}_2$  composites," *J. Mater. Sci.*, vol. 23, no. 8, pp. 2865–2870, 1988.
- [46] Y. Pipon, N. Toulhoat, N. Moncoffre, G. Gutierrez, A. Maître, and M. Gendre, "Influence of the Oxygen content on the thermal migration of Xenon in  $\text{ZrC}_x\text{O}_{1-x}$ ," *J. Nucl. Mater.*, vol. 440, no. 1–3, pp. 546–552, 2013.
- [47] G. W. Chinthaka Silva, A. A. Kercher, J. D. Hunn, R. C. Martin, G. E. Jellison, and H. M. Meyer, "Characterization of zirconium carbides using electron microscopy, optical anisotropy, Auger depth profiles, X-ray diffraction, and electron density calculated by charge flipping method," *J. Solid State Chem.*, vol. 194, pp. 91-99, 2012.

- [48] M. Gendre, A. Maître, and G. Trolliard, "Synthesis of zirconium oxycarbide ( $\text{ZrC}_x\text{O}_y$ ) powders: Influence of stoichiometry on densification kinetics during spark plasma sintering and on mechanical properties," *J. Eur. Ceram. Soc.*, vol. 31, no. 13, pp. 2377–2385, 2011.

## REFERENCES

- [1] U.S. EIA, “Annual Energy Outlook 2019 with projections to 2050,” *Annu. Energy Outlook 2019 with Proj. to 2050*, 2019.
- [2] T. R. Allen *et al.*, “Materials challenges for generation IV nuclear energy systems,” *Nucl. Technol.*, 2008.
- [3] D. Buckthorpe, “Introduction to Generation IV nuclear reactors,” in *Structural Materials for Generation IV Nuclear Reactors*, 2016.
- [4] S. J. Zinkle and G. S. Was, “Materials challenges in nuclear energy,” *Acta Mater.*, 2013.
- [5] T. K. Kim *et al.*, “Current Status and Future Prospective of Advanced Radiation Resistant Oxide Dispersion Strengthened Steel (ARROS) Development for Nuclear Reactor System Applications,” *Nuclear Engineering and Technology*. 2016.
- [6] N. Oono, S. Ukai, S. Kondo, O. Hashitomi, and A. Kimura, “Irradiation effects in oxide dispersion strengthened (ODS) Ni-base alloys for Gen. IV nuclear reactors,” *J. Nucl. Mater.*, 2015.
- [7] R. L. Klueh, “Elevated temperature ferritic and martensitic steels and their application to future nuclear reactors,” *International Materials Reviews*. 2005.
- [8] C. Sun *et al.*, “Microstructure, chemistry and mechanical properties of Ni-based superalloy Rene N4 under irradiation at room temperature,” *Acta Mater.*, 2015.
- [9] T. Yano and B. Matović, “Advanced Ceramics for Nuclear Applications,” in *Handbook of Advanced Ceramics: Materials, Applications, Processing, and Properties: Second Edition*, 2013.
- [10] *Materials Science of Carbides, Nitrides and Borides*. 1999.
- [11] G. Vasudevamurthy, T. W. Knight, E. Roberts, and T. M. Adams, “Laboratory production of zirconium carbide compacts for use in inert matrix fuels,” *J. Nucl. Mater.*, 2008.
- [12] D. Wongsawaeng, “Performance modeling of Deep Burn TRISO fuel using ZrC as a load-bearing layer and an oxygen getter,” *J. Nucl. Mater.*, 2010.
- [13] K. A. Terrani, “Accident tolerant fuel cladding development: Promise, status, and challenges,” *Journal of Nuclear Materials*. 2018.

- [14] I. E. Porter, T. W. Knight, M. C. Dulude, E. Roberts, and J. Hobbs, "Design and fabrication of an advanced TRISO fuel with ZrC coating," *Nucl. Eng. Des.*, vol. 259, pp. 180–186, 2013.
- [15] R. V. SARA, "The System Zirconium—Carbon," *J. Am. Ceram. Soc.*, 1965.
- [16] W. G. Fahrenholtz, E. J. Wuchina, W. E. Lee, and Y. Zhou, *Ultra-High Temperature Ceramics: Materials for Extreme Environment Applications*. 2014.
- [17] H. F. Jackson and W. E. Lee, "Properties and characteristics of zrc," in *Comprehensive Nuclear Materials*, 2012.
- [18] M. M. Opeka, I. G. Talmy, E. J. Wuchina, J. A. Zaykoski, and S. J. Causey, "Mechanical, Thermal, and Oxidation Properties of Refractory Hafnium and zirconium Compounds," *J. Eur. Ceram. Soc.*, 2002.
- [19] K. Minato *et al.*, "Fission product release from ZrC-coated fuel particles during postirradiation heating at 1600°C," *J. Nucl. Mater.*, 1995.
- [20] Y. Katoh, G. Vasudevamurthy, T. Nozawa, and L. L. Snead, "Properties of zirconium carbide for nuclear fuel applications," *J. Nucl. Mater.*, 2013.
- [21] R. W. Harrison and W. E. Lee, "Processing and properties of ZrC, ZrN and ZrCN ceramics: a review," *Advances in Applied Ceramics*. 2016.
- [22] "Zirconium Carbide Crystal Structure." [Online]. Available: [https://en.wikipedia.org/wiki/Zirconium\\_carbide](https://en.wikipedia.org/wiki/Zirconium_carbide). [Accessed: 10-Jun-2109].
- [23] Y. Zhang, B. Liu, and J. Wang, "Self-assembly of Carbon Vacancies in Substoichiometric ZrC<sub>1-x</sub>," *Sci. Rep.*, 2015.
- [24] C. H. De Novion and V. Maurice, "ORDER AND DISORDER IN CARBIDES AND NITRIDES.," *J Phys Colloq*, 1977.
- [25] I. Karimov *et al.*, "NEUTRON DIFFRACTION INVESTIGATION OF ZIRCONIUM CARBIDES.," *Phys. Met. Metallogr.*, 1976.
- [26] W. Hu *et al.*, "Superstructural nanodomains of ordered carbon vacancies in nonstoichiometric ZrC<sub>0.61</sub>," *J. Mater. Res.*, 2012.
- [27] Y. Zhang, B. Liu, J. Wang, and J. Wang, "Theoretical investigations of the effects of ordered carbon vacancies in ZrC<sub>1-x</sub> on phase stability and thermo-mechanical properties," *Acta Mater.*, 2016.
- [28] A. Maitre and P. Lefort, "Solid state reaction of zirconia with carbon," *Solid State Ionics*, 1997.

- [29] A. D. Mazzoni and M. S. Conconi, "Synthesis of Group IVB Metals Oxycarbides by Carboreduction Reactions," *Mater. Res.*, 2002.
- [30] M. Dollé, D. Gosset, C. Bogicevic, F. Karolak, D. Simeone, and G. Baldinozzi, "Synthesis of nanosized zirconium carbide by a sol-gel route," *J. Eur. Ceram. Soc.*, 2007.
- [31] Y. Wang, Q. Liu, J. Liu, L. Zhang, and L. Cheng, "Deposition mechanism for chemical vapor deposition of zirconium carbide coatings," *J. Am. Ceram. Soc.*, 2008.
- [32] J. Aihara *et al.*, "TEM/STEM observation of ZrC-coating layer for advanced high-temperature gas-cooled reactor fuel," *J. Am. Ceram. Soc.*, 2007.
- [33] J. David, G. Trolliard, M. Gendre, and A. Maître, "TEM study of the reaction mechanisms involved in the carbothermal reduction of zirconia," *J. Eur. Ceram. Soc.*, 2013.
- [34] S. Cetinkaya, "Synthesis of fine zirconium carbide powder by carbothermal reaction of carbon-coated zirconia particles," *J. Am. Ceram. Soc.*, 2017.
- [35] M. Gendre, A. Maître, and G. Trolliard, "Synthesis of zirconium oxycarbide ( $\text{ZrC}_x\text{O}_y$ ) powders: Influence of stoichiometry on densification kinetics during spark plasma sintering and on mechanical properties," *J. Eur. Ceram. Soc.*, 2011.
- [36] P. Matteazzi and G. Le Caër, "Room-Temperature Mechanosynthesis of Carbides by Grinding of Elemental Powders," *J. Am. Ceram. Soc.*, 1991.
- [37] Y. Zhou, T. W. Heitmann, W. G. Fahrenholtz, and G. E. Hilmas, "Synthesis of  $\text{ZrC}_x$  with controlled carbon stoichiometry by low temperature solid state reaction," *J. Eur. Ceram. Soc.*, 2019.
- [38] J. B. Holt and S. D. Dunmead, "Self-heating synthesis of materials," *Annu. Rev. Mater. Sci.*, 1991.
- [39] J. Xie, Z. Fu, Y. Wang, S. W. Lee, and K. Niihara, "Synthesis of nanosized zirconium carbide powders by a combinational method of sol-gel and pulse current heating," *J. Eur. Ceram. Soc.*, 2014.
- [40] C. Ang, T. Williams, A. Seeber, H. Wang, and Y. B. Cheng, "Synthesis and evolution of zirconium carbide via Sol-Gel route: Features of nanoparticle oxide-carbon reactions," *J. Am. Ceram. Soc.*, 2013.
- [41] T. KURAUCHI and K. INAGAWA, "Preparation of ZrC Film by Activated Reactive Evaporation," *J. Surf. Finish. Soc. Japan*, 1993.

- [42] A. Gilewicz *et al.*, “Structural, mechanical and tribological properties of ZrC thin films deposited by magnetron sputtering,” *Vacuum*, 2019.
- [43] A. G. Turchanin and V. V. Fesenko, “Thermodynamic characteristics of refractory carbides in their homogeneity regions,” *Sov. Powder Metall. Met. Ceram.*, 1969.
- [44] MORRISON BH and STURGESS LL, “Thermal diffusivity and conductivity of zirconium carbide and niobium carbide from 100 to 2,500 K,” *Res Int Hautes Temp Refract*, 1970.
- [45] H. F. Jackson and W. E. Lee, *Properties and Characteristics of ZrC*, book section 2.13. 2012.
- [46] L. L. Snead, Y. Katoh, and S. Kondo, “Effects of fast neutron irradiation on zirconium carbide,” *J. Nucl. Mater.*, vol. 399, no. 2–3, pp. 200–207, 2010.
- [47] G. W. Keilholtz, R. E. Moore, and M. F. Osborne, “Fast-Neutron Effects on the Carbides of Titanium, Zirconium, Tantalum, Niobium, and Tungsten,” *Nucl. Appl.*, 1968.
- [48] G. H. Reynolds, J. C. Janvier, J. L. Kaae, and J. P. Morlevat, “Irradiation behavior of experimental fuel particles containing chemically vapor deposited zirconium carbide coatings,” *J. Nucl. Mater.*, 1976.
- [49] Y. Yang, C. A. Dickerson, H. Swoboda, B. Miller, and T. R. Allen, “Microstructure and mechanical properties of proton irradiated zirconium carbide,” *J. Nucl. Mater.*, vol. 378, no. 3, pp. 341–348, 2008.
- [50] J. Gan, Y. Yang, C. Dickson, and T. Allen, “Proton irradiation study of GFR candidate ceramics,” *J. Nucl. Mater.*, 2009.
- [51] Y. Huang, B. R. Maier, and T. R. Allen, “Irradiation-induced effects of proton irradiation on zirconium carbides with different stoichiometries,” *Nucl. Eng. Des.*, vol. 277, pp. 55–63, 2014.
- [52] J. Gan, M. K. Meyer, R. C. Birtcher, and T. R. Allen, “Microstructure evolution in ZrC irradiated with Kr ions,” *J. ASTM Int.*, 2006.
- [53] C. J. Ulmer, A. T. Motta, and M. A. Kirk, “In situ ion irradiation of zirconium carbide,” *J. Nucl. Mater.*, vol. 466, pp. 606–614, 2015.
- [54] S. Pellegrino, L. Thomé, A. Debelle, S. Miro, and P. Trocellier, “Damage production in carbide single crystals irradiated with MeV heavy ions,” *Nucl. Instruments Methods Phys. Res. Sect. B Beam Interact. with Mater. Atoms*, 2013.

- [55] S. Pellegrino, L. Thom  , A. Debel  , S. Miro, and P. Trocellier, "Radiation effects in carbides: TiC and ZrC versus SiC," *Nucl. Instruments Methods Phys. Res. Sect. B Beam Interact. with Mater. Atoms*, vol. 327, no. 1, pp. 103–107, 2014.
- [56] M. J. Zheng, I. Szlufarska, and D. Morgan, "Ab initio prediction of threshold displacement energies in ZrC," *J. Nucl. Mater.*, vol. 471, pp. 214–219, 2016.
- [57] M. Jiang *et al.*, "A comparative study of low energy radiation responses of SiC, TiC and ZrC," *Acta Mater.*, 2016.
- [58] M. J. Zheng, I. Szlufarska, and D. Morgan, "Defect kinetics and resistance to amorphization in zirconium carbide," *J. Nucl. Mater.*, 2015.
- [59] C. Jiang, M. J. Zheng, D. Morgan, and I. Szlufarska, "Amorphization driven by defect-induced mechanical instability," *Phys. Rev. Lett.*, 2013.
- [60] H. Haque, "Consequences of delayed air ingress following a depressurization accident in a high temperature reactor," *Nucl. Eng. Des.*, 2008.
- [61] J. J. Lee, T. K. Ghosh, and S. K. Loyalka, "Oxidation rate of nuclear-grade graphite IG-110 in the kinetic regime for VHTR air ingress accident scenarios," *J. Nucl. Mater.*, 2014.
- [62] R. E. Bullock and J. L. Kaae, "Performance of coated UO<sub>2</sub> particles gettered with ZrC," *J. Nucl. Mater.*, 1983.
- [63] J. B. Quinn and I. K. Lloyd, "Comparison of methods to determine the fracture toughness of three glass-ceramics at elevated temperatures," *J. Am. Ceram. Soc.*, 2000.
- [64] T. Ogawa and K. Ikawa, "Crushing strengths of SiC-Triso and ZrC-Triso coated fuel particles," *J. Nucl. Mater.*, 1981.
- [65] G. A. Rama Rao and V. Venugopal, "Kinetics and mechanism of the oxidation of ZrC," *J. Alloys Compd.*, 1994.
- [66] S. Shimada, M. Nishisako, M. Inagaki, and K. Yamamoto, "Formation and Microstructure of Carbon-Containing Oxide Scales by Oxidation of Single Crystals of Zirconium Carbide," *J. Am. Ceram. Soc.*, 1995.
- [67] J. B. Berkowitz-Mattuck, "High-Temperature Oxidation: IV. Zirconium and Hafnium Carbides," *J. Electrochem. Soc.*, 1967.
- [68] C. Gasparri  , R. J. Chater, D. Horlait, L. Vandeperre, and W. E. Lee, "Zirconium carbide oxidation: Kinetics and oxygen diffusion through the intermediate layer," *J. Am. Ceram. Soc.*, 2018.



- [69] R. F. Voitovich and E. A. Pugach, "High-temperature oxidation characteristics of the carbides of the Group VI transition metals," *Sov. Powder Metall. Met. Ceram.*, 1973.
- [70] S. Shimada and T. Ishil, "Oxidation Kinetics of Zirconium Carbide at Relatively Low Temperatures," *J. Am. Ceram. Soc.*, 1990.
- [71] A. S. Shevchenko, R. A. Lyutikov, R. A. Andrievskii, and V. A. Terekhova, "Oxidation of zirconium and niobium carbides," *Sov. Powder Metall. Met. Ceram.*, 1980.
- [72] P. BARNIER and F. THEVENOT, "ChemInform Abstract: A Comparative Study of the Oxidation Resistance of Zirconium Carbide and Zirconium Oxide Carbide.," *ChemInform*, 1989.
- [73] X. M. Hou and K. C. Chou, "Investigation of the effects of temperature and oxygen partial pressure on oxidation of zirconium carbide using different kinetics models," *J. Alloys Compd.*, 2011.

## VITA

Raul F. Florez Meza was born in Sincelejo, Colombia in 1989. He studied at Universidad Nacional de Colombia (UNAL) in Medellin from January 2006 until July 2011 and he graduated with honors with a Bachelor of Science in Chemical Engineering. Later in the same year, he was awarded the Youth Research Fellowship Grant by the Colombian research agency COLCIENCIAS. In 2012, Raul joined the Electrochemical Engineering research group “GRIEQUI” at UNAL, where he conducted fundamental research on solid oxide fuel cells. Raul enrolled as a graduate student at Missouri University of Science and Technology with the Nuclear Engineering program in 2014. He received his master’s degree in Nuclear Engineering in July 2016. Raul published two scientific papers from his master’s work on new cementitious materials for gamma and neutron shielding in dry cask applications. After completing his master, Raul continued with his doctoral studies in Nuclear Engineering. His Ph.D. research focused on investigating the microstructural evolution of  $ZrC_x$  ceramics under irradiation conditions. During his Ph.D. studies, Raul delivered several oral presentations at major national materials science conferences and collaborated with respected researchers at other major institutions in the United States. He was also awarded fellowships and participated in summer schools both in the United States and Europe. Raul successfully defended his doctoral dissertation in October 2019 and received his Ph.D. in Nuclear Engineering in December 2019 from Missouri University of Science and Technology.